Design of a computer controlled magnetic steering system for biomicrorobots

Master Thesis

Author(s):
Exner, Philipp

Publication date:
2005

Permanent link:
https://doi.org/10.3929/ethz-a-005127188

Diploma Thesis

Design of a Computer Controlled Magnetic Steering System for Biomicrorobots

Philipp Exner

Berk Yesin
Adviser

Prof. Dr. Bradley J. Nelson
Institute of Robotics and Intelligent Systems
Swiss Federal Institute of Technology Zurich (ETH)

WS 2004/05

IRIS
Institute of Robotics and Intelligent Systems

ETH
Eidgenössische Technische Hochschule Zürich
Swiss Federal Institute of Technology Zurich

Preface

My diploma project has been a good experience I would not have missed. It is a good example, how interests from different fields of science are building together a forward looking system. At the beginning of the project, there was a basic idea, how a computer controlled microrobot steering system based on magnetic fields could be built. After going into detail, problems from different fields of science came up and showed the complexity of the hole project. Therefore, instead of just starting to design a steering system without detailed knowledge about the forces and behavior of microrobots in application environments like the human eye, time has been invested to find out more about these specific requirements. The insight gained by different experiments allowed to start the goal-oriented research for appropriate magnetic steering principles. During the progress of the project, a lot of problems and questions came up, that asked for new solution approaches, which made the project an interesting challenge.

Working on a future oriented project was a great opportunity for me and I would like to take the chance to thank people who made this project possible and assisted in it:

Berk Yesin, Adviser

Prof. Dr. Bradley J. Nelson, Head of the Institute

Prof. Friedrich Heller, Institute of Geophysics

Philipp Erni, Institute of Food Science and Nutrition

Contents

List of Tables

List of Figures

Abstract

The field of "BioMicroRobotics" is a topical field of research at the IRIS[1] at ETH[2] Zurich. The main research subjects are the understanding of the predominate physical forces that govern part interactions at microscale. Another challenge is to build appropriate sensing and actuation systems. One research project at the IRIS is the development of microrobotic machines that can explore the interior of organisms without being physically connected to the outside world. Recent work in this area showed the feasibility of guiding microrobotic machines by external magnetic fields.

The first task of this project was the analysis of the main forces acting on a microrobot working in different environments. Furthermore, concepts for a 3D[3] field generation device have been developed and partially simulated. By the evaluation of different possibilities to generate magnetic fields to propel microrobots, a system should be developed that allows to propel and steer a microrobot in a pig eye.

[1]Institute of Robotics and Intelligent Systems
[2]Federal Institute of Technology
[3]3 Dimensional

Zusammenfassung

"BioMicroRobotics" ist ein aktuelles Forschungsgebiet am Institut für Robotik und intelligente Systeme (IRIS) an der ETH Zürich. Das Hauptziel der Forschung in diesem Gebiet besteht in der Analyse und dem Verständnis der bei der Interaktion von Mikroteilen auftretenden physikalischen Kräfte. Dabei ist eine der Herausforderungen die Konzeption und Entwicklung von geeigneten Mikrosensoren und -aktoren. In diesen Bereich gehört auch die Entwicklung von Mikrorobotern, die in Zukunft das Innere des menschlichen Körpers ohne eine Verbindung nach aussen erkunden und darin auch einfachere Operationen ausführen können. Die laufende Forschung in diesem Gebiet am IRIS hat gezeigt, dass es grundsätzlich möglich ist, Mikroroboter mit Hilfe von externen magnetischen Feldern in verschiedenen Medien anzutreiben und zu steuern.

In einem ersten Teil der vorliegenden Arbeit wurde eine Analyse der Kräfte, welche auf einen Mikroroboter in verschiedenen Umgebungen einwirken, durchgeführt. Darauf aufbauend wurden verschiedene Konzepte zum Steuern eines Roboters im dreidimensionalen Raum erarbeitet und simuliert. Die Evaluation verschiedener Möglichkeiten zur Erzeugung magnetischer Felder soll schliesslich als Grundlage zur Entwicklung eines System zum Antreiben und Steuern von Mikrorobotern in einem Schweineauge dienen.

Notation

Symbol	Description	Unit
B	Flux Density	T
C_d	Drag Force Coefficient	-
c_p	Specific Heat Capacity	$\frac{J}{kg^\circ K}$
D_N	Drag Number	m
F_d	Drag Force	N
H	Magnetic Field Strength	$\frac{A}{m}$
i	Current Density	$\frac{I}{m^2}$
M	Magnetization	$\frac{A}{m}$
α	Convection Film Coefficient	$\frac{W}{m^{2\circ}K}$
χ	Susceptibility	-
λ	Heat Conduction Capacity	$\frac{W}{m^\circ K}$
μ	Dynamic Viscosity	$Pa\ s$
ν	Kinematic Viscosity	$\frac{m^2}{s}$
ϕ	Flux	Wb
ρ	Density	$\frac{kg}{m^3}$

Constant	Description	Value
g	Newtons Gravitation	$9.81\ \frac{m}{s^2}$
h	Planck's constant	$6.629 \cdot 10^{-34}\ Js$
N_A	Avogadro-Number	$6.022 \cdot 10^{23}\ \frac{1}{mol}$
R	Gas Constant	$8.31\ \frac{J}{mol^\circ K}$
ϵ_0	Influence Constant	$8.85 \cdot 10^{-12}\ \frac{As}{Vm}$
μ_B	Bohr's Magneton	$9.27 \cdot 10^{-24}\ \frac{J}{T}$
μ_0	Permeability of Free Space	$4\pi \cdot 10^{-7}\ \frac{Vs}{Am}$

1 Introduction

To build a steering system for biomicrorobots, requirements and skills from different fields of science must be taken into account. It is an interdisciplinary work between mechanical engineering, physics, electrotechnics, thermodynamics, biology, control systems and informatics. Therefore, it is obvious that combining these fields will lead to conflicts of interests. To find the optimal solution, compromises will be inevitable and must be carefully discussed. Therefore, all factors influencing the system must be thoroughly evaluated. The scope of the presented report is to summarize the most important factors from the different fields of interest and to discuss results from the performed experiments as well as the concepts of different propulsion systems.

In the first part of the report, a short review of the previous work done at the IRIS in the field of steering system developments for microrobot machines is presented. Following the review, the process of designing a steering system is described. Basic requirements and forces acting on microrobots will be considered, followed by an analysis of different field generation devices and a discussion of their possible configurations. Furthermore, the most important points from related topics like coil engineering and tracking will be taken into account and will complete the design process of building an accurate steering system for biomicrorobots.

2 Review of Previous Work

In summer 2004, a first prototype for a biomicrorobot steering system has been developed at IRIS [12]. This system is based on the idea of creating a homogeneous field with a Helmholtz coil pair and a gradient field with a Maxwell coil pair [19]. The Helmholtz coil pair is used to magnetize and align the robot, whereas the Maxwell coil pair is used to propel the robot.
The so called "Gimbal"-system allows to propel and steer microrobots in a small test chamber with dimensions of approximate 1.8 x 1.8 x 1.8 cm.

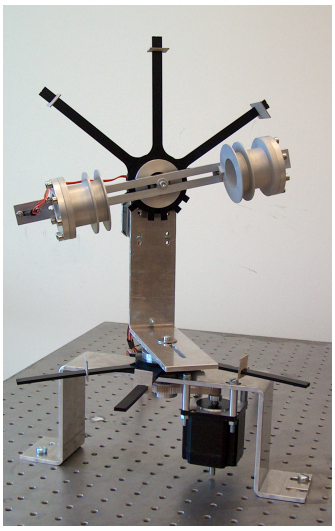

Figure 1: The Gimbal

With this system, some basic experiments have already been performed. It was shown, that the basic idea of propelling microrobots using magnetic fields is feasible. Nevertheless, more detailed experiments must be done before a system for human size scale can be designed and manufactured. Therefore, a new prototype with increased capacity is necessary. Regarding the existing prototype, especially the magnetic field used for propelling the robot is not strong enough for some experiments. Another point that should be improved in the new prototype is the workspace of the system. The dimensions of the usable workspace in the Gimbal system is too small. Especially when additional equipment is needed for the experiments (i.e. when sensors must directly be attached to the test object chamber, the available workspace is not large enough due to the small spacing between the coils).

3 Requirements

The steering system for biomicrorobots has to fulfill different requirements. Most of these requirements are dependending on the application the system is going to be used for.
The long-term objective is to use microrobots in medical applications. One field of application is using the microrobots for assisting health professionals to find defects in the eye and to assist them in eye surgeries. Another application is the investigation of blood vessels. Here, the advantage of using microrobots is the minimal invasive operation property. Operations that until now have been connected with large and time intensive interventions could then be replaced by a new system that reduces the stress for the patient and is less cost intensive. When defining the requirements for a new prototype, the different fields of application must be taken into account.

Robot Movement

To cover a wide range of applications with one system, the system has to allow to propel and to steer the robot in the 3D space. The robot must be able to move in each direction independent of its position. Another requirement is the alignment of the robot. In future, it is planned to use cameras and microactuators on the robot. It has to be assumed, that the workspace of these tools is reduced by the arrangement of the actuators on the robot. Therefore, it is important, that the robot can be aligned in each direction independent of its position.
The velocity of the robot is defined to be at least 0.5 mm/s. When operating in blood vessels, it has to be kept in mind that there is a flow velocity of the blood that can reach up to 0.7 m/s in the arteria.
Another important point of view is the acceleration of the robot along its axis as well as the rotational acceleration. The acceleration of the robot is depending on the force acting on the robot and on the system, excerting the force and torque. I.e. systems including coils are embossed by the inductance of the coils. The so called switching time is mostly limited by the inductance of the coils (Section 11.1). Therefore, a minimum acceleration of the robot is defined.

Geometrical Constraints

As mentioned before, the long-term objective is to use the robot in medical applications for human beings. Therefore, the prototype should already fulfill certain criteria, that become important when scaling the system to human size dimensions.
When operating the system, the patient should - if at all - only be moved at slow speeds. Fast and rotational movements should be avoided because they could lead to sickness of the patient. A lying position of the patient should be preferred so that the system can also be used for injured people, because for them a horizontal position is often the best position. Furthermore, when the system is used for surgeries or investigations in the head area, often a narcosis is necessary and therefore a lying position cannot be avoided.
Due to costs and manufacturing reasons, the dimensions of the prototype should be much smaller than the end product, a human size system. The dimensions should be just large enough, to do conceptual experiments with flowing fluids and with pig eyes.

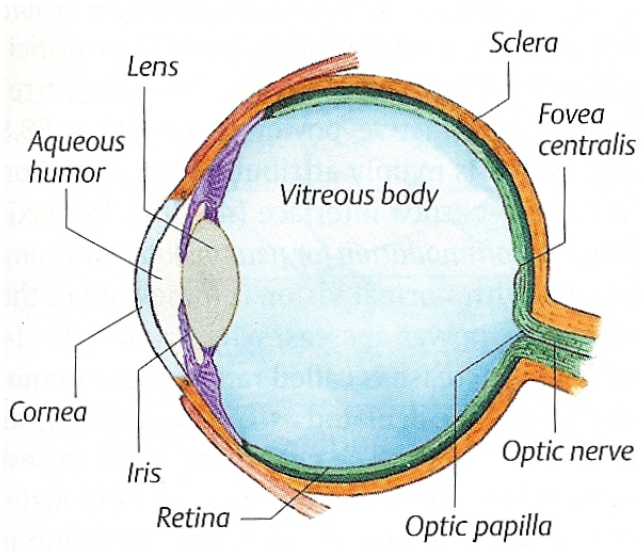

Figure 2: Horizontal plane of the eye [3]

Figure 2 shows the horizontal plane of a human eye. The eye is a slightly asymmetric sphere with an approximate sagittal diameter or length of 25 mm and a transverse diameter of 24 mm. Between the lens and the retina the vitreous cavity is located, which is filled with a gel-like transparent material known as the vitreous body. In this medium the robot should operate.

Concerning the force analysis, the important rheological parameter is the viscosity of the vitreous. The rheology of the eye is a complex field of science and the determination of exact values is quite difficult, especially because there are different viscosities in different regions in the vitreous. There are different viscosities in the anterior, central and posterior vitreous region, that must be taken into account, when calculating forces. It turned out that the maximum viscosity is found in the posterior region. The viscosity of that region is about 4.9 $Pa\ s$ [11].
Because it will not be possible to do experiments with human eyes, the system should be designed in a way that experiments with pig or cow eyes can be done. The maximum viscosity of a cows vitreous body is about 25.5 $Pa\ s$ and therefore much higher than the viscosity of a human or a pigs vitreous body. The viscosity is even so high, that it will not make sense to design a prototype with respect to the viscosity of a cow eye. The system should be designed to use pig eyes that have a viscosity of about 12.2 $Pa\ s$. The dimensions of a pig eye are approximately the same as the dimensions of a human eye. Therefore, the usable space of the prototype should be a cubical chamber with an edge length of at least 3 cm.
The dimensions of the whole system itself are not fixed. Nevertheless, the system should be as small as possible. This aspect is becoming important when the system is scaled up to human size.
Another point of view is the tracking of the microrobot. The geometrical properties of the system must allow the tracking of the microrobot everywhere in the workspace area. Tracking microrobots in human bodies is a field of present research. Ultrasonic or vision tracking systems are only two of many different possibilities. Both of these tracking systems have in common, that they need a line of sight between the receiver/sender and the microrobot that is not covered by any objects that either are not transparent or block the ultrasonic waves. If having rotating parts in the system, it has to be made sure that these rotating

parts do not cover the line of sight of the cameras/ultrasonic devices at any time when the system is in operation. If that cannot be avoided it has to be made sure, that there are other lines of sights that are redundant to the covered views. In that case, more tracking devices than the minimum number are needed.
The requirements for the prototype system are summarized in Table 1

Application	**Scope**	**Description**	**Value**
All	Robots	Robots that can be used in combination with the steering system	All robots mentioned in Appendix A
All	Movement/Alignment	Dimension of robot movement without limitations	All directions in the 3D space
All	Velocity	Minimum reachable velocity in a room fixed coordinate system	0.5 mm/s
All	Linear acceleration	Minimum reachable acceleration along the robots axis	0.5 mm/s^2
All	Rotational acceleration	Minimal reachable rotational acceleration of the robot	0.5 rad/s
All	Test chamber	Minimal dimensions of the test chamber	$3 \times 3 \times 3$ cm
All - visual tracking	Number of line of sights	Number of independent line of sights that are not covered by any part at the same time	2
All - ultrasonic tracking	Number of line of sights	Number of independent line of sights that are not covered by any part at the same time	3
All	Scalability	Possibility to scale the system for human size	possible
All	Motion of object box	If possible the object chamber should stay fixed while the system is in operation	fixed
Eye Operation	Fluid velocity	Velocity of the vitreous fluid	static
Eye Operation	Fluid viscosity	Viscosity of the vitreous of a pigs eye	12.2 $Pa\ s$
Blood vessels	Fluid velocity	Maximum velocity of the blood flow	0.7 m/s
Blood vessels	Fluid viscosity	Viscosity of blood	$4.7 \cdot 10^{-3}$ $Pa\ s$

Table 1: Prototype requirements

4 Forces Acting on the Robot

For paper dimensioning of the steering system, the forces acting on the robot have to be evaluated. To determine the forces acting on the robot, the forces equilibrium is applied on a robot in a flowing fluid. Forces acting on the robot are gravity, buoyancy and drag force.

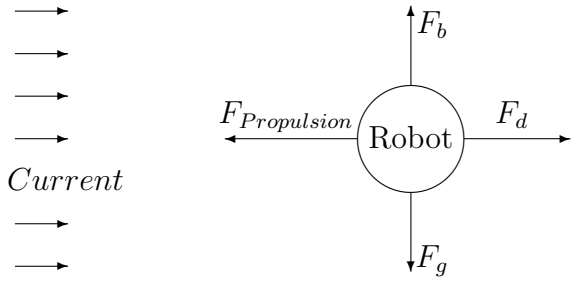

Figure 3: Forces equilibrium

4.1 Gravity Force

The gravity force can be derived from the volume V_m and density ρ_m of the microrobot:

$$F_g = \rho_m V_m g \tag{4.1}$$

4.1.1 Buoyancy Force

The buoyancy force can be calculated by knowing the density of the fluid ρ_f:

$$F_b = V_m \rho_f g \tag{4.2}$$

4.2 Drag Force

The force exerted on a body moving in a fluid depends on the velocity v_f of the body relative to the medium, the density of the fluid ρ_f, the cross section of the body A and the drag force coefficient C_d [10].

$$F_d = \frac{1}{2} C_d \rho_f A v_f^2 \tag{4.3}$$

For a creeping flow around a sphere, the drag force coefficient was determined by Stoke to be

$$C_d = \frac{F}{\frac{\rho}{2} v_f^2 \pi R^2} = \frac{24}{Re} \tag{4.4}$$

where Re is the so called Reynolds Number. Using (4.4) in (4.3) for a sphere with diameter D, the drag force can be determined to be

$$F_d = 3\pi \mu_f D v_f \tag{4.5}$$

Another, solution is the so called Oseen approximation that is an improvement of Stoke's law. Oseens approximation predicts that the drag coefficient is

$$c_D = \frac{24}{Re} \left(1 + \frac{3}{16} Re \right) \tag{4.6}$$

Therefore, the drag force can be written as

$$F_d = \frac{3\pi R^2 v_f (6 R \rho_f v_f + 16 \mu_f)}{8R} \tag{4.7}$$

These theorems describing the drag force are only valid for spheres. Nevertheless, in many publications these assumptions have been used to describe the drag force also for small objects having only approximately the shape of a sphere. This can be a good approximation for rough force estimations. For the IRIS robot that

should be used in combination with the planned steering system, drag numbers have been determined. These robots have more the shape of an ellipsoid than of a sphere (Appendix A).

4.3 IRIS Microrobots Drag Force

As seen in the previous section, the drag force on an specimen in a fluid is dependent on the viscosity of the fluid, the velocity of the fluid around the specimen and the specimens shape. Having a so called "Stokes flow" around the sphere, the drag force can be determined by applying Stokes law (Section 4.2):

$$F_d = 3\pi\mu_f D v_f \tag{4.8}$$

where the geometry factor $3\pi D$ is only valid in the case of a creeping flow around a sphere [10]. By doing experiments, a drag number analogous to the geometry factor for a creeping flow around a sphere can be determined. When this drag number is known for each kind of robot, the drag force for different velocities in fluids with different viscosities can be calculated.
The procedure is to measure the velocity of the robots in fluids of different viscosity and then to apply the forces equilibrium and to calculate the drag force. Doing this experiment in fluids of different viscosity not only allows to determine a drag number but also allows to verify if there is a linear or exponential relation between the drag force and the velocity of the specimen.

4.3.1 Experiment Set-up

The experiment set-up used for the experiments is shown in Figure 4.

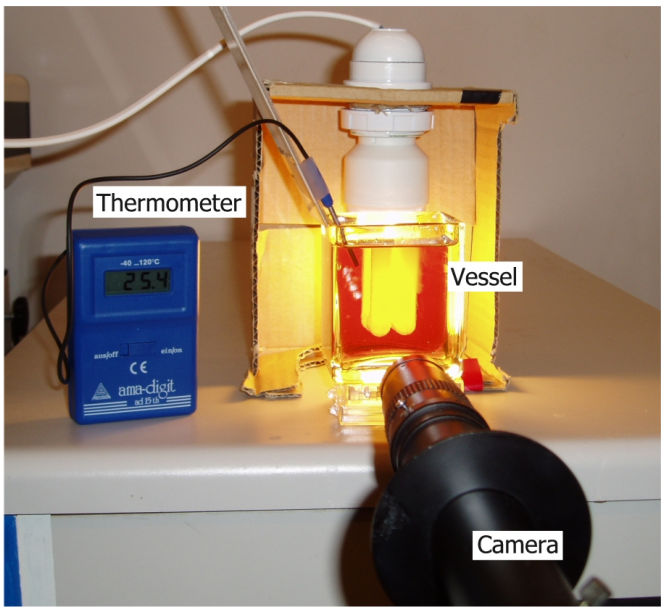

Figure 4: Experiment build-up

The main parts of the experiment set-up are a vessel containing the oil used for the measurement, a camera for tracking the robots position inside the vessel and a thermometer that allows to measure the temperature of the oil.
The measuring procedure is the same for each robot and each oil. The robot is placed into the vessel where the robot then starts to sink due to the gravity force. As soon as the robot reaches the field of view of the camera, the position of the robot is tracked with the camera. Because the robots are quite small, a magnifying ocular is used to improve the precision of the measurements. The time dependent position of the robot that is determined by the camera is written in a data file and is then numerically evaluated.
Figure 5 shows a screenshot of the tracking programs GUI[4] used for the measurements.

[4]Graphical User Interface

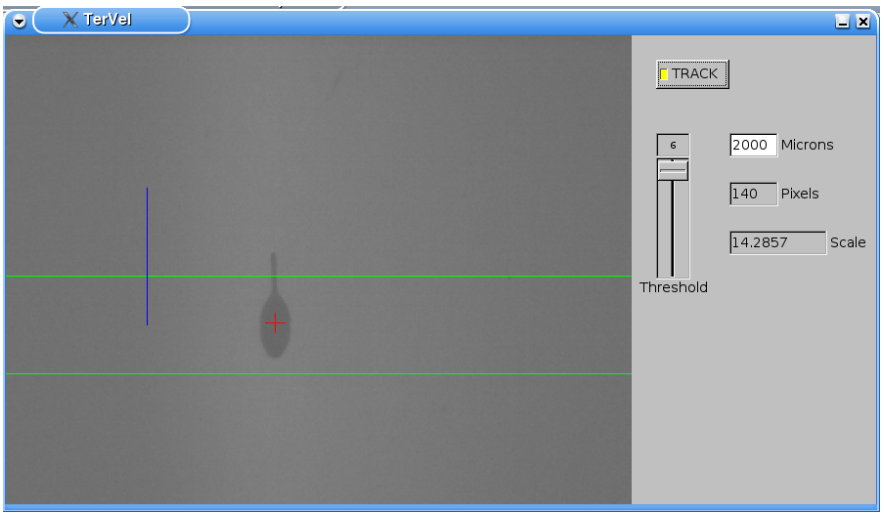

Figure 5: Tracked microrobot

Due to the radiation of the background light, the oil is getting warmer and the viscosity is getting lower. Therefore, for the data evaluation it is important to know the temperature so that the viscosity can be adapted. For that reason, the temperature of the oil is logged after each run of the robot.

4.3.2 Data Evaluation

If the velocity of the microrobot is known, the drag force can be determined by applying the forces equilibrium. This implies, that the measured velocity is constant, or in other words, that the microrobot has already reached its final velocity when it comes into the field of view of the camera. If the velocity is not constant, the principle of linear momentum has to be applied and the acceleration term must be taken into account.
The data gained from the experiment is evaluated with MATLAB. Figure 6 exemplifies the data and its evaluation. The upper plot shows the position versus the time of the microrobot while passing the field of view of the camera. In this plot it can be seen if the robot is sinking at a constant velocity or if it is still accelerating. For determining the velocity, only the the constant part of the velocity is evaluated. From this selection (lower plot in Figure 6) the velocity is determined.

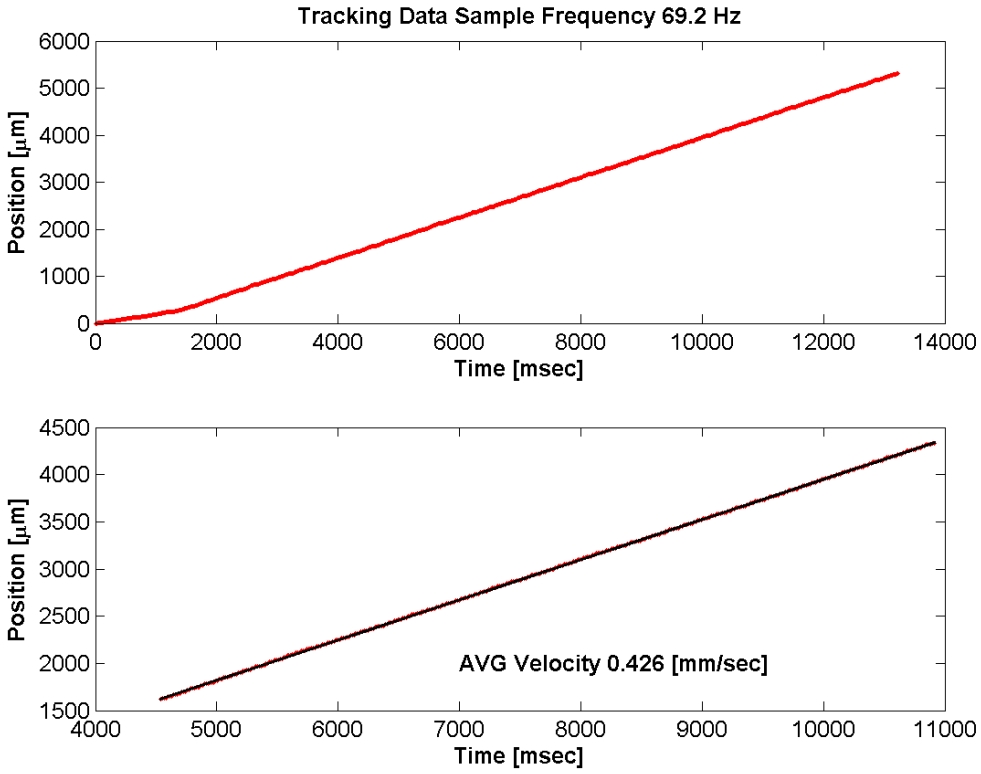

Figure 6: Data from experiment

For a constant velocity, the drag force can be determined by applying the forces equilibrium with respect to the acting forces:

$$F_{DragForce} = F_{Gravity} - F_{BuoyancyForce} \tag{4.9}$$

As seen in Section 4.2 the drag force by Stokes law is a function of the velocity of the microrobot relative to the fluid v_f, the viscosity of the fluid μ_f and a shape factor that is in the case of a sphere $3\pi D$, where D is the diameter of the sphere. Analogically, a drag number D_N is determined for the microrobot.

$$F_{DragForce} = f(v_f, \mu_f, D_N) \tag{4.10}$$

By knowing the drag force, the viscosity of the fluid and the velocity of the robot, the drag number D_N is obtained from

$$D_N = \frac{F_{DragForce}}{\mu_f v_m} \tag{4.11}$$

For a complete analysis, it also has to be checked, if the relation between the drag force and velocity of the microrobot is not square. In this case, the drag force will be written as

$$D_N = \frac{F_{DragForce}}{\mu_f v_m^2} \tag{4.12}$$

4.3.3 Experiment Results

The experiments were done with three different silicon oils[5]. Due to their known viscosity, these oils are often used for calibrating rheometers. The viscosity of the used oils was also measured at the ILW[6] at ETH Zurich. The viscosities of the three oils are around 1000 $mPa\ s$, 350 $mPa\ s$ and 100 $mPa\ s$, respectively. The exact viscosity values of these oils are temperature dependent and can be found in Appendix E.
The evaluation of the measurements shows that the assumption of a linear behavior between the drag force and the velocity of the microrobot is valid and can be applied. Figure 7 shows the box plot evaluation of the measurements using Equation (4.11).

[5]AK100, AK1'000 and AK500 silicon oils from Wacker Chemistry
[6]Institute of Food Science and Nutrition

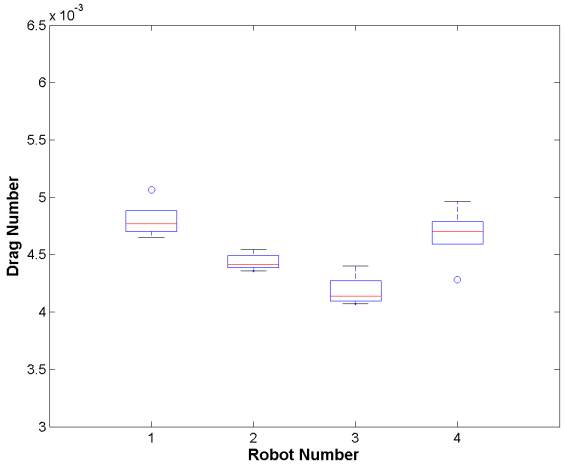

(a) Drag Number in AK100 Oil

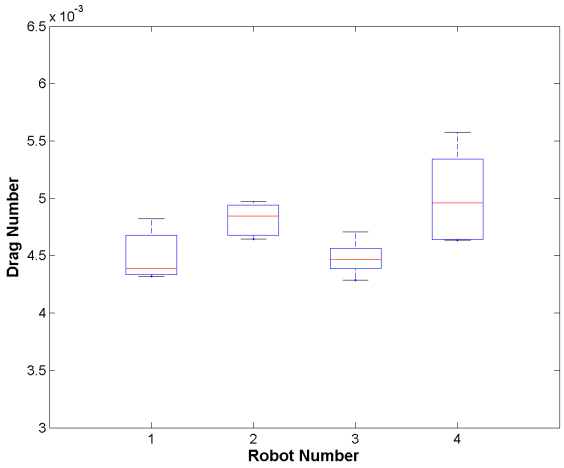

(b) Drag Number in AK350 Oil

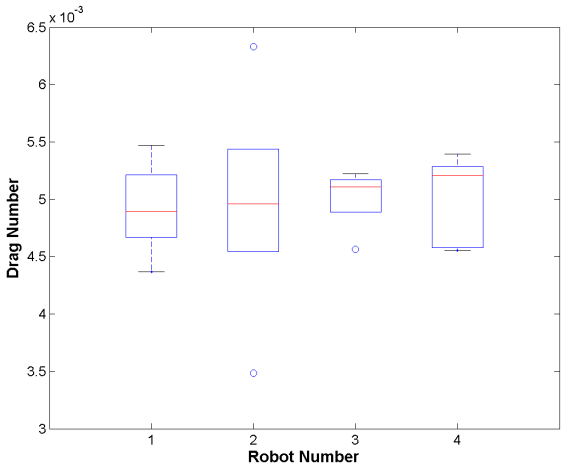

(c) Drag Number in AK1000 Oil

Figure 7: Box plots for the drag numbers

The box plot shows the distribution of the measurement results. The lower and upper lines of the "box" are equal to the 25th and 75th percentiles of the data. The distance between the top and bottom of the box is the interquartile range. The red line in the middle of the box is the median of the measured values and the "whiskers" show the extent of the rest of the data points (unless there are outliers). Outliers are signed with 'o' and are values that are more than 1 time the interquartile range away from the top or bottom of the "box".

Measurements AK100:

- The experiments performed with the AK100 oil show that robot number 1 has the highest drag number and therefore the highest drag resistance in a fluid. This value is unexpected, but can be explained by the experimental procedure. The design of the experiments allows visual control of the alignment of the robot (Figure 5). Unfortunately, robot number 1 has not been aligned to the moving direction during the experiments with the AK100 oil. The robot often has been aligned perpendicular to the moving direction or in an angle of about 45 degrees that explains the unexpected high drag number.
- The drag numbers for robot number 2, 3 and 4 are as expected. Robot number 3 has no waist and therefore a relative small surface perpendicular to the moving direction. The robots number 2 and 4 have a higher drag number than robot number 3. Both robots have a waist and therefore a large surface perpendicular to the moving direction. The higher number of robot 4 compared to robot 2 might be due to the non optimal alignment of the robot during the experiments. The pin tip of robot 2 effects like a helm and provides a good alignment of the robot. The long drawn-out shape of robot 2 could also lead to a better flow around the robot and may prevents vortexes.

Measurements AK350:

- The results show the lowest drag number value for robot number 1, followed by robot number 3, 2 and 4. This order can also be derived from the shape of the robots.

Measurements AK1'000:

- The results show ascending drag numbers for the robots number 1 to number 4.
- Actually, a higher drag number for robot number 2 than for robot number 3 has been expected. The outliers show scattered data points for the measurements of robot 2. These unexpected values might be explained by relative movements of the parts the robot is built of.

4.3.4 Experiment Results Verification

The results of the experiments were verified by doing the same experiments with spheres. The results of these experiments should lead to the same value for the drag force as calculated by applying the forces equilibrium and by calculating the drag force with Stokes', respective Oseens equation. In Table 2, the results for a measured bearing-sphere are shown. The drag force is calculated from the forces equilibrium, once with Stokes' law and once with Oseens approximation.

Measurement	**Velocity** [m/s]	**Gravity Force** [mN]	**Buoyancy Force** [mN]	**Drag Force** [mN]	**Stokes Force** [mN]	**Oseen Force** [mN]
1	0.109	6.919	8.65	6.054	5.720	6.358
2	0.1049	6.919	8.65	6.054	5.505	6.020
3	0.104	6.919	8.65	6.054	5.458	6.017

Table 2: Measurement results for a bearing-sphere

Comparison of the results for the drag force calculated from the forces equilibrium with the results from Oseens approximation, it shows, that the values deviate not more than 5%. This error is influenced by the measurement of the gravity and buoyancy force as well as the determination of the drag force by Stokes law and Oseens approximation. Taking these deviations into account, the results for the measurements are quite exact and the experiment set-up has been validated. A detailed calculation of errors can be found in Appendix C.1.

4.4 Propulsion Force

If F_g, F_b, F_d are known, the propulsion force can be determined. By applying the principle of linear momentum we obtain:

$$\begin{pmatrix} F_{Propulsion,x} \\ F_{Propulsion,y} \end{pmatrix} = \begin{pmatrix} \rho_m V_m a_{m,x} + F_d \\ \rho_m V_m a_{m,y} - F_b + F_g + F_d \end{pmatrix} \tag{4.13}$$

Where a_m is the desired acceleration of the microrobot and the gravity force is pointing in direction of the y-axis. In this force, the torque acting on the robot has not yet been taken into account.

4.5 Torque Acting on the Robot

To align the robot in the fluid, a torque has to be exerted. The determination of this torque is not easy and the calculated results have to be treated with respect to some uncertainties. The values for the principal moments of inertia have been taken from the CAD[7]-files. The robots are then modelled as planks rotated in a fluid. Effects due to friction and turbulences are neglected. Therefore, the torque can be obtained by using the principle of conservation of angular momentum:

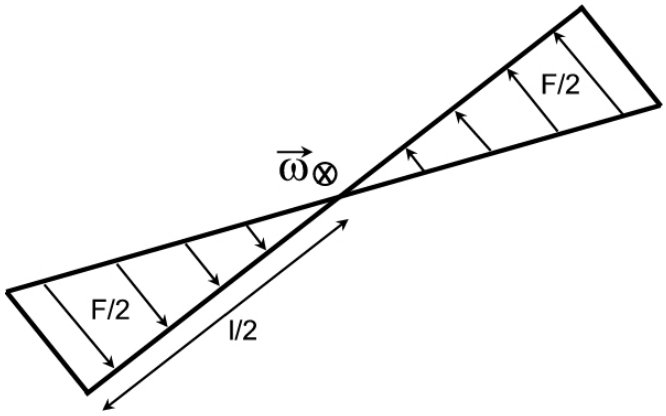

Figure 8: Model for torque calculation

[7]Computer Aided Design

$$T = J_0\ddot{\phi} + \frac{F \cdot l}{2} \tag{4.14}$$

where F is the drag force acting on the robot during rotation, J_0 the principal moment of inertia around the rotation axis and $\ddot{\phi}$ the rotational acceleration.

$$F = c_w \frac{1}{2}\rho_f A v_f^2 \tag{4.15}$$

where c_w, the drag factor for a plank, is approximately 1.1, A is the flow normal area, ρ_f the density of the fluid and v_f the velocity of the fluid relative to the plank.
Using (4.15) in (4.14) leads to

$$T = J_0\ddot{\phi} + \frac{c_w \frac{1}{2}\rho_f A v_f^2 \cdot l}{2} \tag{4.16}$$

5 Forces in Different Applications

In this section, the forces needed to propel the robot are determined for three different scenarios. The scenarios are the following:

1. The robot is operating in an artery
2. The robot is operating in the human eye
3. Laboratory prototype - robot is operating in a pig eye

5.1 Boundary Conditions

The calculations depend on some assumptions. The following values will be used [11][18][3]:

ρ_m	Density of the robot	8900 $\frac{kg}{m^3}$
ρ_{blood}	Density of blood	1055 $\frac{kg}{m^3}$
$\rho_{vitreous,human}$	Density of the human vitreous	1008.9 $\frac{kg}{m^3}$
$\mu_{vitreous,human}$	Viscosity of the human vitreous	4.9 $Pa \cdot s$
$\mu_{vitreous,pig}$	Viscosity of the pig vitreous	12.2 $Pa \cdot s$
$\mu_{blood,avg}$	Viscosity of blood	$4.7 \cdot 10^{-3} Pa \cdot s$
v_{blood}	Velocity of blood in artery	$0.7 m/s$
a_m	Acceleration of the robot	1 $\frac{mm}{s^2}$
a_m	Velocity of the robot	0.5 $\frac{mm}{s}$

The parameters of the robots are taken from Appendix A.

5.2 Robot Operating in Blood Vessel

In this scenario, the robot is employed to operate in blood vessels. Blood has approximately the same viscosity as water and therefore does not increase the drag force. On the other hand, the blood flow can be quite fast. It is important to distinguish, where the robot should operate. The blood flow in vessels is not constant but more like pulses. In the aorta, the pressure pulse wave velocity can reach up to 5 m/s, in arteries even 10 m/s [3]. Due to this high pulse velocities, it

is nearly impossible to propel and control a microrobot in large vessels. Therefore, the system should be designed to use a robot operating in blood vessels with a maximum blood velocity of approximately 0.7 m/s. Table 3 shows the values for the force needed to propel the robot in a blood vessel. The y-axis is aligned with the gravity force.

Robot	F_g **[N]**	F_b **[N]**	D_N **[m]**	F_d **[N]**	F_a **[N]**	F_x **[N]**	F_y **[N]**
1	2.203e-6	2.497e-7	0.00504	3.074e-5	2.245e-10	3.0744e-5	3.2697e-5
2	2.811e-6	3.187e-7	0.005073	3.095e-5	2.866e-10	3.0946e-5	3.3438e-5
3	2.349e-6	2.662e-7	0.0050995	3.111e-5	2.394e-10	3.1107e-5	3.319e-5
4	2.663e-6	3.019e-7	0.00525	3.202e-5	2.715e-10	3.2025e-5	3.4386e-5

Table 3: Forces acting on robot in blood

5.3 Robot Operating in a Human Eye

When the robot is operating in the human eye, the viscosity of the vitreous is boosting the force needed to propel the robot. Even though the velocity is smaller by a order of 100 due to the non flowing vitreous gel, the total force is larger due to the much higher viscosity of the human vitreous.

Robot	F_g **[N]**	F_b **[N]**	D_N **[m]**	F_d **[N]**	F_a **[N]**	F_x **[N]**	F_y **[N]**
1	2.203e-6	2.497e-7	0.00504	1.235e-5	2.245e-10	1.2348e-5	1.4301e-5
2	2.811e-6	3.187e-7	0.005073	1.243e-5	2.866e-10	1.2429e-5	1.4922e-5
3	2.349e-6	2.662e-7	0.0050995	1.249e-5	2.394e-10	1.2494e-5	1.4576e-5
4	2.663e-6	3.019e-7	0.00525	1.286e-5	2.715e-10	1.2863e-5	1.5224e-5

Table 4: Forces acting on robot in human vitreous

5.4 Robot Operating in a Pig Eye

As mentioned in Section 3, it will not be possible to do experiments with human eyes. Therefore, the prototype should be designed to use the robot in pig eyes. Concerning the dimensions, the pig eye is approximately as large as a human eye. The viscosity on the other hand is about 2.5 times higher than the viscosity of a human eye. This higher viscosity value is directly transformed to the total force

required to propel the robot. The density of the vitreous of a pig eye has been estimated to be the same as the density of a human eye vitreous.

Robot	F_g **[N]**	F_b **[N]**	D_N **[m]**	F_d **[N]**	F_a **[N]**	F_x **[N]**	F_y **[N]**
1	2.203e-6	2.497e-7	0.00504	3.074e-5	2.245e-10	3.0744e-5	3.2697e-5
2	2.811e-6	3.187e-7	0.005073	3.095e-5	2.866e-10	3.0946e-5	3.3438e-5
3	2.349e-6	2.662e-7	0.0050995	3.111e-5	2.394e-10	3.1107e-5	3.319e-5
4	2.663e-6	3.019e-7	0.00525	3.202e-5	2.715e-10	3.2025e-5	3.4386e-5

Table 5: Forces acting on robot in pig vitreous

6 Magnetic Propulsion Systems

There are different principles to propel a microrobot. It can be distinguished between internal and external propulsion systems. In an internal propulsion system, the propulsion system itself is placed on the robot (i.e. a propeller actuated by a small electromotor). In an external propulsion system, the robot is actuated passively by a device that is placed apart of the robot. External propulsion systems have the advantage that there is no energy supply necessary on the robot itself. Therefore, the time of operation is often not limited due to energy problems. On the other hand, the propulsion energy has to be transferred from the outside to the robot, which is connected with a loss of energy. In addition, there are only a few principles to propel a microrobot from outside in a wireless mode.
In this project, the focus is set on external propulsion systems based on magnetic fields.

6.1 Basic Principle

There is a magnetic force and magnetic torque acting on a magnetic object in a magnetic field

$$\vec{F} = \int_V (\vec{M} \cdot \bigtriangledown) \vec{B}_{ext} dv \tag{6.1}$$

$$\vec{T} = \int_V \vec{M} \times \vec{B}_{ext} dv \tag{6.2}$$

where V is the volume of the object, $\vec{M}$ the magnetization and $\vec{B}$ the external magnetic field. The advantage of this propulsion principle is the fact, that the human body is no barrier for magnetic fields. Therefore, this principle of propulsion system can be used to propel and steer microrobots operating inside the human body. Hereby it has to be mentioned that when building and using a system working with magnetic fields, certain guidelines and laws have to be regarded (Appendix D).
In Equations (6.1) and (6.2), it is shown that the force and the torque depend on the magnetization of the object.

The magnetization itself depends on the material properties. It can be distinguished between paramagnetic, diamagnetic and ferromagnetic materials. Paramagnetic materials have a net magnetic moment at the atomic level, but the coupling between the neighboring moments is weak. These moments tend to align with an external field, but the degree of alignment decreases at higher temperatures due to the randomizing effects of thermal agitation. Diamagnetic materials exhibit another behavior. Diamagnetic materials do not have any net atomic or molecular magnetic moment. When subjecting these materials to an external field, atomic currents are generated that rise the bulk magnetization that opposes the field. The third group, the ferromagnetic materials have a net magnetic moment at the atomic level, but unlike paramagnetic materials there is a strong coupling between neighboring moments. This coupling gives rise to a spontaneous alignment of the moments that is even increased, when the material is subjected to an external field. Ferromagnetic materials can be classified in hard and soft magnetic materials. Soft magnetic materials have a relatively low permeability and a low coercivity, which makes them easy to magnetize. Hard magnetic materials on the other hand have a relatively high permeability and a high coercivity, which makes them more difficult to magnetize and demagnetize. Figure 9 shows the B-H curve for a soft and hard magnetic material.

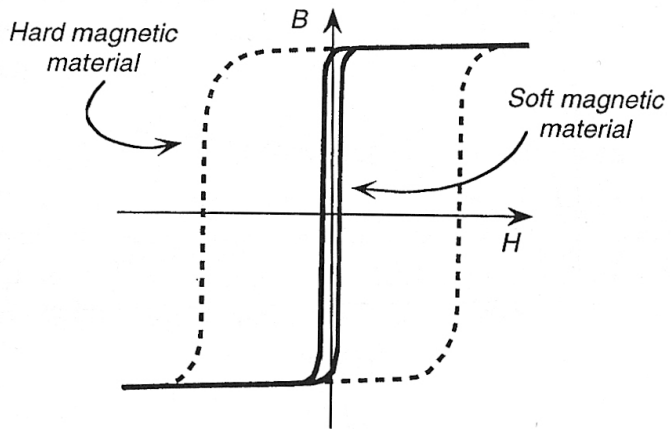

Figure 9: Soft and hard magnetic material behavior [5]

Therefore, when using a steering system for microrobots based on magnetic forces, the material and geometrical properties of the robot must be well known.

7 Magnetic Propulsion Force

After that the field of application has been defined, the actual magnetic force needed to propel the robot can be determined. In Section 6.1 the relation between the force, torque and external field has been shown. By applying Equations (6.1) and (6.2), the required magnetic fields can be calculated.
There are basically two different parts of the field, that are relevant. The magnitude of the field is relevant for the torque while the gradient of the field is relevant for the propulsion. If an object should be moved that is not magnetized by nature, the magnitude is also used for magnetizing the object. Solving (6.1) along one axis leads to

$$\bigtriangledown B_{ext} = \frac{F}{\int\limits_V M dv} \tag{7.1}$$

where $\bigtriangledown B_{ext}$ is the gradient of the magnetic field, $\int\limits_V dv$ the volume and M the magnetization of the robot. Therefore, the larger the volume and the higher the magnetization, the weaker is the required magnetic field gradient.
Solving (6.2) along one axis leads to

$$B_{ext} = \frac{T}{\int\limits_V M sin(\phi) dv} \tag{7.2}$$

where ϕ is the angle between the direction of the magnetization and the direction of the external field. Also here, a high magnetization as well as a large volume can reduce the required field strength.
As mentioned above, if one works with robots that need to be magnetized, the magnitude of the magnetic field has to be chosen to be strong enough to reach the desired magnetization. Because the propulsion force as well as the torque are dependent on the magnetization of the robot, the highest possible magnetization will be preferred. Therefore, the field should be strong enough to cause a saturating magnetization of the robot. This magnetization is on one hand depending on the material of the robot and on the other hand depending on the shape of the object.

7.1 Magnetization of the Robot

The robots used at the IRIS are made of nickel, which is a soft magnetic material. By nature, the robots are not magnetized and therefore must be magnetized by an external field (Appendix B.6). For simple shapes there exist formulas that allow to determine the induced magnetization by an external field analytically. Because the robots used at IRIS do not have a trivial shape the magnetization cannot be determined analytically. Therefore, experiments were performed to determine the magnetization. These experiments will show the relation between an external field and the induced magnetization of the robots. Furthermore, the saturation magnetization will be determined.

7.1.1 Measurements Using Forces Equilibrium

For the experiment, a oil filled chamber is placed at the center of of a Helmholtz and Maxwell coil pair. A microscope camera is used to track the position of the microrobot. In this configuration, the Helmholtz coils are generating the field for magnetizing the robot where the Maxwell coils create the gradient field for levitating the robot. By knowing the strength of the two fields, the magnetization of the robot can be calculated.

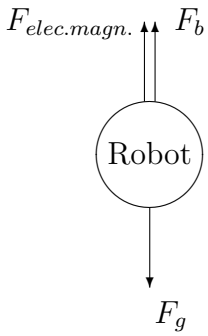

Figure 10: Steady state configuration

By solving the forces equilibrium equation, the magnetization is determined from

$$\begin{aligned} F_{elec.magn.} &= F_g - F_b \\ V_m M \bigtriangledown B &= V_m \rho_m g - V_m \rho_f g \end{aligned} \tag{7.3}$$

$$M = \frac{V_m \rho_m g - V_m \rho_f g}{V_m \bigtriangledown B} = \frac{g(\rho_m - \rho_f)}{\bigtriangledown B} \tag{7.4}$$

The experiment procedure was the same for all four kinds of robots currently used at IRIS.

The current through the Helmholtz coil is kept fixed while the current through the Maxwell coil is controlled by the computer. A PID[8] control loop is established through the visual feedback of the camera to levitate the robot at stabilize its position at the center of the chamber against gravity and buoyancy forces (Figure 11). When the robot's position is stabilized the current through the Maxwell coil is recorded. To analyze the behavior of the magnetization in the external magnetic field, the experiment is done at different field strengths of the Helmholtz field.

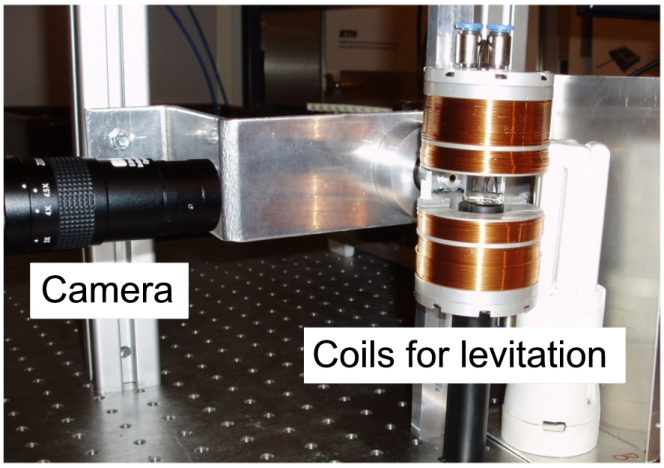

Figure 11: Magnetization test set-up

It is important to note, that the robot material magnetization curve has a hysteresis behavior. Therefore, the experiment started with no current flowing through

[8]Proportional plus Integral plus Derivative

the Helmholtz coil that generate the magnetization field. Then the current has been continuously increased until the maximum current for the coil wire has been reached.
To ensure that the robot was stabilized right at the center of the two coils, the field has been measured with a hall probe at the position, where the robot was stabilized (at the center point between the two coils, the Maxwell field is zero and the Helmholtz field reaches its maximum).

7.1.2 Experiment Results

Figure 12 shows the current in the Helmholtz coils versus the currents in the Maxwell coils for the steady state configuration. The circles indicate the measured points, the lines show a linear-in-the-parameters regression for the measurement points of each robot.

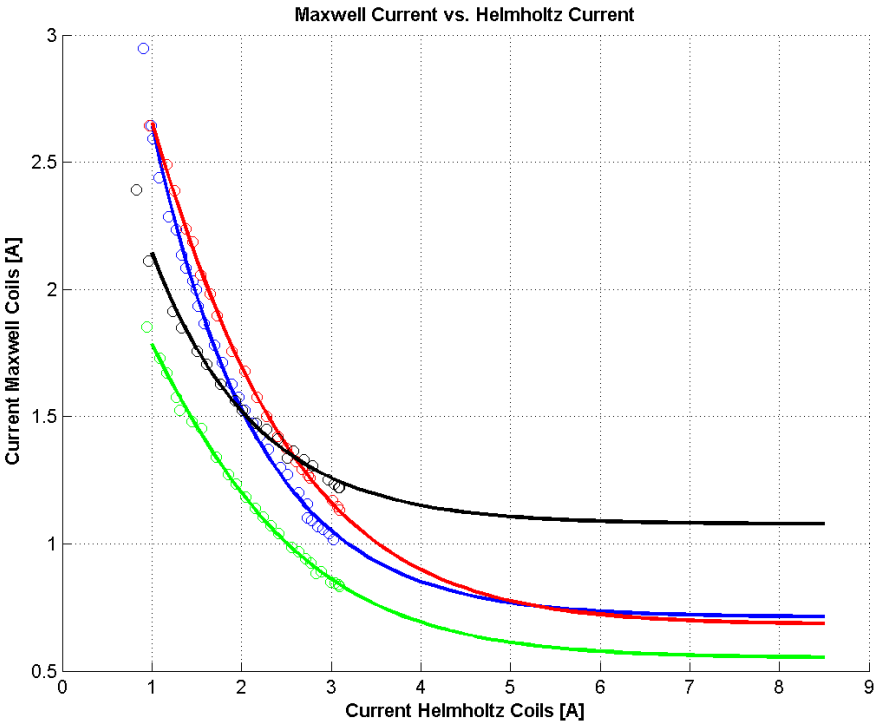

Figure 12: Currents in the coils for steady state configuration. Robot 1 = blue, robot 2 = red, robot 3 = green, robot 4 = black

As expected, the results show that the relation between the current in the Helmholtz coils and the current in the Maxwell coils is not linear. Since the current in the Helmholtz coils and the Maxwell coils is known, the strength of the two fields can be determined.
The coils used for the experiments do not have an exact Helmholtz configuration. Therefore, the coils are modeled from single wire turns and the field is evaluated numerical with MATLAB. The Maxwell coils in the set-up have 487 wire turns where the Helmholtz coils have 245 wire turns. Manual measurements of the field with a hall sensor were made to check out the calculated results. Figure 13 shows the measured and calculated field created by the Maxwell coils used for the magnetization determination at two different currents.

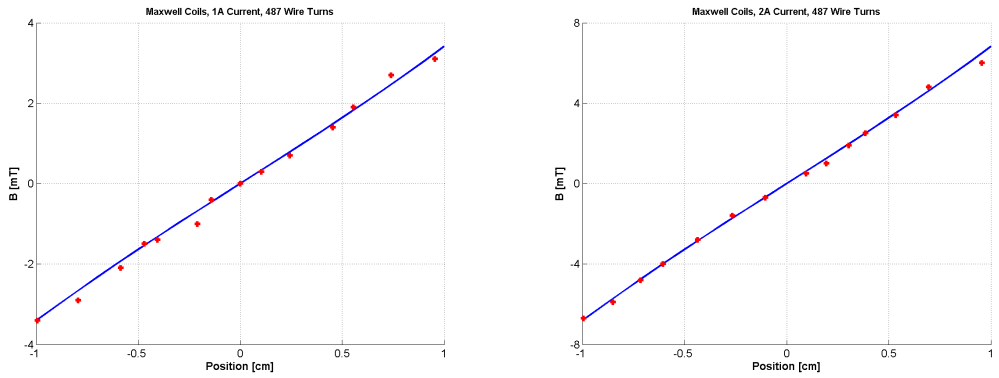

(a) 1A Current (b) 2A Current

Figure 13: Calculated and measured values of magnetic field along the central axes of Maxwell coils. Measured values are indicated by '+' signs.

From these results the gradient of the Maxwell field can be extracted to evaluate the magnetization of the robots. Figure 14 shows the relation between the magnetization of the robots and the current in the Helmholtz coils.

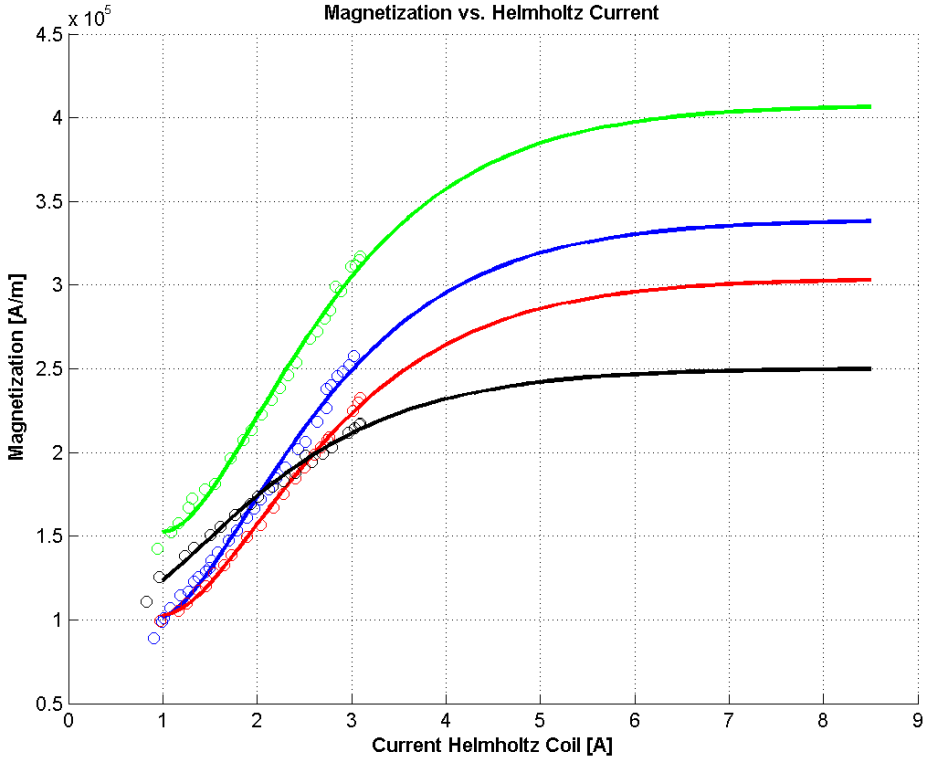

Figure 14: Magnetization vs. Helmholtz Current. Robot 1 = blue, robot 2 = red, robot 3 = green, robot 4 = black

The relation between the current in the Helmholtz coil pair and the generated field is linear and has also been confirmed experimentally. Figure 15 shows the measured Helmholtz field at the center between the two coils.

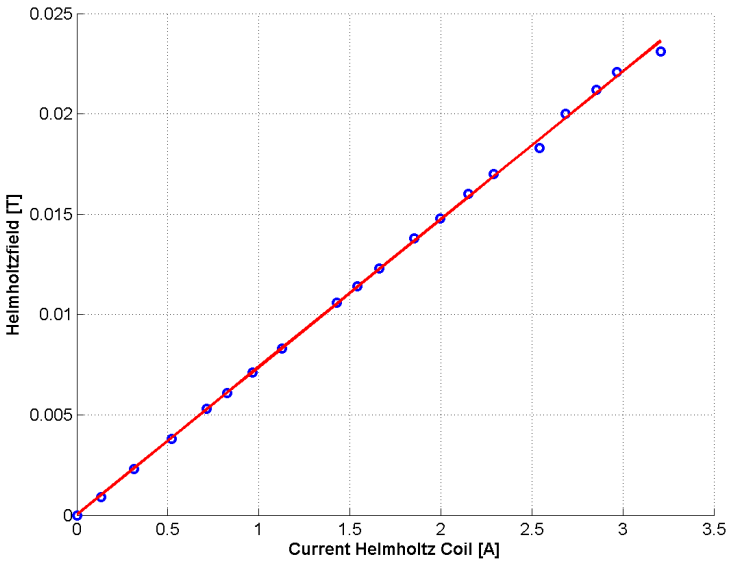

Figure 15: Measured Helmholtz field

7.1.3 Discussion

The insights gained by the measurements using the forces equilibrium show consistent results, if the determined saturation magnetization is compared with the shape of the robot. As described in Section B.6 the magnetization is depending on the shape. For ellipsoidal shapes, the magnetization can even be analytically determined [5]. The shape of the studied robots can be approximated by an ellipsoid. When the demagnetization factor for such an approximated elliptic shape is determined for the individual robots, the highest demagnetization factor is found for robot number 4, the lowest for robot number 3 which is consistent with the magnetization order of the experimental results.
The advantage of determining the magnetization using the forces equilibrium is that the magnetization experiment does not depended on the volume of the robot. Equation 7.4 shows that the volume is cancelled out. Unfortunately, the coils used for generating the magnetization were not strong enough to reach the region, where the strongly increasing part of the magnetization curve is leveling down to the saturation magnetization value. Therefore, the curve has been interpolated by a linear-in-the-parameters-regression and the results have to be treated carefully.

7.1.4 Coercivity Spectrometer

From the experiments done by evaluating the forces in the steady state configuration, no exact values for the magnetization saturation could be obtained. Therefore, the saturation magnetization was also determined at the Institute of Geophysics at ETH Zurich. Using a coercivity spectrometer the B-H behavior of the four types of robot was determined. Figure 16 shows the coercivity spectrometer used for the measurements [8].

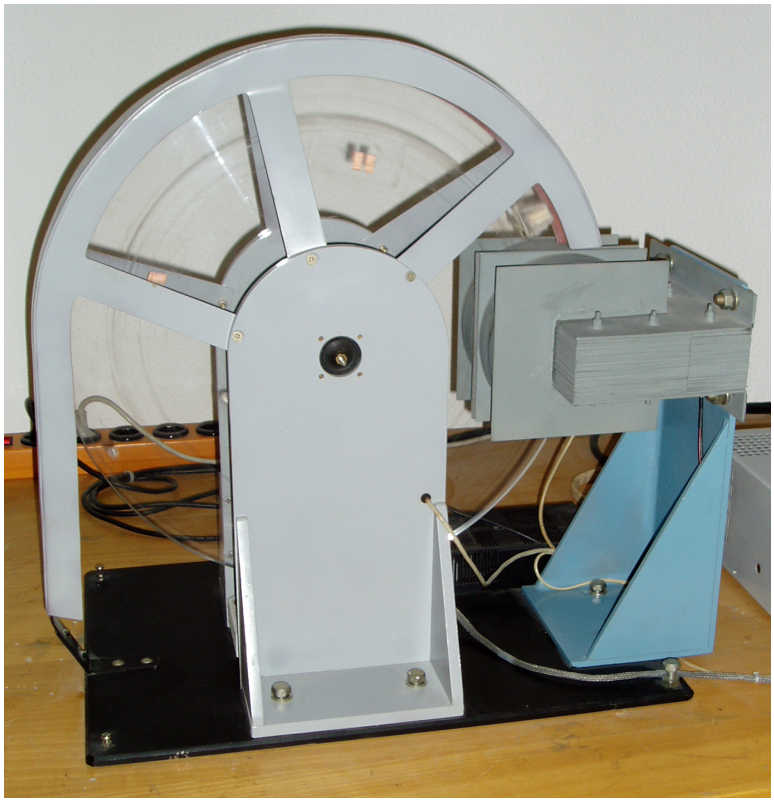

Figure 16: Coercivity spectrometer

In this spectrometer, the saturation moment[9] is determined. By dividing the saturation moment through the volume, the magnetization of the robots can be determined.
The results of the measurements done with the coercivity spectrometer are shown in Figure 17.

[9]In cgs-system measured in emu = electromagnetic units

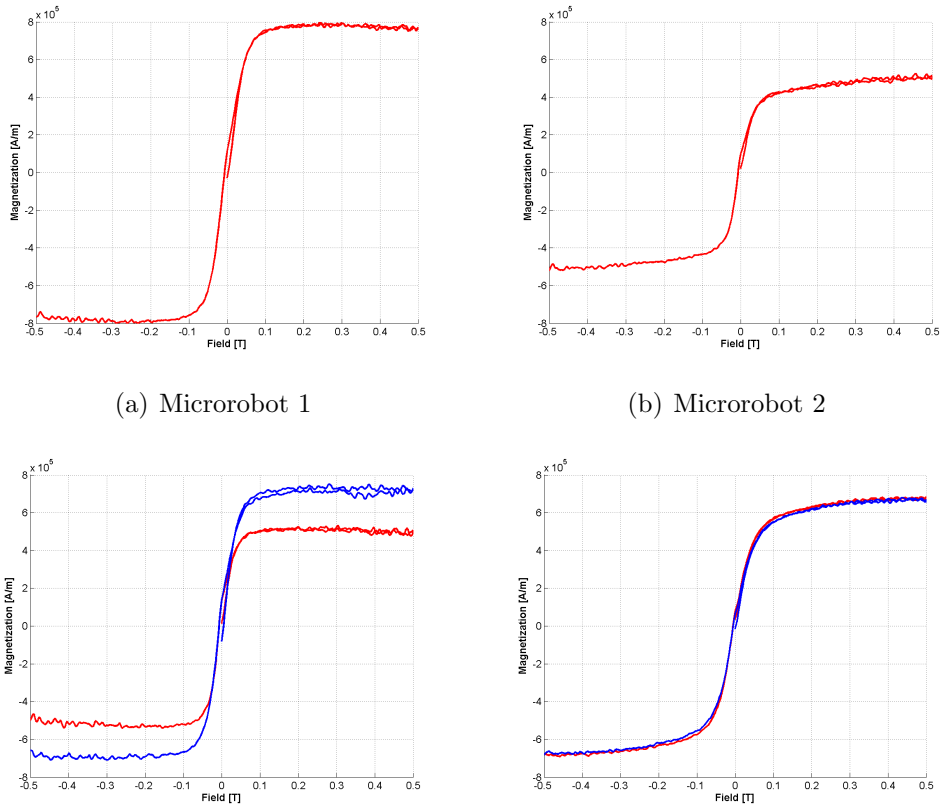

(a) Microrobot 1

(b) Microrobot 2

(c) Microrobot 3

(d) Microrobot 4

Figure 17: Magnetization of the microrobots

Four different types of robots have been studied. Robot types number 3 and 4 have been analyzed twice with two different robots. The results of these measurements lead to different values for the saturation magnetization than the ones determined in Section 7.1.2.

7.1.5 Discussion and Conclusions

The difference between the two sets of values for the saturation magnetization can be explained by the unknown parameters for the magnetization determination. In the experiment performed to determine the magnetization by applying the "forces equilibrium", the reachable strength of the Helmholtz field has been limited and therefore, an interpolation over a wide range has been necessary. On the other hand, using a coercivity spectrometer requires exact information about the volume of the robot. The volume of the robot can either be derived from the

exact dimensions of the parts the robot is made from or it can be calculated with the weight of the robot (including the glue that is used to hold the parts together) as well as the density of the robot and the density of the glue. Determining the volume as well as determining the weight is very demanding due to the small dimensions.
Another important point is the precision of the assembled robots. Figure 17(c) shows different magnetization values for the same type of robot. Examination of the two measured robots under the microscope explains the two different values for the same robot model. The tips of the robot with the lower magnetization value are not precisely sticking together. The tips are slightly missaligned, which leads to multiple magnetic poles on the robot (Figure 18).

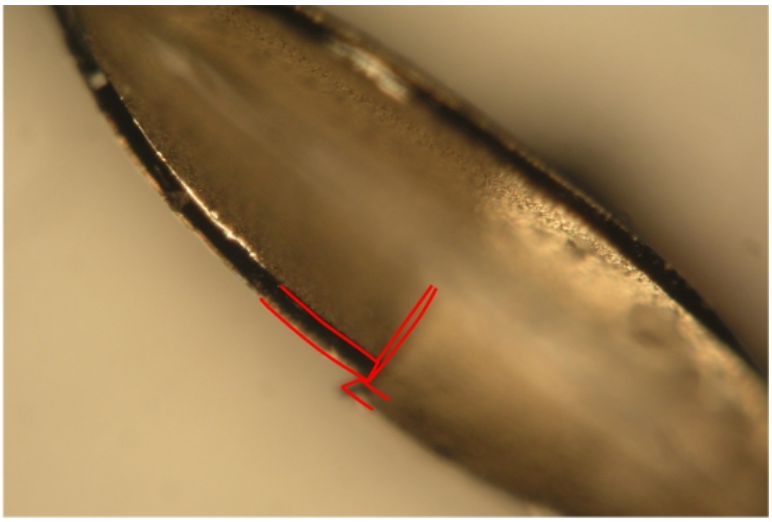

Figure 18: Missaligned wings of robot 3

Due to the experiments done by applying the steady state forces equilibrium and the analogy between the robots shape and the ellipsoid, the order of the saturation magnetization will be the one determined in the first experiment.
On the other hand, the coercivity spectrometer experiments show another magnetization order and the magnitude of the saturation value cannot be concluding be determined. What can be obtained from the experiments done with the coercivity spectrometer is the value of the external field, were the magnetization saturation is reached. Depending on the robot model, the saturation magnetization is already reached when applying a field of approximately 200 mT. Figure 19 shows the percentage magnetization saturation dependent on the external field.

The data has been taken from the coercivity spectrometer experiment results and smoothen with a filter.

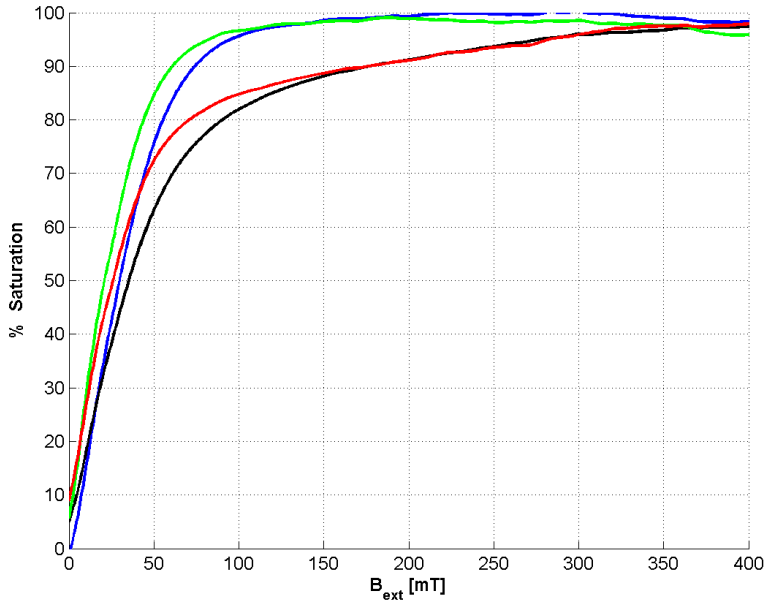

Figure 19: Percentage magnetization saturation. Robot 1 = blue, robot 2 = red, robot 3 = green, robot 4 = black

Comparing these values with the magnetization values from the experiment done with magnetic levitation, the same order concerning the velocity of reaching the saturation magnetization is reached.

The results gained by the experiments give a good approximation for determining the required field strength for a steering system based on magnetic fields. Nevertheless, if exact values for the magnetization saturation are needed, an improvement of the steady state forces equilibrium experiment is proposed. Stronger coils would also allow to measure values close to the saturation point. These additional measuring points would allow to interpolate missing points and to fit a reliable magnetization curve.

7.2 Required Field Strength

The needed field strength for the different fields of application can now be determined with respect to the uncertainty of the magnetization of the IRIS microrobots. Because the values determined for the saturation magnetization by the forces equilibrium experiment described in Section 7.1.1 are lower than the values from the coercivity spectrometer, these values (conservative assumption) are taken to determine the needed field strength for the propulsion system.
Concerning the magnetization field, the values from the coercivity spectrometer experiment are taken. This experiment shows, that at an external field strength of about 200 mT, the magnetization saturation is more or less reached for robot number 1 and 3. For robot number 2 and 4, the saturation magnetization is only reached at about 400 mT. Having an as high as possible saturation, the gradient field is reaching its lowest value. It could also be thought of not totally magnetize the robots. Due to the nonlinear magnetization behavior, the last 10% of saturation need an unproportional higher field, than the previous 90%. By applying a field of only approximately 100 mT, a magnetization saturation of already about 90% in the case of robot 1 and 3 can be reached (Figure 19).

For the calculation of the required field strength, the following values were used:

Robot	**Volume** $[m^3]$	**Saturation Magnetization [A/m]**	**External Magnetization Field [T]**
1	$2.52 \cdot 10^{-11}$	$3.4 \cdot 10^5$	0.2
2	$3.22 \cdot 10^{-11}$	$3.0 \cdot 10^5$	0.4
3	$2.69 \cdot 10^{-11}$	$4.1 \cdot 10^5$	0.2
4	$3.05 \cdot 10^{-11}$	$2.5 \cdot 10^5$	0.4

Table 6: Robot parameters

Applying these assumptions, the following field strength could be determined for the different applications.

Robot	**Volume** $[m^3]$	**Magnetization** $[A/m]$	$\bigtriangledown B$ **due to** F_x [T/m]	$\bigtriangledown B$ **due to** F_y [T/m]
1	2.523e-011	340000	1.93	2.16
2	3.22e-011	300000	1.73	1.98
3	2.69e-011	410000	1.52	1.71
4	3.05e-011	250000	2.27	2.57

Table 7: Robot in blood

Robot	**Volume** $[m^3]$	**Magnetization** $[A/m]$	$\bigtriangledown B$ **due to** F_x [T/m]	$\bigtriangledown B$ **due to** F_y [T/m]
1	2.523e-011	340000	1.44	1.67
2	3.22e-011	300000	1.29	1.54
3	2.69e-011	410000	1.13	1.32
4	3.05e-011	250000	1.69	2

Table 8: Robot in human vitreous

Robot	**Volume** $[m^3]$	**Magnetization** $[A/m]$	$\bigtriangledown B$ **due to** F_x [T/m]	$\bigtriangledown B$ **due to** F_y [T/m]
1	2.523e-011	340000	3.58	3.81
2	3.22e-011	300000	3.2	3.46
3	2.69e-011	410000	2.82	3.01
4	3.05e-011	250000	4.2	4.51

Table 9: Robot in pig vitreous

To align and saturate the robot, the magnitude of the field is relevant. Evaluation of Equation (4.16) in Section 4.5 shows that the needed torque is in the order of 10e-10 Nm and therefore the needed field strength for aligning the robot would be in the order of a few mTesla. Therefore, the magnitude of the field is not given by the torque needed for aligning the robot but by the field needed for magnetizing the robot.

7.3 Reduction of the Field Strength

The calculated fields for propelling a microrobot in a pig eye are very strong. Especially the required gradient field of 4.5 Tesla/m is very strong and hard to reach. Therefore, possibilities for reducing the field strength are discussed.
The required field strength has been calculated from Equation (6.1). There it can be seen, that the required gradient of the field is linearly dependent on the required force and is inversely proportional to the volume and the magnetization of the robot. Assuming the force can not be reduced, there are two possibilities left to reduce the required field: Either by increasing the volume or by increasing the magnetization of the robot. Because the main part of the required force is given by the drag force that is also dependent on the shape and therefore the volume of the robot, the first possibility to reduce the magnetic field gradient will be to increase the magnetization of the robot.
The magnetization of the robot can only be as high as the saturation magnetization of the robot. For the calculations done in the previous section, it has been assumed, that the robot will already be magnetized to its saturation magnetization. Therefore, to get a higher magnetization, the material of the robot must be changed to a material with a higher magnetization saturation. It can also be considered to use a permanent magnet material for the robot. In this case, it would not be necessary to apply a magnetic field to magnetize the robot.
On the other hand, it has to be kept in mind, that in the future also some sensors and actuators should be placed on the robot and that these may be incompatible with a permanent magnet material.
The second possibility to reduce the magnetic gradient field is the volume. Having a larger volume would also reduce the needed field gradient. On the other hand, one must be careful that due to the larger volume the forces, especially the drag force of the robot, are not increasing by the same order as the magnetic force is enlarged by the larger volume. Another point is the application the robot is used for. If the microrobot machines should be used for minimal invasive operations, the volume is limited due to this external boundary condition.

Concluding, it can be said, that there are possibilities to reduce the needed magnetic field strength. But the decision for one or the other solution is dependent on the field of application and the future design of the robot and its equipment.

8 Experiments for Force Verification

In the previous sections, the forces acting on a microrobot in different applications have been determined. Furthermore, the required magnetic field strength has been calculated. For this calculations, assumptions about unknown parameters have been done. Especially the fluid dynamic behavior of the vitreous is stamped by some uncertainties. To verify these calculated forces, experiments were done with a pig eye.

Figure 20: Robot in a pig eye

8.1 Goal of the Experiment

In the experiment, a microrobot was aligned and propelled in a pig eye by applying a magnetic field. For that purpose, eyes from pigs that have been slaughtered just a few hours ago, were used. It is important that the eyes are relatively fresh. It can be shown that the viscosity of the vitreous is changing after the slaughter. The more time has elapsed after slaughtering the less viscous is the vitreous [11]. The eyes for the experiment were not treated with any appliances. In the dissection, just the lens has been removed to have access to the vitreous body.
The magnetic fields used in the experiment were generated by permanent magnets. To be sure about the strength and progression of the magnetic field of the permanent magnets, the field has been measured and analytically calculated. To measure the magnetic field strength a special set-up has been used.

8.2 Permanent Magnet Measurement

The magnetic field of the permanent magnet was measured using a Suttter MP-285 Micromanipulator and a Hirst GM05 Gaussmeter. Figure 21 shows the test set-up used for the experiments.

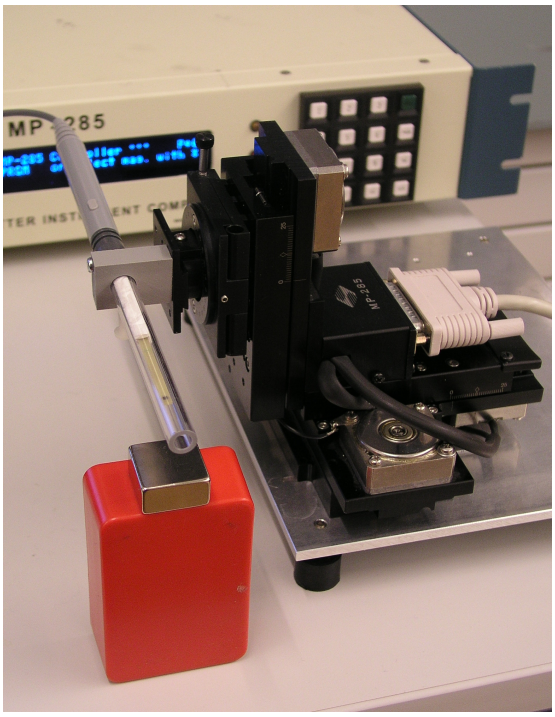

Figure 21: Magnet measurement set-up

The hall probe of the gaussmeter is attached to the arm of the micromanipulator that is computer controlled moving at different heights over the surface of the magnet. With the hall probe, the field is measured by an accuracy of 0.1 mTesla. Figure 22 shows the calculated and measured field of a bar magnet 7.5 mm above the magnet surface. The edge length of the square bar magnet is 20 mm and the height 10 mm. It can be seen that the measured and analytically determined B-fields are matching.

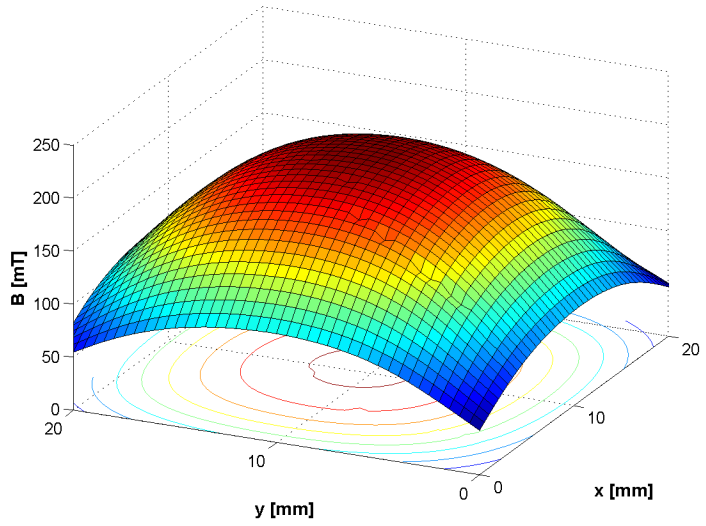

(a) Measured B-field

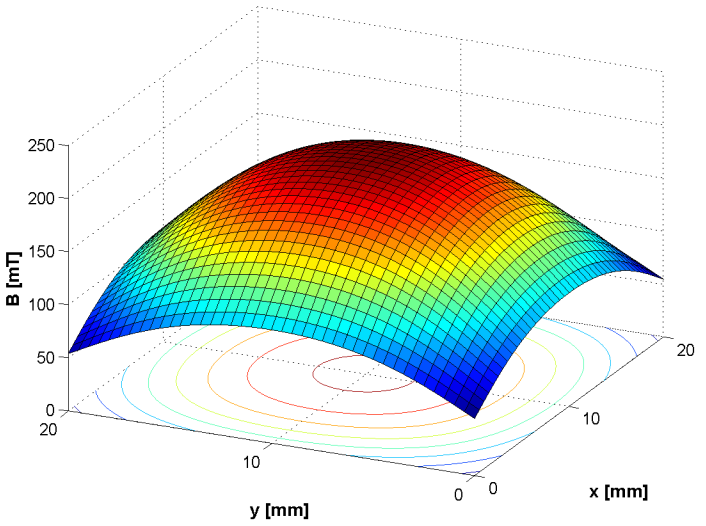

(b) Calculated B-field

Figure 22: Comparison between measured and calculated B-field of a bar magnet.

8.3 Aligning the Robot

The scope of this experiment was to prove that it is possible to align a microrobot in a homogeneous field without moving it to one or the other direction. For this experiment, two strong permanent magnets have been arranged in a way that

the magnetization direction of the two magnets is pointing in the same direction. Figure 23 illustrates the arrangement of the permanent magnets around the pigs eye. To have a better control of the alignment of the robot, the experiment was done under the microscope.

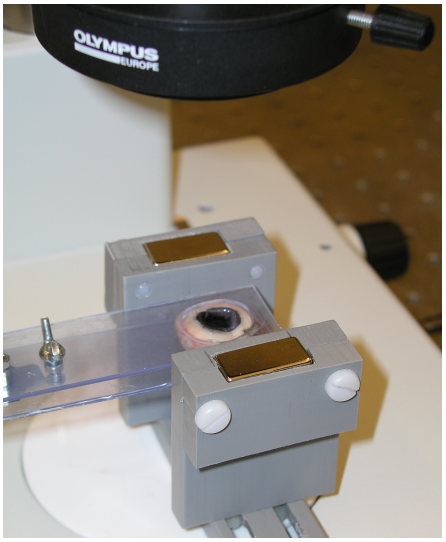

Figure 23: Set-up for magnetic experiment

The experiment showed, that the robot can be well aligned in all directions by applying a homogeneous field generated by two permanent magnets. Depending on the distance between the two magnets, the region where the robot can be aligned without moving against one or the other magnet, is larger or smaller.

8.4 Propelling the Robot

For this experiment, the robot was put into the vitreous while no external field was applied. While getting closer with a permanent magnet, it was observed that the robot started to move towards the magnet due to the increasing gradient. Depending on the robot model, the robot started to move, when the magnet was approximately 4 up to 5 centimeters away from the robot. When keeping the distance between the robot and the magnet constant at four centimeters, the robot strands after having moved a few millimeters. When removing the magnet, the robot is pulled back to the starting point due to the elastic forces inside the vitreous. Even when getting very close (app. 1 cm) to the robot with the magnet, the robot is moving back after removing the magnet. Therefore, it can

be concluded, that the robot is not moving through the vitreous but that it is just pushing the whole part of the vitreous in an elastic manner. It has also been tried to move the robot through the vitreous by letting the robot wiggle while moving forward. But also with that the robot did not move relatively to the ambient vitreous.

Among the robots tested in the pigs eye, there were also robots which magnetization has been measured with the coercivity spectrometer (Section 7.1.4). For these robots, the magnetic force in the external field can be well determined. Calculating the force i.e. for a measured robot of type 4 leads to the magnetic propulsion force shown in Figure 24 .

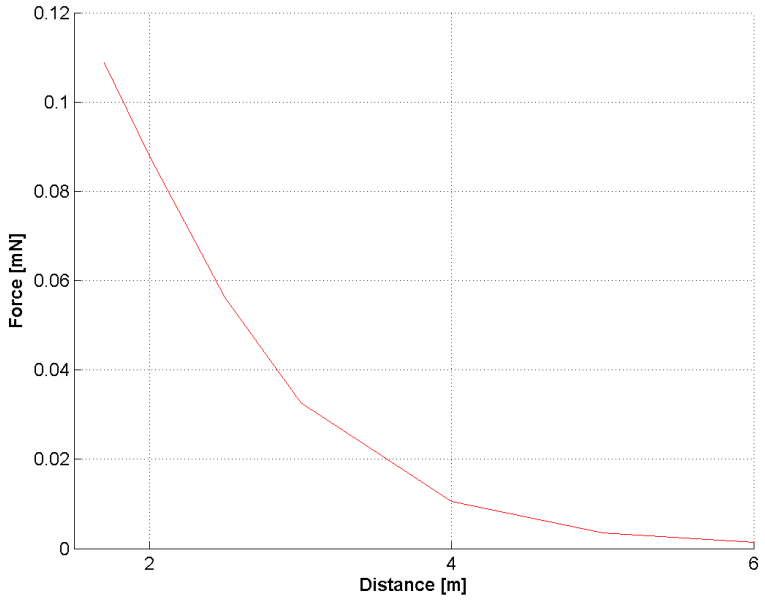

Figure 24: Magnetic force against distance

A comparison of these results with the predicted forces in Section 5.4 shows that the calculated force of 35 μN is reached at a distance of 2.95 cm between the robot and the magnet.

8.5 Conclusions

The experiments done with the pigs eye show some interesting results. First of all, it could be shown that it is possible to align and propel a microrobot inside an eye by applying external magnetic fields that lead to a magnetization and propulsion force. Another important conclusion is the fact, that the spring term in the viscoelastic model of the eye must not be neglected when calculating the forces acting on a microrobot in the eye.
When comparing the analytically calculated forces with the experiments it can be seen, that the actually needed forces will be a little bit higher due to the spring term of the vitreous viscosity model. To exactly determine the needed forces, further experiments with pig eyes are recommended. The better the understanding about the vitreous behaviour and the better the viscoelastic model for the determination of the forces acting on the robot inside an eye, the more exact can the needed magnetic fields be determined. Otherwise, the fields needed for propulsion must be conservatively defined, which drives the strength and therefore the costs for the system exponentially up.

9 Generating Magnetic Fields

There are different possibilities to generate magnetic fields. The most common field generation devices are air core coils, electromagnets and permanent magnets. In the following section, different kinds of these field generation devices are discussed and compared.

9.1 Air Core Coils

One possibility to generate magnetic fields is using air core coils. In this subsection, an overview of different coil designs is given. The analysis of these coils should help to find the optimum solution for a system based on air core coils.

9.1.1 Helmholtz Coils

For aligning the microrobot along its central axis, a uniform magnetic field is needed. That magnetic field is created by two coils in an so called Helmholtz configuration.
In an Helmholtz configuration the distance between the two coils is chosen to be the same as the radius of the coils. Both coils are carrying the same current in the same direction. In that configuration the magnetic field is most uniform in the vicinity of their midpoint [9].
The strength of the magnetic field along the z-axis can be calculated from

$$B_z = \frac{\mu_0 I a^2}{2((\frac{d}{2} - z)^2 + a^2)^{\frac{3}{2}}} + \frac{\mu_0 I a^2}{2((\frac{d}{2} + z)^2 + a^2)^{\frac{3}{2}}} \tag{9.1}$$

Evaluating the field at the midpoint (z=0) when choosing the coil distance d between the two coils the same as the coils radius a leads to

$$B_{z|z=0,d=a} = \frac{8\sqrt{5} I \mu_0}{25a} \tag{9.2}$$

Figure 25 shows the magnetic field of the Helmholtz coil pair along the z-axis (I = 1A, a=0.1 m).

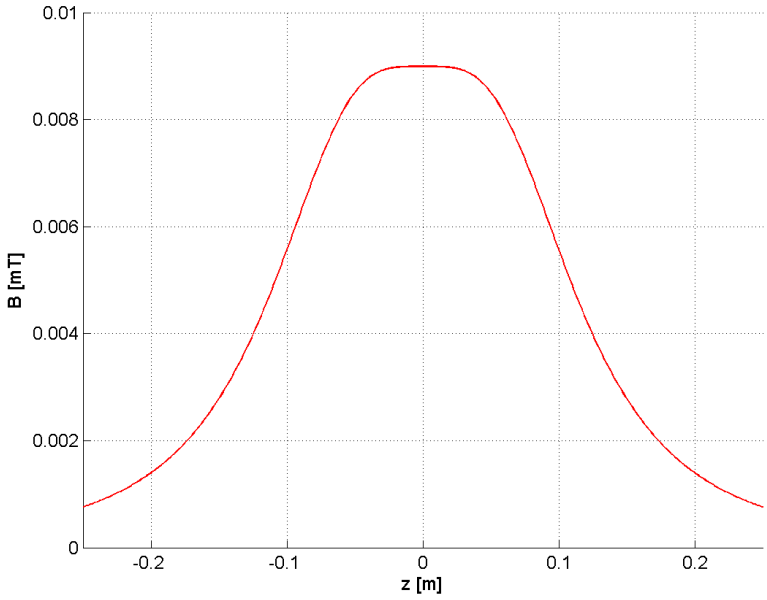

Figure 25: Magnetic field of the Helmholtz coil pair

9.1.2 Maxwell Coils

To propel the microrobot along its axis, a gradient field is needed. The easiest way to create an uniform magnetic gradient field can be achieved with a so called Maxwell coil pair. In this configuration there are two identical coils carrying the current in opposite directions. The distance between the two coils is chosen to be $\sqrt{3}a$ with a as the denoting radius of the coil loops. In this configuration a uniform gradient field around the center of the two coils can be reached [9].
The strength of this field at the midpoint between the two coils is zero. That can be derived from

$$B_z = \frac{\mu_0 I a^2}{2((\frac{d}{2} - z)^2 + a^2)^{\frac{3}{2}}} - \frac{\mu_0 I a^2}{2((\frac{d}{2} + z)^2 + a^2)^{\frac{3}{2}}} \tag{9.3}$$

when evaluating the field strength at the midpoint between the two coils ($z = 0$) and inserting for the distance between the coils $d = \sqrt{3}a$.
Figure 26 shows the magnetic field of a Maxwell coil pair along the z-axis (I = 1 A, a=0.1 m).

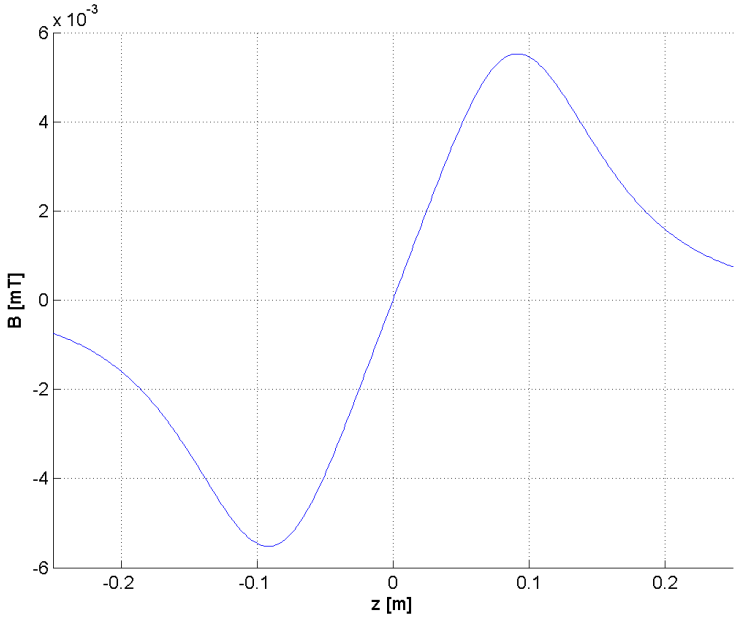

Figure 26: Magnetic field of the Maxwell coil pair

For the propulsion of the microrobot, the gradient of the field is important (Section B.6.1). The differentiation of the magnetic field along the z-axis in the Maxwell configuration is obtained to:

$$\frac{dB_z}{dz} = \frac{3\mu_0 I a^2}{2}\left(\frac{\frac{d}{2}-z}{\left((\frac{d}{2}-z)^2+a^2\right)^{\frac{5}{2}}} + \frac{\frac{d}{2}+z}{\left((\frac{d}{2}+z)^2+a^2\right)^{\frac{5}{2}}}\right) \tag{9.4}$$

Evaluating (9.4) at the midpoint ($z = 0$) in the Maxwell configuration ($d = \sqrt{3}a$) leads to:

$$\frac{dB_z}{dz}_{|z=0,d=\sqrt{3}a} = \frac{48\sqrt{21}\mu_0 I}{343a^2} \tag{9.5}$$

for the gradient of the field. It can be shown, that the gradient is uniform to 5% within a sphere of radius 0.5 a.

9.1.3 Superimposed B-Field

To be able to align and propel the robot, the fields generated by the Helmholtz and Maxwell coils are superimposed. Figure 27 shows the fields generated by the Maxwell and the Helmholtz coils as well as the superimposed field along the z-axis (I=1 A, a=0.1 m).

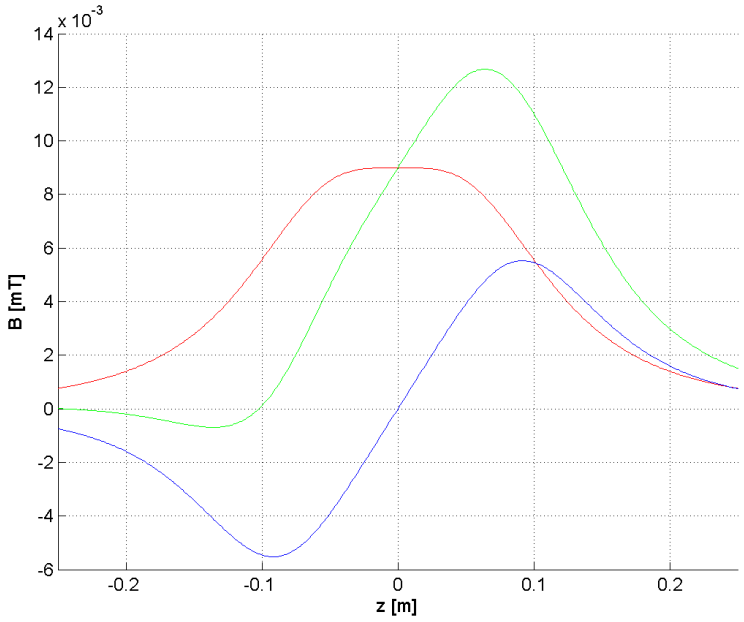

Figure 27: Helmholtz (red), Maxwell (blue) and superimposed magnetic field (green)

The torque on the robot is dependent on the B-field whereas the magnetic force is dependent on the gradient of the B-field (Equations (B.25),(B.24)). Therefore the gradient of the superimposed field has to be evaluated. Figure 28 shows the gradient of the magnetic field along the z-axis (I=1A, a=0.1 m).

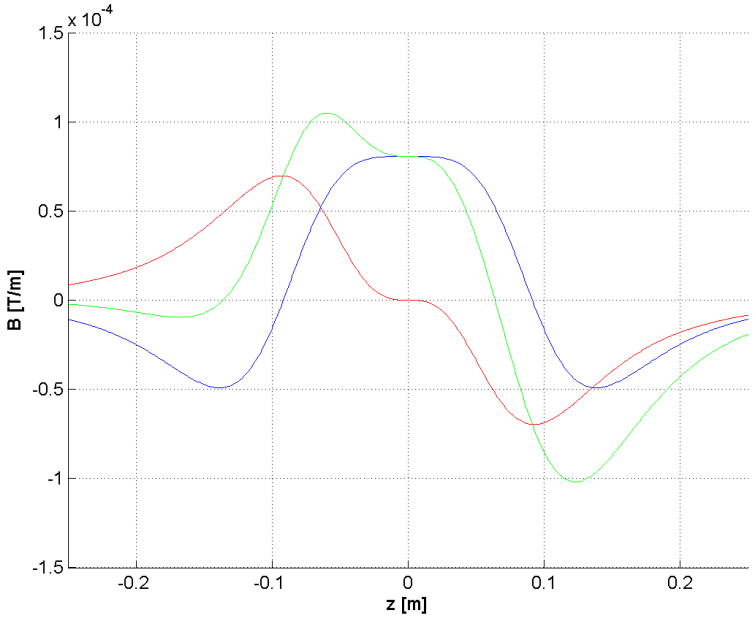

Figure 28: Gradient of Helmholtz (red), Maxwell (blue) and superimposed magnetic field (green)

Applying the superimposed field, the force and torque on a robot along the z-axis can be calculated. Figure 29 shows exemplary the force and torque on a robot with a magnetization of $2.4 \cdot 10^5$ A/m and a volume of $2 \cdot 10^{-11}$ m^3 (I = 1A, a=0.1 m).
It can also be shown (Figure 30) that the force on the robot is zero, when the Maxwell coils are deactivated ($I_{Maxwell} = 0$ A, $I_{Helmholtz} = 1$ A, a=0.1 m).

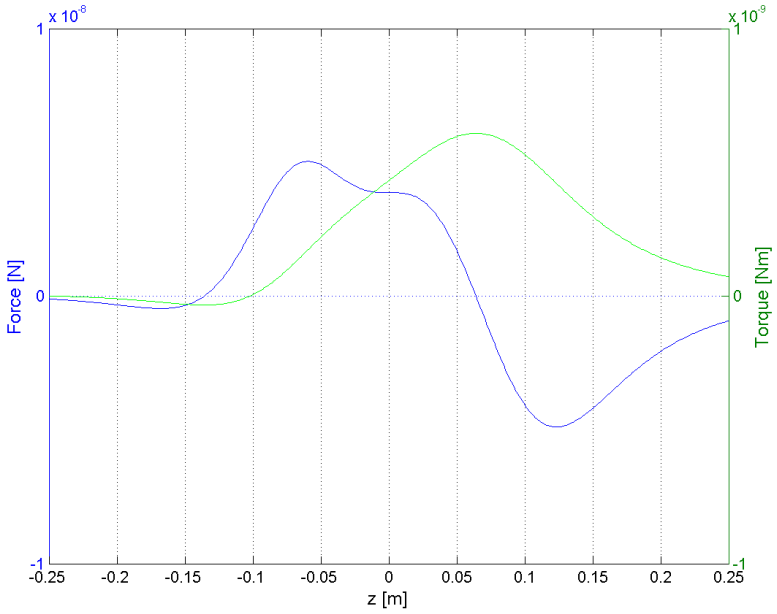

Figure 29: Force and torque on robot in the superimposed magnetic field

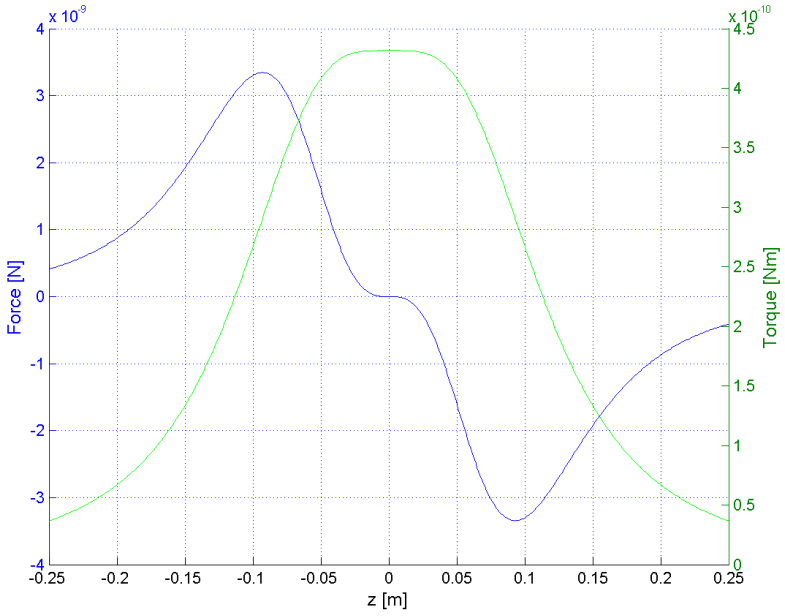

Figure 30: Force and torque on robot in the superimposed magnetic field when the Maxwell coils are deactivated

9.1.4 Conclusions

The idea of using a Helmholtz coil pair for creating a homogeneous field and using a Maxwell coil pair for creating a gradient field is the easiest way to control the alignment axis and the propulsion force independently. It is important to note that the homogeneity of the field generated by the Helmholtz coil pair is only given in a small area around the midpoint of the coil pair. Also the gradient of the field generated by the Maxwell coil pair is only homogeneous in a small area around the midpoint of the Maxwell coil pair. In the optimal case, the field is homogeneous for the whole workspace. In the case of having the system built for applications in the eye, this might be reached by having coils with a large diameter. If one is interested in using such a device for other medical applications than eye surgeries (i.e. investigation of blood vessels), a translational compensation of the actual position of the microrobot to the center of the two coil pairs by moving the test object must be taken into consideration. Such a translational compensation could either be done by centering the microrobot mechanically or by moving the electromagnetical fields by changing the currents in the two coils of one coil pair independently so that the point of the homogeneous field strength is shifted to one or the other side of the coil axis midpoint. This shifting of the field would make controlling of the coils much more complicated and would imply that the current in the coils can be increased compared to the current used for the "standard configuration".
Another aspect that influences the coils design is the nonlinear relation between the radius of the coils and the magnetic field strength. Therefore, as soon as large coils are needed, the necessary total current capacity of the coil increases heavily. In consideration of that fact, maybe some homogeneity of the field has to be given in for the benefit of having a stronger field with the same coil diameter. Figure 31 shows the B-field along the center axis of a "Helmholtz" coil pair, when the distance d between the two coils differs from the optimal Helmholtz configuration where the distance between the coils is chosen to be the same as the radius a of the coils. Plotted are distances chosen to be 0.7 ... 1.3 times the radius.

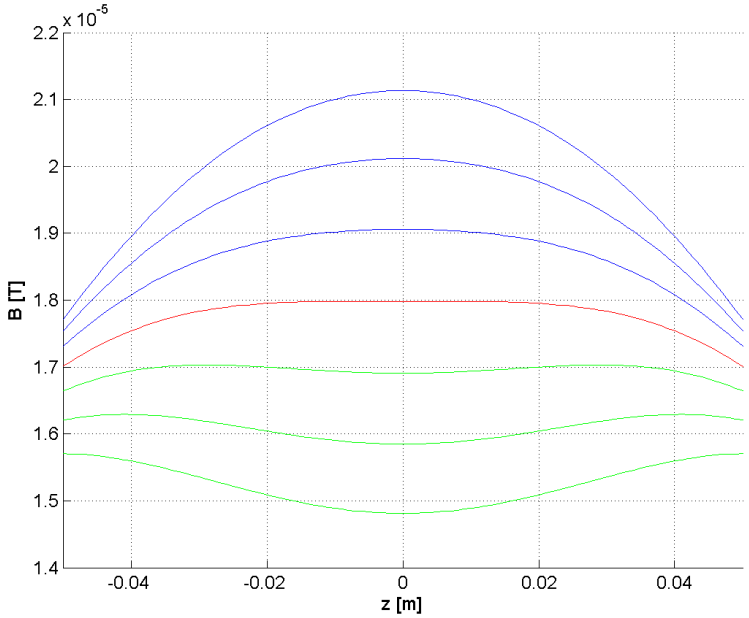

Figure 31: Variance of the Helmholtz field (I=2 A, a=0.1 m). Blue: d<a, red: d=a, green: d>a

Figure 32 shows the gradient of the B-field along the axis of a "Maxwell" coil pair, when the distance between the two coils differs from the optimal Maxwell configuration where the distance between the coils is chosen to be the same as $\sqrt{3}$ times the radius a of the coils. Plotted are distances chosen to be 0.7 ... 1.9 times the radius.

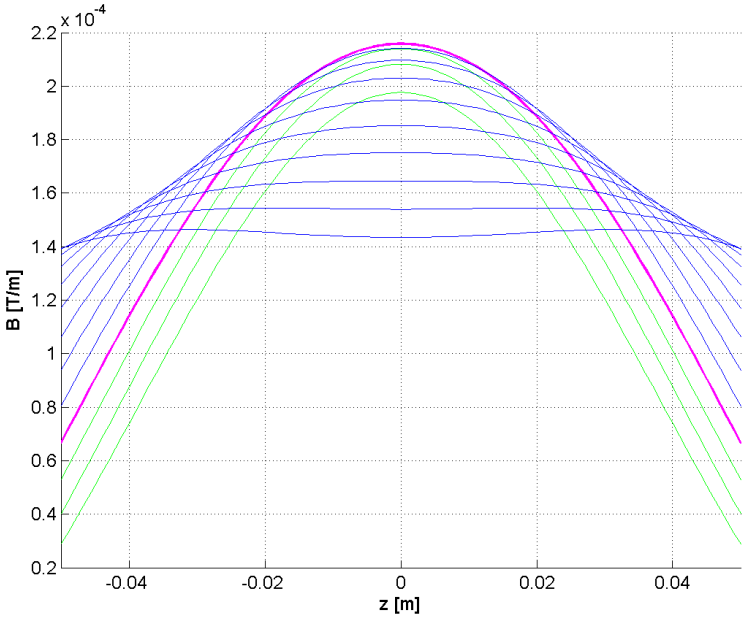

Figure 32: Variance of the gradient of the Maxwell field (I=2 A, a=0.1 m). Blue: d<a, magenta: d=a, green: d>a, red: d=$\sqrt{3}$a

The field generated by coils with a cylindrical section area are used for many applications. In this coil design, the strongest part of the field is aligned in direction of the coil axis. When a longitudinal object should be placed in an external field that should align with the longer object axis, there is no disadvantage in using this common coil design. On the other hand if a field perpendicular to the longer axis of the coil is needed, the diameter of the coil has to be large enough, that the object can be placed inside the coil. There are some other coil designs, that allow a more space-sparing design of the system.

9.1.5 Transverse Gradient Coils

Beyond the common air core coils in a Maxwell configuration, there are the so called "Transverse Gradient Coils" used to generate gradient fields. One method of designing transverse gradient coils is to use four straight, parallel conductors. These conductors are placed at the edge points of a rectangle and are all carrying the same current in the same direction. From this basic principle, different geometrical arrangements are deduced.
In most MRI[10] scanners, the gradient coils are made of wires wound on a cylindrical surface. There, the classical example is the double-saddle or "Golay" coil (Figure 33).

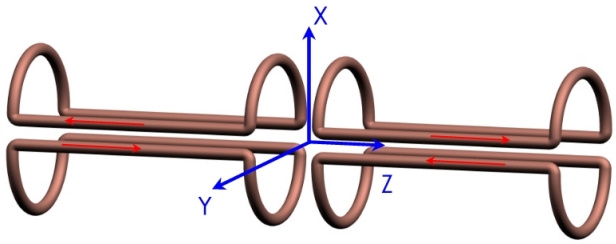

Figure 33: "Golay" x-gradient coil

To generate strong gradient fields, coils must carry large currents. When the fields need to be switched in direction, the currents in the coil must also be switched which leads to oscillating Lorentz forces. The result of these oscillating forces are vibrations of the coil that produce acoustic noise. Using coils with co-axial return paths can - in the correct geometrical configuration - reduce this acoustic noise due to local force balancing [1].

[10]Magnetic Resonance Imaging

Figure 34 shows the B-field of a transverse gradient coil with coaxial return paths. Depending on the choice of the currents direction, a gradient or homogeneous field can be generated between the coils.

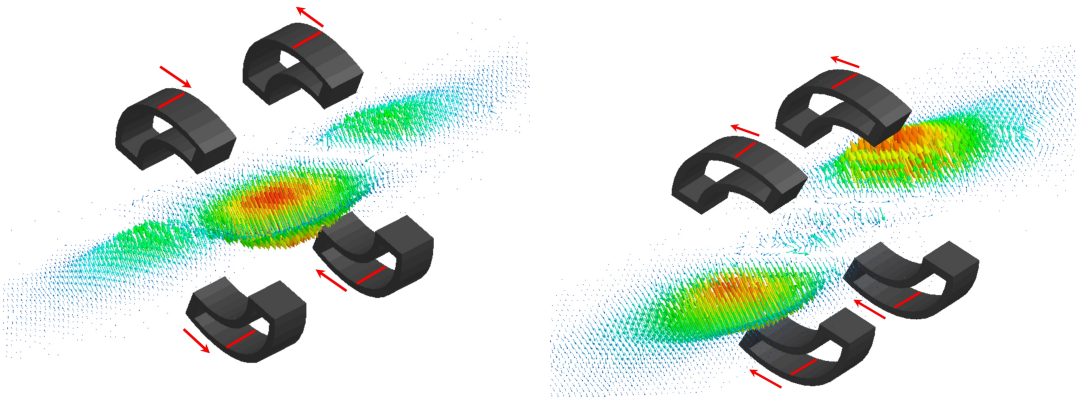

(a) Homogeneous field (b) Gradient field

Figure 34: Magnetic field of transverse gradient coils with co-axial return paths

The advantage of these coils is the noise reduction due to the optimum configuration. Another advantage is the shape of the coils and their arrangement in space. The conductors can be winded on a cylindrical face that can be aligned with the length axis of the human body. Compared with a conventional air core coil, the field is not aligned with the coil axis. Therefore, a combination of conventional air core coils and the transverse gradient coils should be taken into consideration. Regarding the field strength, there is the same disadvantage for this kind of coil as for the common air core coil. The field is generated without iron cores and has therefore a limited field strength.

9.1.6 Birdcage Coils

The so called "Birdcage Coils" are often used as RF[11] coils in MRI systems. Figure 35 shows an illustration of such a coil.

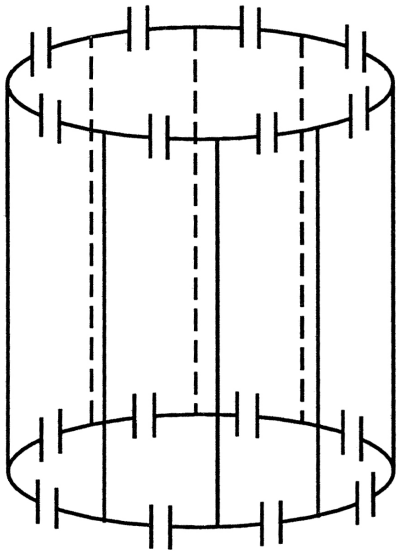

Figure 35: RF-Birdcage coil

Although RF are not planned to be used to steer the microrobot, the conceptual design of the birdcage coil may be adapted to be used in a steering system to generate homogeneous or gradient fields.
Nevertheless, the fields generated by birdcage coils will also be as weak as the fields generated by solenoid or transverse gradient coils.

[11] Radiofrequency

9.2 System with Iron Cores

The main problem of steering microbots with electromagnetic fields is to generate strong enough magnetic fields. In the previous section, system designs with air solenoid coils have been discussed. Using iron cores in coils can increase the magnetic field. The combination of a coil with an iron core is the so called electromagnet. A system using electromagnets for levitating small magnets has been proposed by Nakamura and Khamesee [13].
In this section, an overview of possible designs using iron cores is presented.

9.2.1 Coils with Iron Cores

The first approach will be using common coils with iron cores. Using an iron core in a single coil leads to a higher field near the surface of the iron core compared to the field of the coil without an iron core. On the other hand, if plotting the magnetic field strength along the axis of the coil it can be shown that there is a rapid decrease near the surface of the iron core and that the field further away is nearly the same as the field of the coil without an iron core. Looking at the system configurations described in Section 10 leads to another complication. In these systems always a Helmholtz coil pair and a Maxwell coil pair are aligned on one axis. If "filling" these coils with iron cores, the fields generated by the Helmholtz and Maxwell coils are no longer independent due to mutual magnetization of the iron cores. Furthermore, also the iron cores inside coils aligned on other axes would become magnetized and a very complicated controlling algorithm that includes active demagnetization of unintentional magnetized iron cores will become necessary. Therefore, other magnetic field generation devices and configurations will become necessary.

9.2.2 Push and Pull Magnet

Due to the decreasing field when going away from a magnet, a magnetized specimen is always pulled towards the magnet. If building a system only using one magnet, a solution that enables to push the specimen is discussed in this section. A principle that could be taken into account is the so called "Push and Pull Magnet" system.

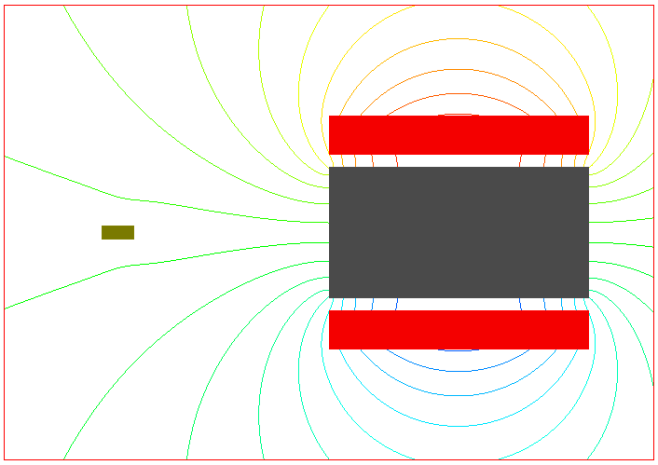

Figure 36: Magnetic field generated by the electromagnet

In this system, one electromagnet is used to push and pull a specimen using the principle of conservation of angular momentum and the high viscosity of the medium, the robot is operating in. For pulling the robot, the electromagnet is generating a constant field. In this field, the robot is aligned with the magnetic field lines and pulled in direction of the magnet.
For pushing the robot, the field cannot just be inverted. Because a specimen in a magnetic field is always aligned to the magnetic field lines, the object would be rotated and again pulled in direction of the magnet. Therefore, if the robot should be moved in the opposite direction, the magnet must generate an oscillating field with an offset. By applying an oscillating field, the robot is pushed for a short time away from the magnet. During this pushing phase, the robot is starting to rotate due to the torque exerted by the magnetic field. Against this magnetic torque, the principle of conservation of angular momentum and the resistance of the fluid around the object are acting. Before the object has rotated more than approximately 45°, the magnetic field changes the direction and the robot is turned back. To get this mechanism to work, the object has to be made of a hard magnetic material. If using a soft magnetic material, the magnetization direction of the object will change when changing the direction of the field generated by the electromagnet and it will not be possible to push the magnet.
This approach for moving the robot towards as well as off the magnet only works, if the rotational acceleration induced by the magnetic moment is smaller than

the acceleration along the axis of the robot. This behavior can be improved by the shape of the object. Therefore, a shape with a large drag resistance against rotation (i.e. using special wings) is preferred.
The advantage of this system is that the magnet could be placed close to the surface of the eye, so that the maximum strength of the field which is found close to the surface of the iron core, can be used.
Calculating approximately the torque and linear drag force for moving the IRIS robot in an eye, this principle would not work due to the small angular moment of the IRIS robot.

9.2.3 Electromagnet Principle

Figure 37 shows the principle of an electromagnet. Inside the gap, a high magnetic field is generated, which is quite homogeneous. The basic principle is that the path of the magnetic field inside the magnet is broken by the gap. If the gap is not too large, the path is closed over the gap ($\Phi_{Fe} = \Phi_g$), having nearly the same strength of the field in the gap as in the material itself.

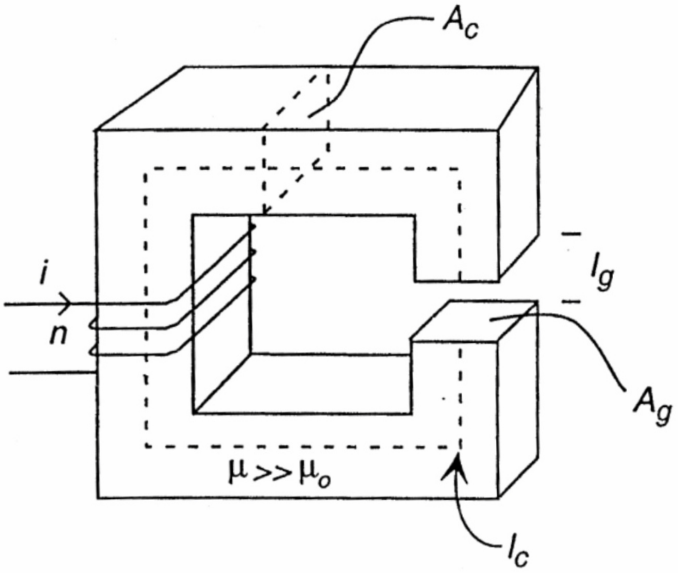

Figure 37: Electromagnet principle [5]

The field inside the gap can be determined to be:

$$\begin{gathered} \oint_c \vec{H} d\vec{l} = NI \\ or \\ H_c l_c + H_g l_g = NI \end{gathered} \tag{9.6}$$

As there is no leakage flux, all the flux that passes through the iron core is also passing through the air gap. Assuming that the face of the gap has the same sectional area as the iron core and that $\mu_0/\mu << 1$, the field in the gap is approximately

$$B_g = \frac{\mu_0 NI}{l_g} \tag{9.7}$$

The same principle can be used with other shapes that build a well defined circuit, i.e. a toroid (Figure 38).

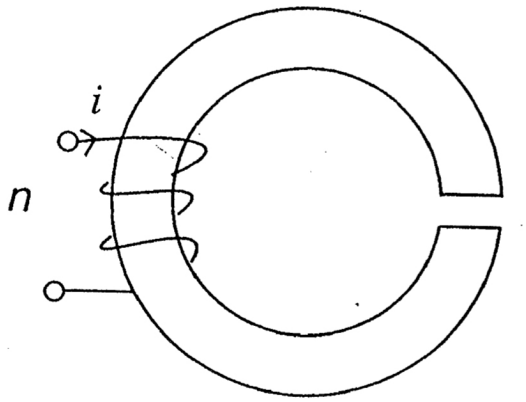

Figure 38: Toroid [5]

Compared with an iron core coil, the field can be pulled high over a wider distance due to the closed loop behavior of the magnetic flux. Due to this fact, the electromagnet principle should be taken into account for building a microrobot steering system.

9.2.4 Gradient Field with Electromagnet

As mentioned in the previous section, the shape of the iron core can also be the shape of a toroid. A possible design of a toroid electromagnet has been simulated in a FEM[12] program[13]. In this design, the "gap faces" are formed in a way, that a gradient field is generated. Having just homogeneous fields would not allow to propel the robot. Figure 39 shows a vector plot of the field inside the gap.

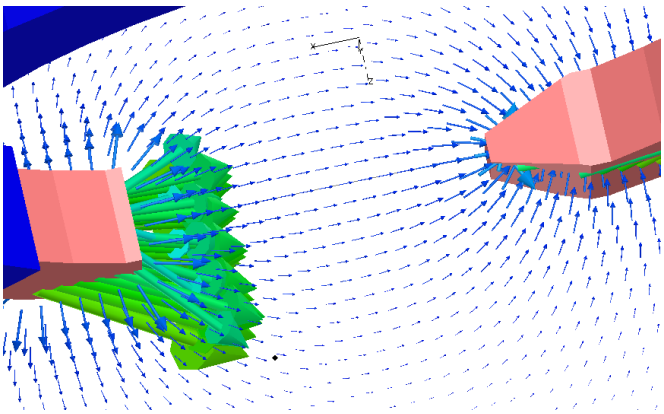

Figure 39: Electromagnet gradient field

Such a configuration could be used in a system with a movable toroid magnet that can be rotated around the head. Because the direction of the field cannot be aligned with the human body axis, an non-holonomic control algorithm will be inevitable.

9.2.5 Conclusions

Finding an accurate system using iron cores is very difficult. The field strength won by the influence of the relative permeability of the cores material can only be used near the surface of the core. Going further away from the surface, the field strength decreases rapidly.
Reaching stronger fields by using cores inside coils is also expensively bought by loosing the decoupling between the homogeneous field and the gradient field. In a system with coils having an iron core, it is not possible to arrange Helmholtz

[12]Finite Element Method
[13]Ansonft Maxwell 3D

and Maxwell coils on the same axis, because it is not possible to have no iron core magnetized in negative axis direction and the other iron core in positive axis direction. Also iron cores not being on the same axis will influence each another and will make controlling of the required fields very difficult.
Another point of view is the accessibility of the system and especially the test-object chamber. In a set-up with coils having iron inlays, the possibility of holding objects or additional equipment through the center of the coil does no longer exist.

Using systems based on an electromagnet will also fail due to the large distance needed between the two poles. For a system like the toroid set-up, a gap of approximately 35 cm would be needed to place the ring around the head. When the gap in the closed flux loop is getting to large, the field strength in the gap is breaking down rapidly and the won effect of having a strong field in the gap is lost.

Due to this considerations, it does not make sense to use coils with iron cores in a microrobot steering system.

9.3 Permanent Magnet Systems

Instead of using air core coils or coils with iron cores, the possibility of using permanent magnets should be taken into account. First, it seems that systems based on permanent magnets will be branded by the same problems that occur with systems based on iron core coils. In Section 9.2.5 it has been stated, that the additional field strength gained by an iron core inlay of a coil is fast decreasing when going away from the iron inlay and due to the disadvantages of the inlays, it does not make sense to use such systems. Furthermore, it has been said that it is not possible to have iron core coils aligned on one axis with different magnetization directions. Having permanent magnets, these problem is reduced due to their hard magnetic material behavior and their well defined magnetization direction. Permanent magnets can be aligned on one axis in a combined Maxwell and Helmholtz configuration without collecting a resulting magnetization of the magnets, as it would be the case for the iron cores of coils. Permanent magnets have a completely different behavior than coils with iron cores and are therefore discussed in this section.

Permanent magnets have several advantages over conventional electromagnets. They can provide a relatively strong magnetic field over an extended spatial region. The magnetization of permanent magnets is basically constant. Another advantage is the shape of the magnets. Permanent magnets can be fabricated with a wide range of different shapes and magnetization patterns. Depending on the used material, they are also relatively inexpensive. On the other hand, the magnetic field of a permanent magnet cannot be adjusted or turned off. That necessitates a completely different mechanical set-up than for conventional air core coils.
Because permanent magnets cannot be switched on and off, tilting the field has to be done by moving the magnets. The design problems are therefore shifted from electrotechnical problems to mechanical problems. To be able to have a fast system, the magnets have to be moved at high speeds with high accelerations. On the other hand, fast actuators are available and often used in automatic fabrication processes. Because it is easier to have fast rotational movements, a system that is tilting fields by having rotational beard magnets should be considered.

9.3.1 Magnet Configurations

The principle of a permanent magnet arrangement is shown in Figure 41. When the two magnets are aligned with their magnetization axis, a homogeneous field can be generated between the two magnets. When rotating one magnet about 90° in positive direction and the other one about 90° in negative direction, the magnetic field at the center between the two magnets is zero.

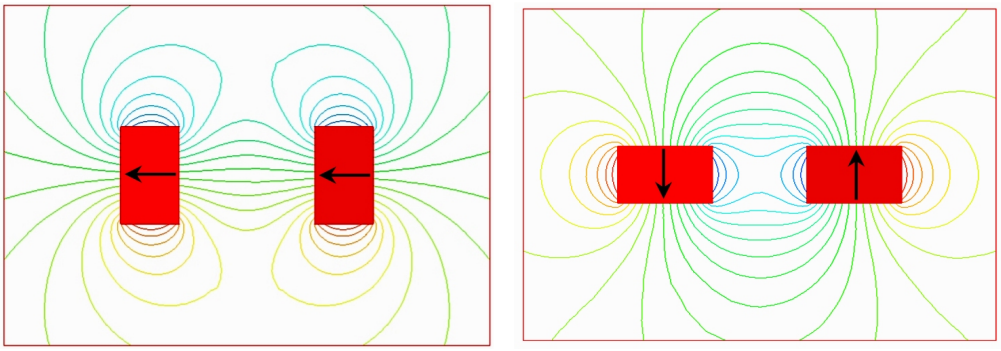

(a) (b)

Figure 40: B-field around permanent magnets in activated position (a) and deactivated position (b). The arrow indicate the direction of the magnetization.

Expanding this principle with more than two magnets, a rotating field can be generated by using four magnets (Figure 41).

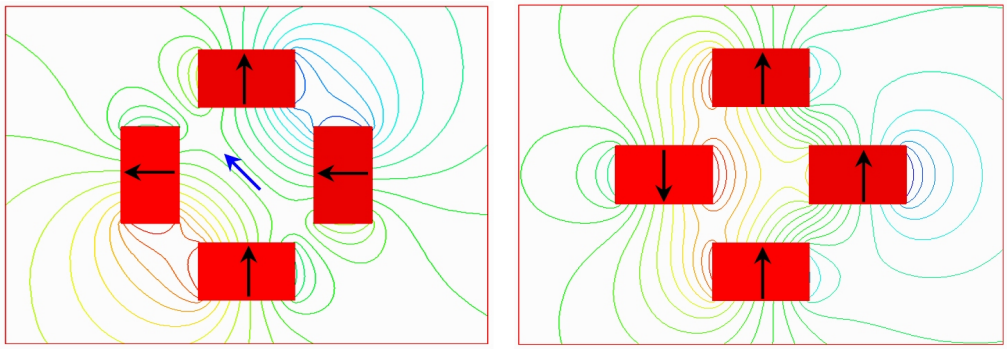

(a) (b)

Figure 41: B-field around permanent magnet. The black arrows indicate the direction of the magnetization and the blue arrow the B-vector just at the center.

In Figure 41(a) it can also be seen, that the field on the diagonal axis is homogeneous over a long distance. This can be explained by the magnetic field generated by a permanent magnet. Figure 42 shows the z-component of the magnetic field of a bar magnet.

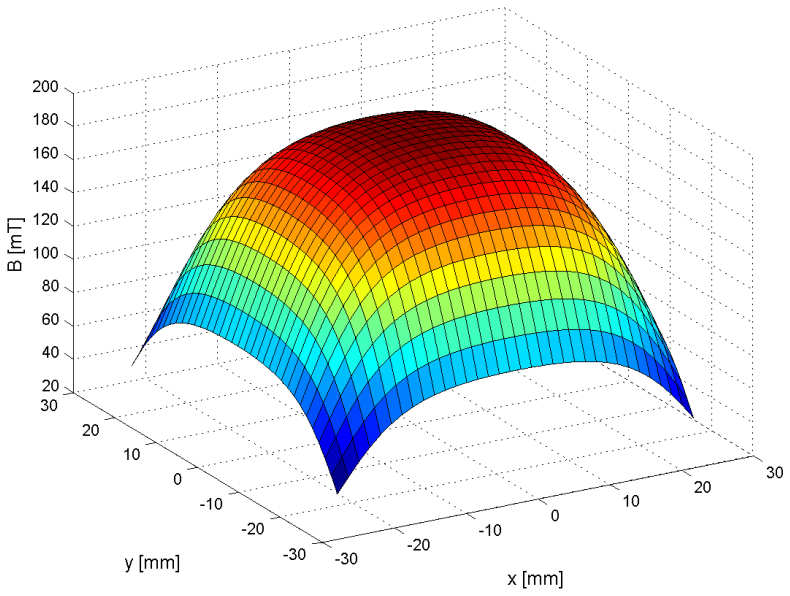

Figure 42: B_z above square bar magnet with edge length 5 cm and height 2 cm at z=1 cm

Depending on the distance from the surface of the magnet and the relation between the edge length and the thickness of the bar magnet, the magnetic field is quite homogeneous in a smaller or larger region over the magnet.
A steering system based on permanent magnets could be an alternative. Having strong permanent magnets leads to strong fields. On the other hand, the field strength of the magnet cannot be changed. Therefore, adjusting the field strength at a certain point needs new solution approaches. Superimposing the field of four permanent magnets for generating the field in one direction could be a possible solution (Figure 43).

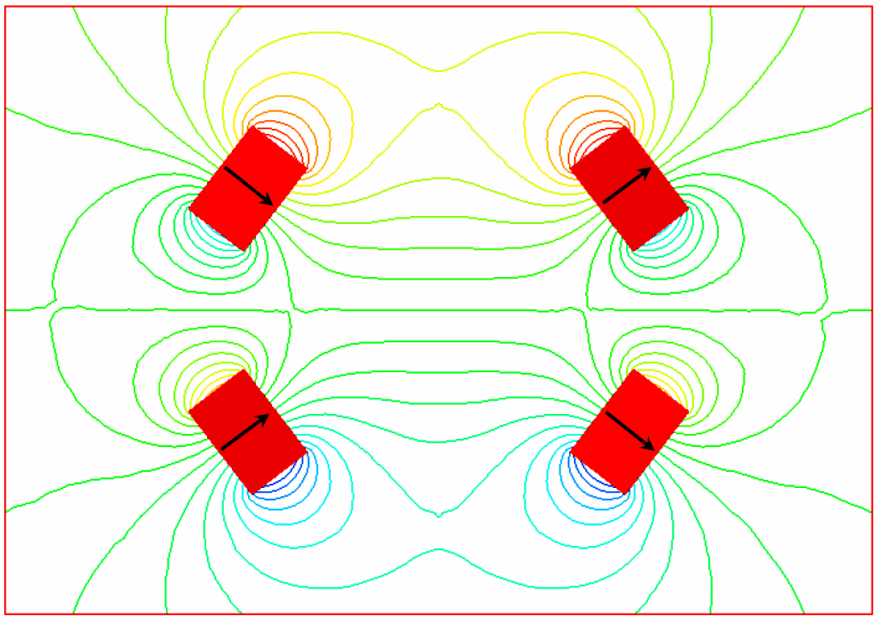

Figure 43: Flux lines of four permanent magnets

By rotating the upper left and lower right magnet about a positive angle and the two other magnets about a negative angle about the magnet midpoint, the field generated along the horizontal direction can be adjusted. Figure 44 shows the field for three different configurations. The axis going through the two left side magnets is chosen to be at the left side of the plot and the axis going through the two right magnets at the right side of the plot.

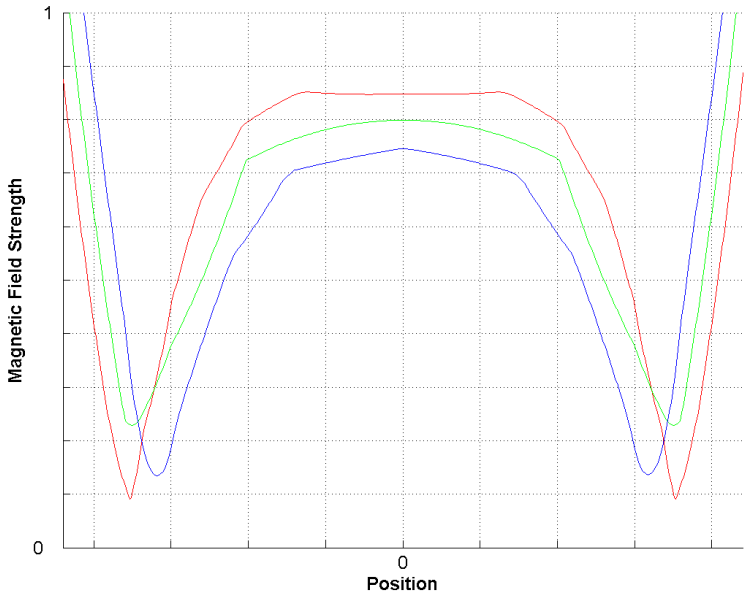

Figure 44: Qualitative development of the magnetic field in an homogeneous field configuration. Blue = magnets rotated about 30°, green = magnets rotated about 37.5°, red = magnets rotated about 45°.

The same field adjustment can be done by generating a field using a configuration where the magnetization of the two magnets on the right side is opposite to the direction of the two magnets on the left side (similar to a Maxwell coil configuration) .

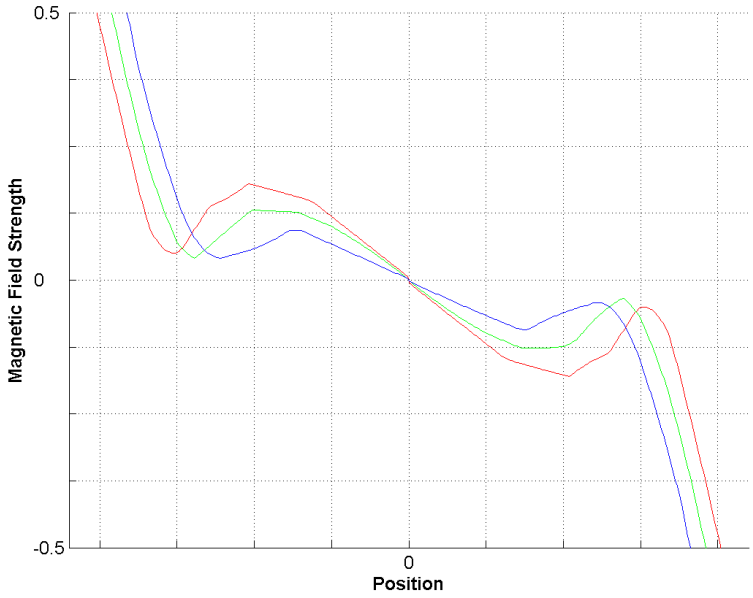

(a) Magnetic field

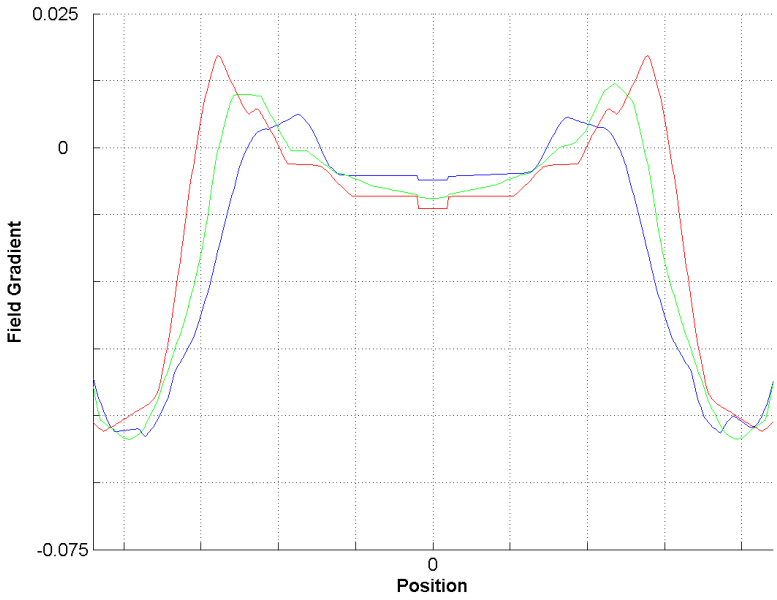

(b) Gradient of magnetic field

Figure 45: Qualitative development of gradient field configuration. Blue = magnets rotated about 30°, green = magnets rotated about 37.5°, red = magnets rotated about 45°.

9.3.2 Conclusions

Permanent magnets can provide relatively strong fields, but special configurations are needed to control these fields because they cannot be just "switched on or off" like electromagnets. As explained before, solutions for solving this problem exist. Such configurations must be carefully modeled and simulated, especially when these configurations are put together to a complete microrobot steering system. When working with robots that are not magnetized by nature, a homogeneous and a gradient field is needed at the same time. The homogeneous field is used to magnetize the robot and the gradient field to propel it. Therefore, a permanent magnet configuration similar to the Helmholtz and Maxwell field respectively is needed (Section 9.1). In this case it has to be kept in mind that permanent magnets can also be demagnetized. Therefore, the magnets material and their strength must be carefully chosen. If the field of one magnet or magnet pair is higher than the minimal coercivity field strength needed to demagnetize a magnet that is having an opposite magnetization than the applied field (second quadrant in B-H curve, Figure 9).

Another difficulty could be the placement of the robot. The configurations for switching the magnetic field on and off as well as the field adjusting configuration is only referred to a certain region. Therefore, it has to be well considered, how a microrobot can be brought in this area without being pulled to one of the field generating magnets. If the magnetic forces are not to high, could be done by hand and/or special grippers, otherwise active shielding of the fields will be inevitable.

Concluding, it can be said that if high fields for low costs should be provided, permanent magnets are a promising principle.

9.4 Summary Magnetic Field Generation Devices

Magnetic field generation devices based on air core coils, iron core coils, electromagnets and permanent magnets have been discussed. The most important conclusions are:

- Air core coils have the advantage of creating independent magnetic fields that can easily be superimposed. Furthermore, the field strength can be well controlled by applying different currents. On the other hand, the fields generated by air core coils are quite weak compared with fields generated i.e. by electromagnets. Anyhow, to generate strong fields with air core coils, superconducting coils that need a lot of additional equipment are necessary. Using such coils for a laboratory prototype is meaningless.

- The logic conclusion would be to use coils with iron cores. Coils with iron cores can generate strong magnetic fields close to the surface of the iron core, but when going further away from the surface, the field strength is rapidly decreasing. Another disadvantage is the mutual magnetization of the iron cores when having multiple coils with iron cores. Due to the nearly unlimited circumference of the magnetic field generated by a coil, also the iron cores of coils that are actually not activated will be magnetized and generate unintentional fields in different directions. Therefore it is also nearly impossible to generate a gradient field by taking two coils with iron cores in the so called Maxwell configuration. Due to this considerations, a system based on coils with iron cores should not primarily be taken into consideration.

- A special way of systems with iron cores are the so called electro magnets. In this system, the fact that the magnetic flux inside a material is closed over a small gap is used. As already mentioned in the discussion of these systems, this effect brings only good benefits for small gaps. Also generating gradient fields is not as easy as when arranging two coils in a so called Maxwell configuration.

- The last discussed group of magnetic field generation devices are the permanent magnets. Although permanent magnets cannot be switched on and off and although the field strength of a single magnet cannot be adjusted,

they have some advantages that should not be neglected. The fields generated by permanent magnets are relatively strong and due to their hard magnetic material behavior it is also possible to arrange multiple magnets nearby without changing their original magnetization and magnetic field direction.

Due to this considerations, either a system based on air core coils or on a novel permanent magnet system should be taken into consideration.

10 Coil Configurations

Using air core coils leads to different possible configurations and arrangements of the coils to fulfill the requirements of a steering system for biomicrorobots. The systems can be sorted by the number of coil pairs used for steering the robot in the 3D space. All system configurations presented in this section are based on the combination of a Helmholtz and a Maxwell coil pair.

10.1 1-Coil Pair

10.1.1 Gimbal System

Having one dynamic coil pair with two rotating degrees of freedom could meet the requirement of generating a magnetic field for nearly all directions in the 3D space. A prototype for such a system has already been developed [12].

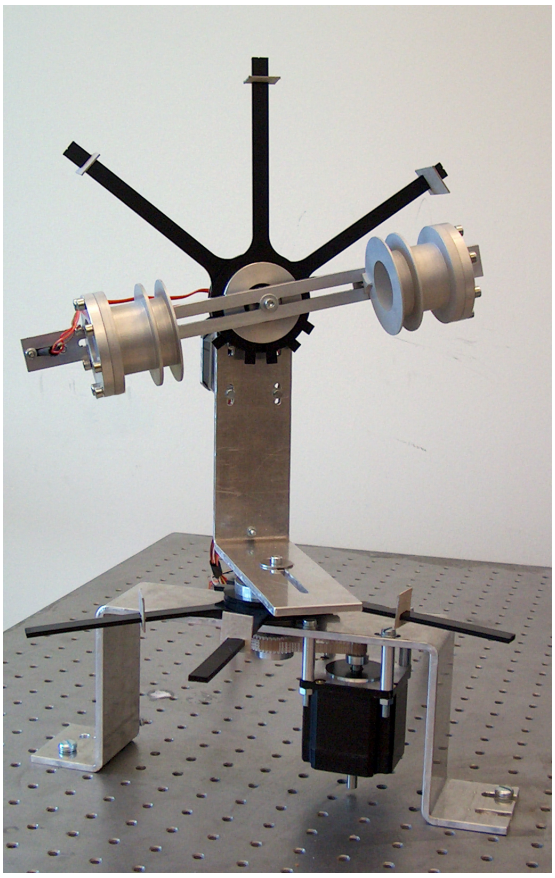

Figure 46: The Gimbal

In this system, one Helmholtz and one Maxwell coil pair are mounted on the same coil centerline. This main coil axis can be rotated about two perpendicular axis.
The problem of this system is the workspace. It is impossible to rotate the coils around both axis about 360° because the rotation is limited by the object holder. As a consequence of that, the microrobot cannot be moved in some directions. Another limiting factor is the reachable rotational accelerations. When scaling this setup for uses in medical applications for human beings, the coils are getting bigger and heavier. Therefore, the moment of inertia of the rotational part is exponentially increasing.

Advantages:

- In this system, only one coil pair is needed and therefore, the costs for manufacturing are not as high as for systems with more than one coil pair.
- Only linear increasing of the dimensions of the system due to an second or third coil pair.
- Only two power amplifiers are needed. One for the Helmholtz coil pair and one for the Maxwell coil pair.
- Controlling of the system is relative easy. The direction and magnitude of the magnetic fields are well defined.
- No mutual inductance of coils from other axis.

Disadvantages:

- The system does not fulfill the requirement for motion along all directions because the object holder inhibits a rotation of 360°. The remaining motion and alignment axis cannot directly be reached. A non-holonomic steering algorithm is inevitable.
- The distance between the coils is defined by the largest dimension of the object. When scaling this system to human size, a large distance between the two coils is needed and therefore the coils are getting huge.

- For visual tracking, more than 2 cameras are needed. There is no position for the cameras where the line of sight is not covered by any moving parts while the system is in operation.

- The rotational acceleration is limited by the stiffness of the coil holder. When having large coils, the moments of inertia and loads on the bearing points are getting very large.

10.1.2 RoboCoil

Another possible configuration using only one coil pair, is the so called "RoboCoil" system. In this system, one coil pair is beard with one rotational degree of freedom relative to the main system holder unit. The second degree of freedom is the motion of the main system holder unit on a circular path around the test object. Not to loose this second degree of freedom because the test object box is attached to the main system holder unit, the test object box itself is also rotational beard (Figure 47).

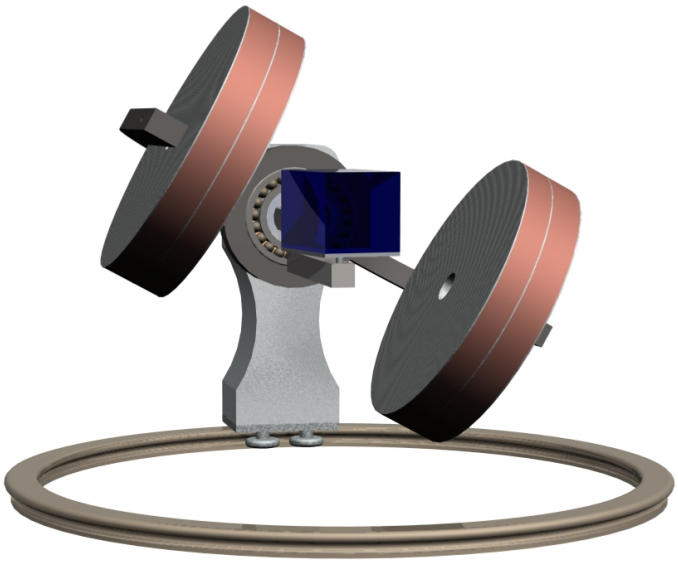

Figure 47: RoboCoil system

To get a static position of the object in a room fixed coordination system, the object itself is rotational beard on the same rotation axis as the rotation axis of the holder unit, holding the coils. The object is always rotating around the object rotation axis at the negative rotation speed that the holder unit is rotating around the holder unit axis (note that the object and holder unit axis must be collinear).

Advantages:

- The robot can be moved along all directions.
- In this system, only one coil pair is needed and therefore, the costs for manufacturing are not as high as for systems with more than one coil pair.
- Only two power amplifiers are needed. One for the Helmholtz coil pair and one for the Maxwell coil pair.
- The cameras for vision can be mounted on the same axis as the object holder. Therefore, vision can be done by only using two cameras in an unidirectional alignment (Section 12.1.1).
- No mutual inductance of coils from other axis.

Disadvantages:

- The distance between the coils is defined by the largest dimension of the object. When scaling this system to human size, a large distance between the two coils is needed and therefore the coils are getting huge. Note that also the revolute joint for the rotation compensation of the object chamber must be placed between the coils.
- If mounting the camera on the object holder, the cameras have a relative speed against the object chamber. That leads to new problems as lighting, edges of the object chamber, etc. making the tracking algorithm more complicated
- If the cameras are not mounted on the object holder, more than two cameras are needed for visual tracking.

- The system needs at least 3 revolute joints. If an additional compensation mechanism for moving the object relative to the coils axis is needed, additional mechanical effort cannot be avoided. This compensation mechanics must be placed after the rotation compensation of the object chamber. This will additionally enlarge the distance between the coils

- Controlling and steering of the system is more complex than in the Gimbal system.

- Changing the direction of the microrobot is dependent on the rotational acceleration of the system. Having large and huge coils, very strong actuators are needed.

- The mechanical design effort is - compared with other coil configurations - more complex.

10.2 2-Coil Pairs

10.2.1 1-Dynamic and 1-Static Coil Pair

Using 2 coil pairs reduces the degrees of movability for the system. By using one static and one dynamic coil pair, all vector directions of the magnetic field can be reached by only rotating one coil pair around one axis. Such a system is shown in Figure 48. In this system, the object holder is placed through the static coil pair, that is also the most important advantage of this type of system. Having a system with one rotating coil pair, the longest dimension of the test-object defines the distance between the coils. In this system, the longest dimension of the object (in the case of a human, the height) can be placed trough the coils and so the second length defines the distance between the coils.

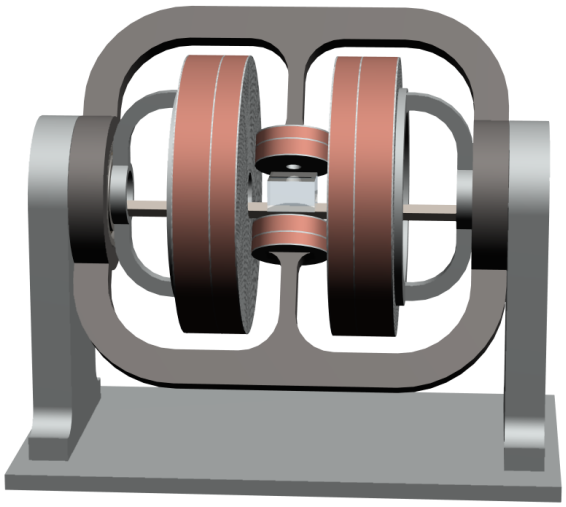

Figure 48: System with one rotating and one static coil pair

Advantages:

- Motions along all axis without limitations are possible.
- The distance between the coils is defined by the second largest dimension of the test object. Long shaped objects can be placed through the coils.

- Two cameras for vision are enough, if they are placed on the static coils axis with a mirror system (Section 12.1.1).

Disadvantages:

- More than one coil pair is needed and therefore at least four power amplifiers are necessary.
- If a "real" Helmholtz and Maxwell configuration should be reached, the radius of the coils for the second coil pair have to be has to be chosen to be approximately diameter of the coils of the first coil pair (Figure 49).
- Changing the direction of the microrobot is dependent on the rotational acceleration of the system. Having large and huge coils, very strong actuators are needed.

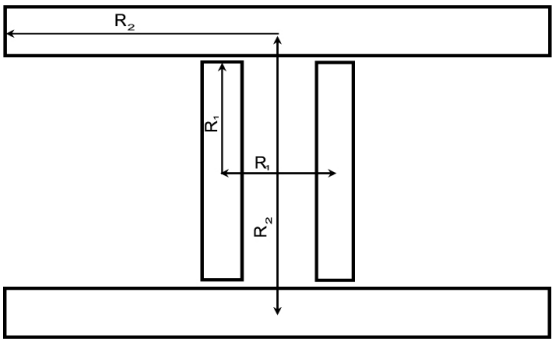

Figure 49: First and second Helmholtz coil pair in an optimal distance arrangement

10.3 3-Coil Pairs

10.3.1 Optimum Field Solution

In this system configuration, three Helmholtz and Maxwell coil pairs are arranged on three perpendicular axis. The distance between the coils is chosen to be a Helmholtz resp. Maxwell configuration as described in Section 9.1.1 and Section 9.1.2. The homogeneous field as well as the gradient field is generated by superimposing the fields generated by the coil pairs on the three axis. First simulations of the superimposed field in different directions have been made with the

Ansonft Maxwell 3D FEM software. Figure 50 shows a vector plot of a simulated superimposed field.

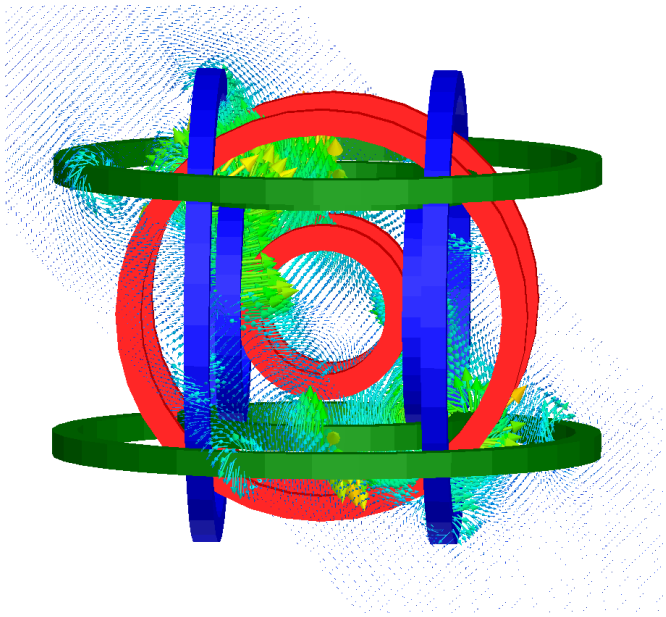

Figure 50: FEM simulation of the superimposed B-field

Advantages:

- Optimum homogeneous fields generated by the coils.
- No mechanical rotating parts. Therefore, the design of the system is easier. Rotating parts will make the cabling of the electrical parts and the design of the flexible tubes for the cooling system more complicated.
- If coils with a small inductance are used, the direction of the resulting field can be changed very fast.
- Inaccuracies in the mechanical set-up can easily be corrected by the software controlling the fields.
- Due to not having any rotating parts, the positions for the tracking devices are well defined.
- The dimensions of the coils are given by the second largest dimension of the test object. Long shaped objects can be placed through the coils.

Disadvantages:

- The main problem of this system would be the dimensions of the coils. As discussed in Sections 9.1.1 and 9.1.2, the optimum distance between the coils is given by choosing the radius of the coils as the distance between the Helmholtz coils and by choosing $\sqrt{3}$ times the radius of the coils for the distance between the Maxwell coils. Therefore the coil dimensions are rapidly increasing for the second and third coil pair. As a result of the increasing dimensions of the coils, very high currents are needed to generate strong enough magnetic fields.
- Having more coils in a small area can lead to reciprocal inductiveness.
- All coil pairs are having different dimensions which makes manufacturing more expensive.
- At least six amplifiers are needed. Should all coils independently be controlled, even twelve amplifiers are necessary.

10.3.2 Power Cube

Another solution, using three static coils, is the "Power Cube" (Figure 51). In this system, the coils are fitted in an rectangular cube. The three Helmholtz and Maxwell coil pairs are all having the same dimensions. The cube itself is not only used as a base frame, it is also used as a large cooling block.

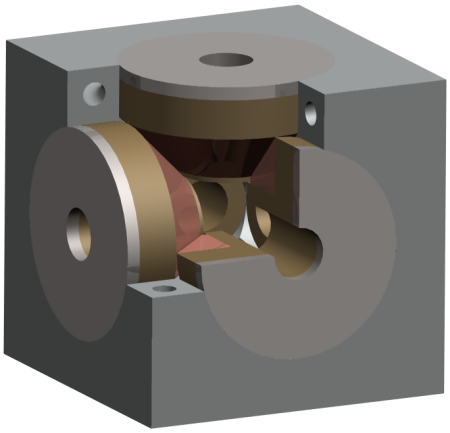

Figure 51: "Power Cube"

Advantages:

- All Maxwell and all Helmholtz coils are having the same dimensions that makes manufacturing less expensive.
- Having no rotating parts makes the cabling of the electrical parts and the design of the flexible tubes easier.
- Due to not having any rotating parts, the positions for the tracking devices are well defined.
- The dimensions of the coils are defined by the second largest dimension of the test object. Long shaped objects can be placed through the coils.

Disadvantages:

- Because all coils are having the same dimensions and are configured in a rectangular array, the distance between the coils is a "non real" Helmholtz and Maxwell configuration. The distance between the coils is much larger than the optimum Helmholtz or Maxwell distance. This leads to less stronger and inhomogeneous fields (Section 9.1.4).
- At least six amplifiers are necessary. Should all coils independently be controlled, even twelve amplifiers are necessary.
- Having more coils in a small area can lead to mutual inductance of the coils.
- To use the space optimal, coils with a 45° angle are necessary. Such coils are a little bit more expensive than "normal" coils due to the more complex manufacturing process.

A configuration for a system that generates a homogeneous field of about 60 mT and a gradient of 1.48 T/m has been calculated to evaluate the B-field progress along the middle axis of coils.

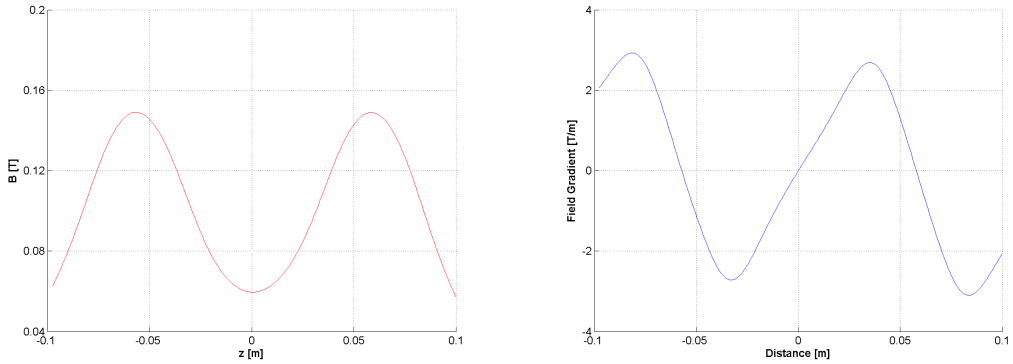

(a) B-field along coils axis (b) Gradient of B-field along coils axis

Figure 52: Power Cube - Helmholtz field

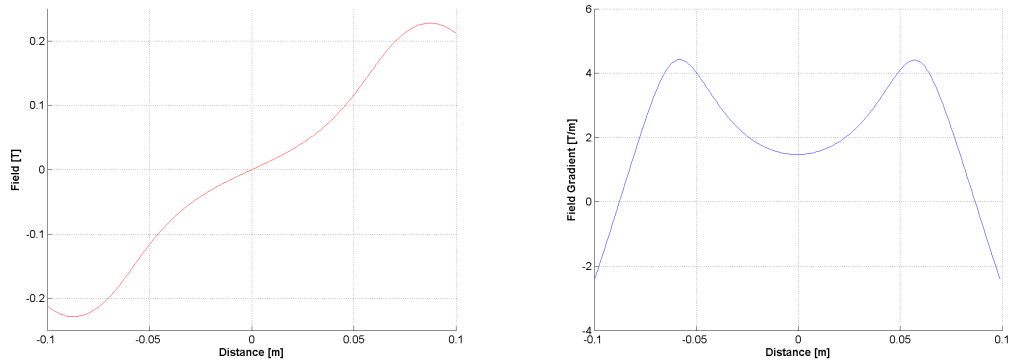

(a) B-field along coils axis (b) Gradient of B-field along coils axis

Figure 53: Power Cube - B-field

It can be seen that the field at the middle point of a coil axis is weaker than closer to the coils. This is valid as well as for the homogeneous field as for the gradient field. By making an intelligent shift of the fields, the field actually used for generating the magnetization of the robot can also be used to build an additional component for the gradient. Such a "shift" of the fields can be produced by controlling the two coils generating the homogeneous field independently. To win gradient field strength by shifting the "homogeneous" Helmholtz field implies that the current carried by the Helmholtz coils can be increased. Otherwise there will not be enough field strength to keep the robots magnetization saturated. On the other hand, from aspects of building the coils as small as possible, it does not make sense to over dimensionize the Helmholtz coils. Therefore, such a field

shift only makes sense for using it as a short time amplification of the gradient field where it can be said, that for a short time, a higher current in the wires is applicable without destroying them. Figure 54 shows such a field shift.

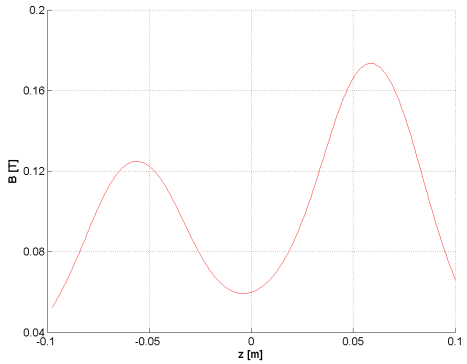

(a) Helmholtz B-field along coils axis

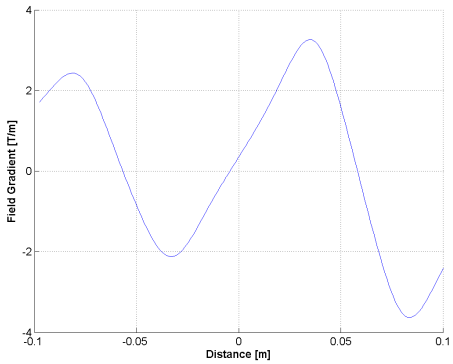

(b) Gradient of Helmholtz B-field along coils axis

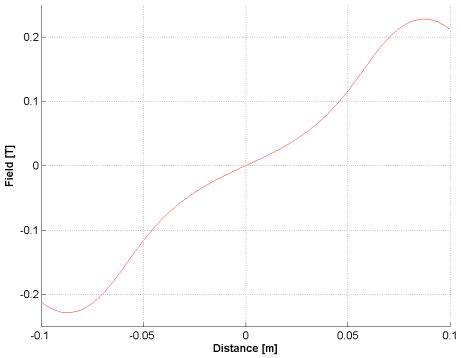

(c) Maxwell B-field along coils axis

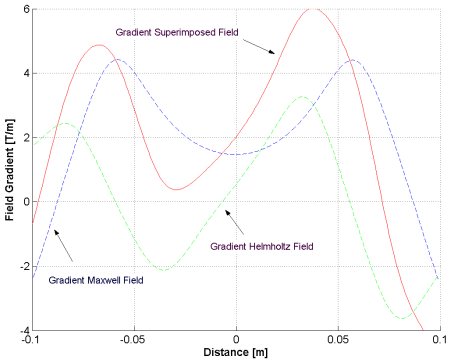

(d) Gradient of B-fields

Figure 54: Power Cube - Shifted B-field

10.4 Summary of the Configurations

In the previous sections, different coil configurations for systems based on air core coils have been discussed. All of these proposals have their individual advantages and disadvantages. The proposals base on the requirement of providing a resulting magnetic field that can be aligned in each direction. So far, no exact designs concerning the dimensions and the design of the coils have been done. Therefore, until now all decisions must basically be taken into consideration. To evaluate

which system would be the optimal solution, it first must be checked if all requirements mentioned in Section 3 are fulfilled. On this account, the following questions must be posed:

- Can the needed field strength be achieved
- Is the field homogeneous enough
- Is the system controllable
- Is the system fast enough
- Can the required power be supplied
- Is the system feasible concerning technical considerations
- Can the system be scaled to human size
- What are the manufacturing costs
- What about the adaptability for different experiments

In Section 7.2 the needed field strength for propelling a robot in different applications has been determined. Calculating some coil designs for the three main groups of possible configurations (1-coil pair, 2-coil pairs and 3-coil pairs) will already exclude some of the proposed systems. When also having a look at the technical feasibility of the systems it becomes apparent that it is nearly impossible to build a meaningful system based on air core coils.
A calculation shows that the needed coil dimensions for a small laboratory prototype will be very large. To generate a homogeneous field of approximately 200 mT in a prototype with a free space of 3.5 cm between the coils will lead to a coil pair with a inner coil diameter of 10 cm and an outer coil diameter of 26 cm when a coil thickness of 4 cm is chosen. Figure 55 shows the field progression of a coil pair with the mentioned coil dimensions, when a current of 2.8 A is applied

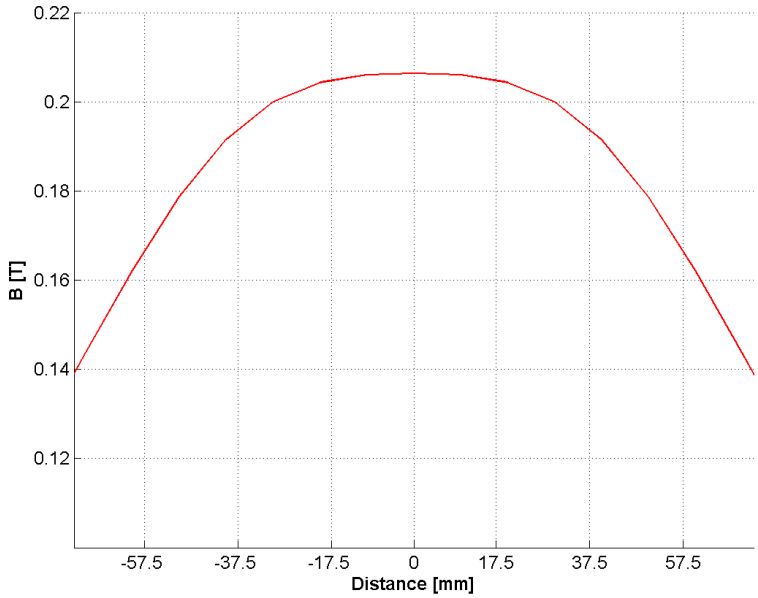

Figure 55: Homogeneous field

In this configuration, there would be approximately 6800 turns with a total resistance of approximately 220 ohm. Therefore, the required power for one coil would be approximately 1725 W.
The wire of such a coil would act as a large internal heat generation and therefore a cooling system would be inevitable. In Section 11.2 different cooling systems and their influence on the coil design are discussed.

Due to this reasons, other configurations based on other field generation devices (i.e. permanent magnets) must be taken into consideration.

11 Coil Engineering

If a system based on coils should be designed, some important points concerning coil design must already in the beginning of the development phase of the design process be taken into account.
Designing coils is a very sophisticated field of engineering. Electrotechnical, thermodynamical and magnetostatical properties have to be taken into account. In this section, only the most important aspects will be mentioned. It is obvious that one could write a book about coil design. The aim of this report is to give an overview of the most important facts that should help to make a drafting for a coil that then can be discussed and improved by an expert in the field of coil design. A coil basically consists of a coil body and a wire that is winded onto the body. In addition there can be certain components for cooling the coil. The requirements for a coil can generally be described as follows:

- Provide the required field strength at a certain distance.
- Low inductance
- Low resistance
- Low operating temperature
- Inexpensive manufacturing
- Small dimensions

All these requirements depend on each other. For example the resistance and the inductance are not only dependent on the field that should be generated by the coil, but they are also dependent on the temperature of the wire and the dimensions of the coil. Starting at a given inner diameter, the coil can either be designed to have a larger outer diameter and a small thickness or to have a smaller outer diameter and a larger thickness. In the case of having a smaller outer diameter, the resistance of the wire will be smaller due to the shorter wire. On the other hand, the field progression outside the coil will be another than the progression of the coil with the larger outer diameter. At the same time, inductance that is limiting the switching time is changing and therefore, the optimal ratio of thickness and diameter of the coil has to be found.

11.1 Coil Inductance

All coils have an inductance that is the principle limit for the switching time. Each coil can be modelled by a coil equivalent circuit with an inductance and a resistance (Figure 56).

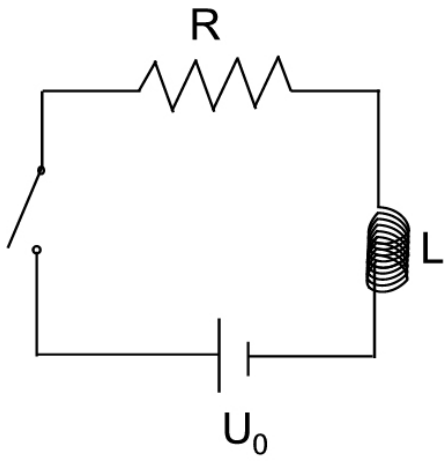

Figure 56: Coil equivalent circuit

The resistance (R) is calculated from the the specific resistance of the material (ρ) multiplied by the length of the wire (L) divided by the cross sectional area of the wire (A):

$$R = \rho \frac{L}{A} \tag{11.1}$$

The inductance of a coil is dependent on the geometry and the material of the coil. The inductance can be calculated over the magnetic flux through the coil:

$$L = \frac{\Phi}{I} \tag{11.2}$$

If there is another current circuit close to this "current circuit", an additional flux term is added

$$\Phi_m = L_{12} I_2 \tag{11.3}$$

where L_{12} is the so called mutual inductance.

Applying Kirchhoff's Voltage Law, the circuit shown in Figure 56 can be described by

$$U_0 - IR - L\frac{dI}{dt} = 0 \tag{11.4}$$

Solving (11.4) for I(t) leads to

$$\begin{aligned} I(t) &= \frac{U_0}{R}(1 - e^{\frac{-Rt}{L}}) \\ &= \frac{U_0}{R}(1 - e^{\frac{-t}{\tau}}) \\ &= I_e(1 - e^{\frac{-t}{\tau}}) \end{aligned} \tag{11.5}$$

where

$$\tau = \frac{L}{R} \tag{11.6}$$

is the time-constant for the coil circuit. Will say the larger the inductance and the smaller the resistance of the coil the longer is the time to reach the desired end current I_e.
This behavior must be taken into account when designing coils.

11.2 Coil Cooling

Beside the electro mechanical problem of the inductance of the coils and the need to provide large power supplies, warming of the coils is another problem that needs to be considered when designing coils. Due to the resistance of the wire material, the wires are warming up during operation. On one side, the increased temperature of the wire causes a higher resistance, on the other side, if the wire becomes too hot, either the isolation of the wire or the wire itself breaks down. In addition, warming of the wires leads to deformations due to the thermal expansion of the material. Therefore, for larger coils, a cooling system is needed. There are different principles for cooling the coils. An important issue is also the prize of a coil. The cheapest coils are just wind without any special additional features like cooling wires. To design a good cooling system for a coil, the winding process has to be improved. When winding a coil, gaps between the single wires cannot be avoided. Within such gaps there is no material that could conduct the heat away from the wire. Therefore, the gaps must be filled with a material with a good heat conductivity to conduct the heat away from the wires to the outer side of the coil. If that is not enough, a flowing medium is needed that transports the heat out of the coil.
In the following sections, first some rough approximations are made to determine the internal heat generation of the wires and to derive an approximate cooling flow if a cooling medium is used. Afterwards two possibilities for cooling the coils are presented. In this section, superconducting coils will not be treated.

11.2.1 Calculations

In the coil system, the wires are treated as an internal heat source. The heat produced by the wires depends on the current, the specific resistance of the wire material and the diameter of the wire. The resistance of the wire can be obtained from

$$R_e = \frac{\rho_e l}{A} \tag{11.7}$$

where ρ_e is the specific resistance of the material, l is the length and A is the section area. The specific heat emission per volume unit is then

$$\dot{Q}'''_{source} = \frac{\dot{Q}_{source}}{Al} = \frac{I^2 \rho_e l}{(Al)A} = i^2 \rho_e \tag{11.8}$$

where i is the current density $i = I/A$.
If a cooling medium is used, the cooling medium should deduce the largest part of the heat generated by the wires. The heat flow of the cooling medium can be determined by

$$Q = \dot{m} c_p (T_1 - T_2) \tag{11.9}$$

where $\dot{m}$ is the mass flow, c_p[14] the specific heat capacity of the medium and $T_1 - T_2$ the temperature change in the medium.
In the steady state condition, the heat production and emission are in equilibrium. In the case of a cooled coil, the wires are treated as a heat generation and the cooling fluid as heat emission. Additionally, we have natural convection on the surfaces of the coil. For a rough approximation, the flow from the wires can be set equal to the heat flow of the cooling fluid to determine the needed mass flow of the cooling medium for a given temperature change in the cooling medium.
This approximation neglects any geometrical and thermal attributes of the coil. If one is interested in more precise results, the thermal conductivity of the used materials, the geometry of the coils and the convection behavior of the surfaces with contact to a flowing medium also has to be modelled. Especially the convection coefficient between the cooling medium and the coil contact surface has to be determined more precise. In this area, there is the temperature gradient.
For a laminar flow in a tube, the heat-transfer coefficient can be determined over the so called Nusselt number Nu_D. For a laminar flow in a tube with a constant surface temperature, the Nusselt number can be approximated to be 3.66 [16]. Having a turbulent flow, an average Nusselt number can to be calculated from

$$\overline{Nu_d} = 0.0235 \cdot (Re_D^{0.8} - 230)(1.8 Pr^{0.3} - 0.8) \left(1 + \left(\frac{D}{L}\right)^{\frac{2}{3}}\right) \left(\frac{\mu}{\mu_w}\right)^{0.14} \tag{11.10}$$

[14] water 20°: $4.182 \cdot 10^3 \frac{J}{kgK}$

The heat transfer coefficient is then defined as

$$\alpha = \frac{Nu_D \lambda}{D} \tag{11.11}$$

where λ is the heat conduction capacity of the flowing medium and D is the diameter of the tube. With this convection coefficient, the material properties, the geometrical dimensions of the coil and the cooling tubes, the heat flow can be calculated. Because of the geometrical properties of the coil, in most cases the flows and temperatures are calculated with FEM programs.

11.2.2 Cooled Body Coil

One possibility to cool the coil is just cooling of the body of the coil. If only the body of the coil is cooled, the body has to be made from materials with a good heat conductivity. Often aluminium is chosen because of its good manufacturing properties. On the other hand, using aluminium leads to eddy currents inside the coil body that interfere with the magnetic field. In Figure 57 a coil body with cooling channels inside the body is shown. The advantage of such a cooling system is the decoupling of the winding process and the cooling system of the coil. Using such a cooling system does not interfere with the winding process. This makes manufacturing of the coils cheaper. The disadvantage on the other hand is that there is no direct contact between the cooling channels and the wires. Furthermore the wires are only cooled from one side of the wire bundle. This leads to very high temperatures in the middle layer of the wire rounds.
To avoid that, the coil body could be equipped with cooling ribs going from the inner side to the outer side of the body. But here, there is a tradeoff between cooling the wire and gaining space for additional wire turns.

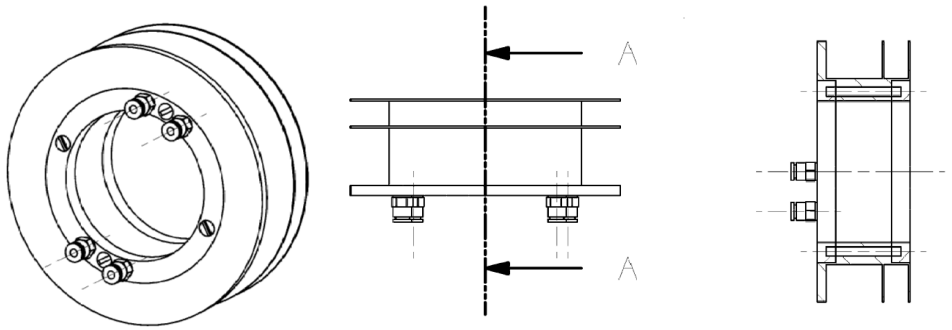

(a) Coil Body (b) Side View (c) Section Cut A-A

Figure 57: Coil with cooling water channels

11.2.3 Winded Cooling Tubes

Another cooling mechanism are cooling tubes that are winded on the coils body between the wire. Figure 58 shows the principle of the winded cooling channels.

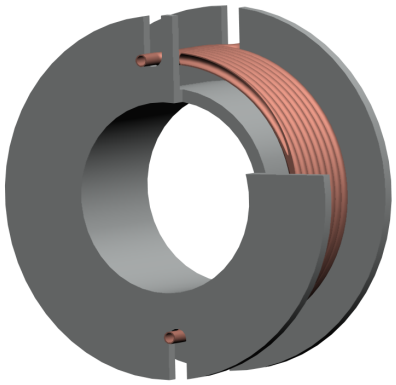

Figure 58: Coil with copper cooling tubes

To reach a good gradient between the temperature of the water in the cooling tubes and the temperature of the wires over the whole thickness of the coils, two helix wire tubes can be winded in one another. In one tube the water is flowing then from the left to the right and in the other tube from the right to the left side. The advantage of such a cooling system is the fact, that the material of the coil body does not need a good thermal conductivity. The material for the coil body can be chosen by considerations about electromagnetical effects.

There are many similar systems for cooling coils, however all off them can be allocated to either one of the two types of systems described above.

11.2.4 System Comparison

To be able to make an estimation which system is appropriate to cool the coils, the two main principles - "cooled coil body" and "winded cooling tubes" - are compared with each other.

Calculation Settings

The given boundary conditions for the coils are.

- Minimum inner radius of the coil body 38 mm
- Thickness of the coil body 50 mm
- Outer radius of the coil 70 mm
- Distance between the coils measured from the coil body's face 50 mm
- Magnetic field at the center between the two coils on the coils axis 0.05 T

These boundary conditions are randomly chosen, but represent given inputs into a microrobot steering system. The inner coil body diameter can be relevant, if something should be placed through the coil (object holder, cameras, ...). The thickness and the outer diameter are influencing the other coils that may be placed around this coil pair. Therefore, these two dimensions are fixed. The distance between the two coils is defined by the usable workspace and has also been set to a fixed value as well as the field strength.
For evaluating the temperature and heat flux inside the coil with the ANSYS Workbench 8.1 FEM program, some assumptions and simplification are done. If more accurate results are wished, some of these simplifications must be substituted by exact determined values.
To generate the required field, the number of turns and the current is calculated numerically with MATLAB. It is assumed, that the whole available space for the wires is used. The internal heat generation by the wires has been determined using (11.7) to calculate the resistance of the wire. The length of the wire has

been determined using the average radius of wire area to get an average length for one winding. This value has then been multiplied by the number of turns calculated in MATLAB. The wires are modeled with a square section shape, so gaps and therefore inhomogeneous thermal conductivity in the wire bundle have been neglected.
Table 10 lists the values for the two coils

Coil Type	**Single Wire Current [A]**	**Number of Turns**	**Average Wire Radius [mm]**	**Total Resistance [ohm]**	**Power [W]**	**Internal Heat Generation** $[W/m^3]$
Cooled Body	2.8	1189	60	27.97	219.3	$6.6 \cdot 10^5$
Winded Cooling Tubes	2.17	2412	55	52	244.9	$8.4 \cdot 10^5$

Table 10: Coil parameters

By having the same distances between the coils but different average coil radii due to different designs of the coils, the magnetic fields generated by the coil pair look different (Figure 59).

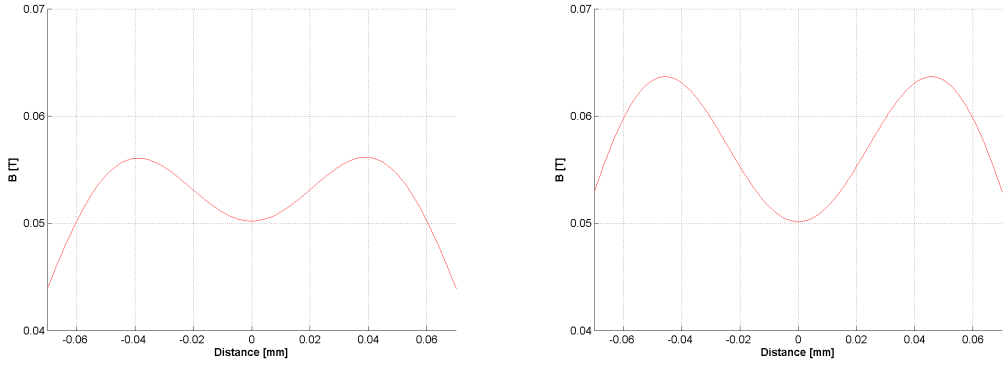

(a) "Cooled Body Coil" (b) "Winded Cooling Tubes"

Figure 59: Magnetic field cooled coils

Beyond the internal heat generation of the wires, some other boundary conditions and assumptions have been made for the FEM calculation:

- Natural convection on the outer surfaces of the coil body and the outer wire surface ($\alpha : 5W/m^2$)
- Ambient temperature for the outer surfaces of the coil body and the outer wire surface (22 °C)
- Since there is no possibility to define a flowing medium in the used FEM program, a convection for laminar flow in tubes has been set for the cooling channels ($\alpha : 437.8W/m^2$). The ambient temperature in the water channels (water temperature) has been set and is assumed to be an average temperature with a constant temperature in the water channels (15 °C).
- For the stopping criteria for the number of iterations a refinement value of 5% is set.
- The coil body material is set to be aluminium, the wires and water channels copper and the water valves brass.

Limitations of the calculation:

- Due to constant water temperature modeled for the calculation, in the area of the inflow and the outflow of the water, the highest differences between the calculation and the real system will appear.
- The flow in the tubes has been assumed to be laminar. Especially for the cooled body coil, this may not match with the real system.
- The windings of the wire have been simplified by assuming a square section shape and that there are no gaps in between the single windings. Therefore, the real temperature inside the wire is most likely higher than the calculated temperature.

11.2.5 Results

For calculating the thermal effects inside the coil multiple boundary conditions and assumptions have been set. The solution has to be treated with respect to these settings. The most important point is the setting for the cooling medium. For the calculations a temperature has been set for the fluid. It is obvious that the temperature will change during its way through the cooling channels. The

change of the temperature is dependent on the mass flow of the cooling fluid. The faster the fluid flows through the channel, the higher is the temperature gradient between the fluid and the border of the water channel at the output of the coil. If the temperature T_c is set for the fluid, a mass flow can be approximated by using the heat flux for the convective term from the FEM calculation. Using (11.9), the mass flow is

$$\dot{m} = \frac{Q}{c_p \delta T} \tag{11.12}$$

The assumption with the highest uncertainty is the assumption for the change of the temperature in the water. To be on the safe side, the incoming cooling water temperature $T_{in,cw}$ has to be lower than T_c. The temperature change δT is then calculated by $T_c - T_{in,cw}$. In this case, in the region of the incoming cooling water, the temperature of the coil will be a little bit lower than the results of the FEM calculation.
Table 11 shows the converged thermal values for the "Cooled Coil Body".

Scope	**Minimum Temperature** [°C]	**Maximum Temperature** [°C]
All Bodies	55.52	59.05
Coil Body	57.11	59.05
Cabs	56.22	58.72
Wire	58.06	59.05

Table 11: Thermal results - "Cooled Coil Body"

Compared with the results for the "Winded Cooling Tubes Coil", the results are much higher.

Scope	**Minimum Temperature** [°C]	**Maximum Temperature** [°C]
All Bodies	34.2	39.06
Coil Body	37.52	39.05
Outer Wire	38.38	39.06
Inner Wire	38.19	38.75

Table 12: Thermal results - "Winded Cooling Tubes Coil"

The results for the temperature dispersion and the parameter settings for the calculations can be found in Appendix F.

11.2.6 Conclusions

Due to the much lower temperature of the coil and its components a cooling mechanism that is similar to the "cooled wire coil" should be preferred. This result is not surprising. The contact surface of the channels for the cooling medium is much smaller in the cooled body coil than in the other coil. Additionally, the temperature gradient between the cooling medium and the contact surface is higher, if the cooling tubes are going directly through the heat generating parts. Nevertheless, the cooling system must also be selected considering additional criterias like manufacturing possibilities and price.

12 Tracking

As mentioned in Section 3, a tracking system for controlling the movement of the robot during operation is necessary. In this section, the most important points concerning the tracking system will be discussed. The focus is not on the algorithms but on the geometrical circumstances that must be considered.

12.1 Tracking Systems

Beyond other tracking systems, visual and ultrasonic tracking systems are an actual field of research and offer a promising possibility for tracking microrobots in the eye. It is possible to look through the lens of the eye inside the eye. The vitreous body is transparent and therefore it is possible to use visual tracking. Also ultrasonic tracking could be used due to the material properties of the eye and the microrobots.

12.1.1 Visual Tracking

To locate an object in the 3D-space by using visual tracking needs at least two lines of view pointing on the object in different angles. Normally, two cameras are used having perpendicular lines of sights. If it is not possible to arrange the two cameras pointing from different sides on the tracking object, special set-ups are needed.
A possible camera set-up that allows looking from one side on the tracking object is shown in Figure 60. In this set-up, the cameras does not have to point from different angles onto the object. The line of view is only split into two lines of view pointing from different angles on the objects after the cameras. That allows to look with one camera from one side onto the object and to split the view just before the object chamber .

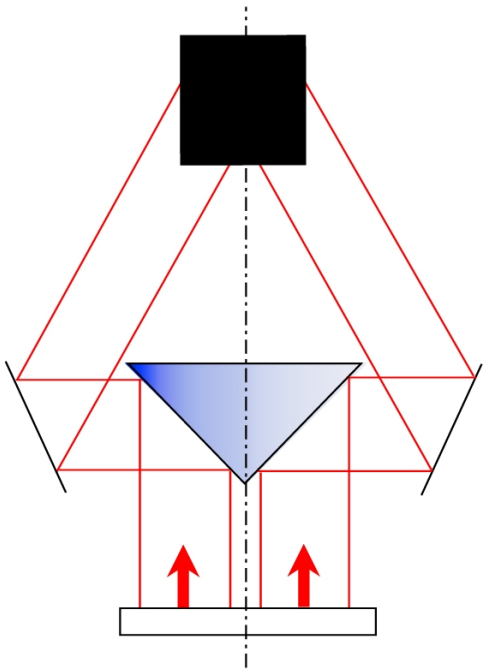

Figure 60: One Directional Camera Set-up

In this set-up, one camera is looking onto a 45°prism. This prism splits the view into two parts. With two mirrors, the line of sight is then mirrored onto the object with an angle. Using only one camera looking onto the prism divides the image into two parts. The same set-up can also be used with two cameras looking onto the prism. Each camera is then looking onto one cathetus of the prism. Using two cameras has the advantage of having the full image of each camera. On the other hand, two cameras need more space, especially, when the position of the cameras has to be compensated to enlarge the space where the microrobot can be tracked.

This set-up makes sense, if the tracking algorithm should be kept simple and it is not possible to have two static line of sights being not covered any time during operation due to moving parts. Otherwise, more cameras are needed to replace cameras that are covered by moving parts in some configuration or moving cameras are needed. In this case the tracking algorithms are getting more complex.

Another important point is the field of view of the cameras. Using microscope lenses allows to have a large image of the robot and follow its actions visually. On the other hand, using microscope lenses reduces the field of view. If the workspace for the robot is larger than the field of view of the cameras, the position of the field of view has to be corrected during the operation. Beyond additional software design effort, additional hardware is required.
When building a smaller prototype for a steering system where the cameras should look through the coils, either the inner diameter of the coils has to be large enough, so that the camera can be moved inside the coil so far, that the whole workspace can be covered, or the camera has to be placed outside the coil, so that only the field of view has to be moved inside the coil (Figure 61).

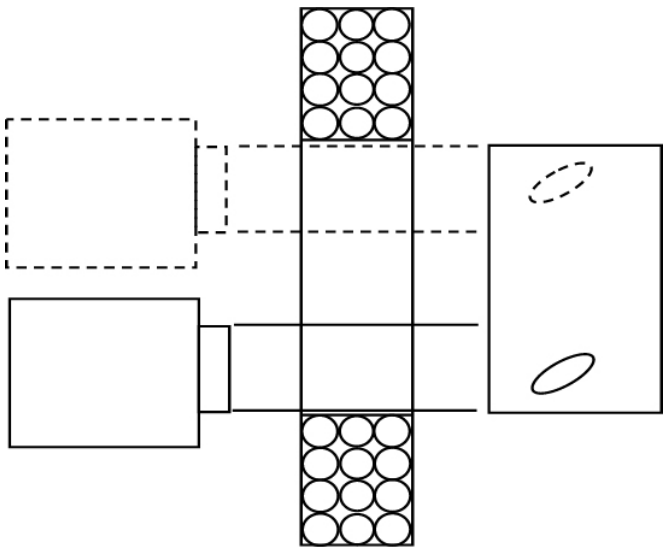

Figure 61: Camera looking through a coil on the object box

12.1.2 Ultrasonic Tracking

For ultrasonic tracking normally three transmitters and receivers are needed to determine the position of an object in the 3D-space. The axis of these three ultrasonic "rays" must not be aligned, otherwise one or two dimensions are getting lost for the position determination.

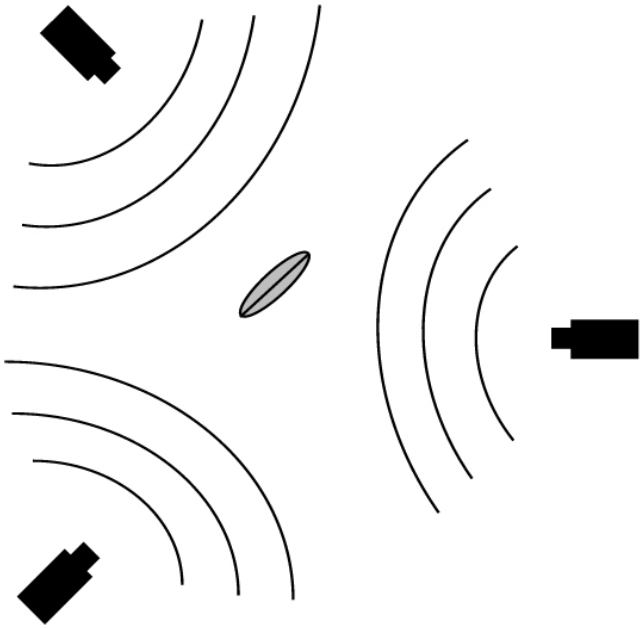

Figure 62: Ultrasonic tracking principle

The basic principle of an ultrasonic tracking system is to measure the time between sending and receiving a signal from ultrasonic waves. By placing the ultrasonic sources at different positions, from the delay time of the three signals, the position of ultrasonic wave reflecting object can be determined.

13 Conclusions and Future Work

Building a steering system for microrobot machines is a complex process which involves interests from many fields of research. Before the actual designing process of a steering system can be begun, knowledge about the fundamental behavior of microrobot machines in different environments must be achieved. Only then the engineering design process can be started and different system solutions can be discussed.

During this project, new insights into a better understanding of the interaction forces and properties of the IRIS microrobots in different environments like flowing fluids and the eye vitreous have been gained. The comprehensive analysis about different magnetic propulsion mechanisms made it possible to go into detail and make first drafts for different configurations of magnetic field generation devices that allow a 3D steering of a microrobot. It was shown, that there are different system configurations based on air core coils that allow to propel and steer a microrobot in the 3D space. Due to electromechanical difficulties in building such a system as a laboratory prototype, further analysis about alternative concepts for other field generation devices like permanent magnet systems have been done.

There are now different ways to continue with building a computer controlled magnetic steering system for biomicrorobots. Figure 63 shows schematically the different ways to go. One possible way would be to get more knowledge about the forces of interaction. Therefore, one point would be to determine the magnetization of the IRIS microrobots more precisely by using a better test set-up for the magnetization measurements and to modify the viscosity model of the pig eye.
The other possible way to continue the work would be to directly make a decision for a certain type of magnetic field generation device used for the steering system. If the decision is to use air core coils, one can either directly chose the way of designing a system using high conducting or superconducting coils, or otherwise to redimension the required forces for the system. If weaker forces are required, a laboratory prototype system based on common air core coils can be built. Independent of this considerations, the 2-coil pairs configuration for the coils is recommended. Comparing the advantages and disadvantages of the different sys-

tem configurations, this system will be the best solution for a prototype magnetic steering system, that also can be scaled up to human size (Section 10.2).
Instead of building a system based on air core coils, a system based on permanent magnets may also be taken into consideration. In that case, first of all additional configuration studies are recommended. For the basic concepts of adjusting the field strength by having rotating magnet pairs (Section 9.3.1), some simple test set-ups would be helpful evaluate the achievable magnetic field strength. Using such a test set-up would also allow to simulate superimposing field effects and to measure the resulting magnetic fields when superimposing the fields from Maxwell and Helmholtz configurations. Only after these configuration studies, one can start with the final design for a magnetic steering system prototype based on permanent magnets.

Which way is chosen is also dependent on the research topics that should be reached by having a magnetic steering system prototype. If not only steering of a robot inside an eye vitreous is the goal, but the system should also be used as a platform for testing different tracking systems or control algorithms, then one may can also deal with weaker forces. Anyway, it is the right way to go on building a prototype for a future oriented system that will bring improvements in the field of medical assistant devices.

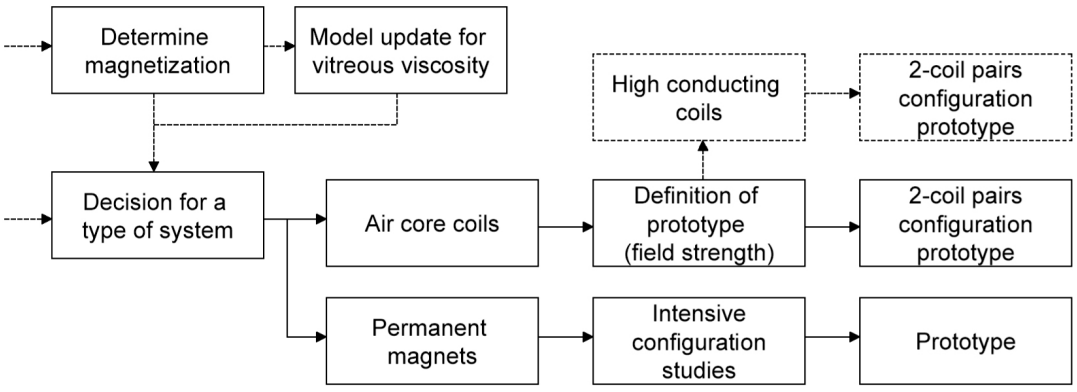

Figure 63: Future work

References

[1] R. Bowtell and A. Peters. Analytic approach to the design of transverse gradient coils with co-axial return paths. In *Magnetic Resonance in Medicine*, volume 41, March 1999. ISSN 0740-3194.

[2] B. D. Cullity. *Introduction To Magnetic Materials*. Addison-Wesley Series in Metallurgy and Materials. Addison-Wesley, Menko Park, CA, 1972. ISBN 0-201-01218-9.

[3] A. Despopoulos and S. Silbernagl. *Color Atlas of Physiology*. Thieme, Stuttgart, Germany, 5 edition, 2003. ISBN 3-13-545005-8.

[4] R. Feynman, R. Leighton, and M. Sands. *The Feynman Lectures on Physics Vol.2*. Addison-Wesley publishing company, 1964. ISBN 0-201-51004-9.

[5] E. P. Furlani. *Permanent Magnet And Electromechanical Devices*. Academic Press, San Diego, CA, 2001. ISBN 0-12-269951-3.

[6] L. Gehm. *Rheologie - Praxisorientierte Grundlagen und Glossar*. Vincentz Verlag, Hannover, Deutschland, 1998. ISBN 3-87870-449-6.

[7] M. S. Grady, M. A. Howard, J. A. Molloy, R. C. Ritter, E. G. Quate, and G. T. Gillies. Nonlinear magnetic stereotaxis: Three-dimensional, in vivo remote magnetic manipulation of a small object in canine brain. *Medical Physics*, 17:405–415, May 1990.

[8] P. G. Jasonov, D. K. Nurgaliev, B. V. Burov, and F. Heller. A modernized coercivity spectrometer. *Geologica Carpathica*, 49:224–225, 1998.

[9] J. Jin. *Electromagnetic Analysis and Design in Magnetic Resonance Imaging*. CRC Press, Boca Raton, Fla., 1999. ISBN 0-8493-9693-X.

[10] P. K. Kundu and I. M. Cohen. *Fluid Mechanics*. Academic Press, San Diego, CA, 2 edition, 2002. ISBN 0-12-178251-4.

[11] B. Lee. *Comparative rheological studies of the vitreous body of the eye*. PhD thesis, University of Pennsylvania, Michigan, 1992.

[12] A. Meier. *Gimbaled Electromagnetic Coil for Guidance and Propulsion of Magnetic Micro Robots*. Semester thesis, Institute of Robotics and Intelligent Systems, ETH Zurich, 2004.

[13] T. Nakamura and M. B. Khamesee. A prototype mechanism for three-dimensional levitated movement of a small magnet. In *IEEE/ASME Transactions on Mechatronics*, volume 2, March 1997.

[14] B. J. Nelson. Bio micro robotics: Robotics for exploring life. *Bulletin Magazine*, (292), February 2004. (in German only).

[15] U. D. Nguyen, J. S. Brwon, I. A. Chang, J. Krycia, and M. S. Mirotznik. Numerical evaluation of heating of the human head due to magnetic resonance imaging. In *IEEE Transactions on Biomedical Engineering*, volume 51, August 2004. ISSN 0018-9294.

[16] D. Poulikakos and J. Gass. *Script Thermodynamics II*. ETH Zurich, Laboratory for Thermodynamics in Emerging Technologies, 2002.

[17] P. A. Tipler. *Physik*. Spektrum, 1 edition, 2000. ISBN 3-86025-122-8.

[18] J. Visser-Heerema. *Über das spezifische Gewicht der bei der Operation von der Netzhautablösung gewonnenen Flüssigkeit*. In Arch. Augenheilkd., volume 109, pp. 543 - 61, 1936.

[19] K. B. Yesin, K. Vollmers, and B. J. Nelson. Analysis and design of wireless magnetically guided microrobots in body fluids. In *Proc. of 2004 IEEE Int. Conf. on Robotics and Automation, New Orleans*, April 2004.

A Robot Configurations

Today, four different kind of robots are used at IRIS. In this report, the robots are identified by numbers from 1 to 4. All of these robots are assembled from the basic parts shown in Figure 64

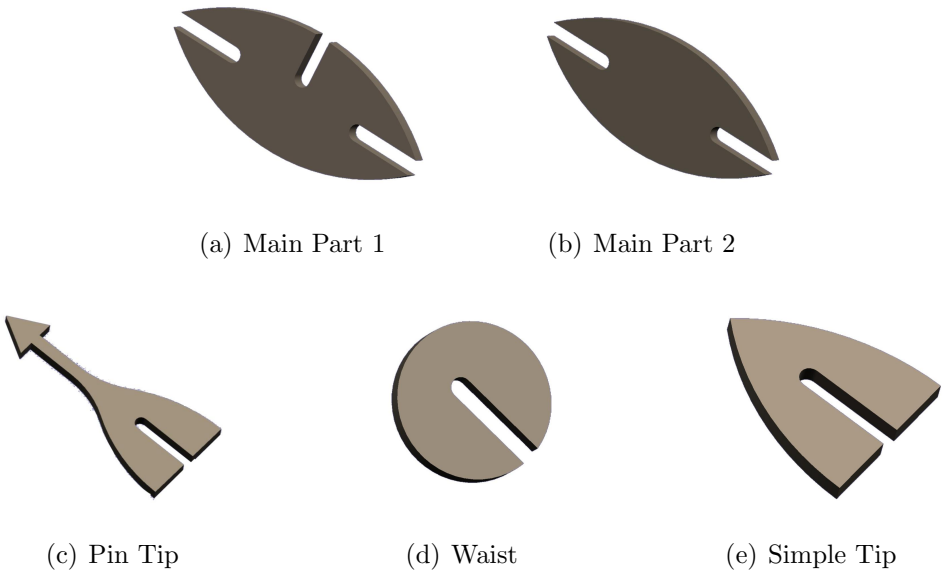

(a) Main Part 1 (b) Main Part 2

(c) Pin Tip (d) Waist (e) Simple Tip

Figure 64: Parts of the Microrobot

The volume as well as the moment of inertia of the parts and the robots is taken from the CAD-files. The volume of the individual parts is with respect to a part thickness of 50 nm:

- $V_{MainPart1}$ $1.223 \cdot 10^{-11}$ m^3
- $V_{MainPart2}$ $1.27 \cdot 10^{-11}$ m^3
- $V_{SimpleTip}$ $6.27 \cdot 10^{-12}$ m^3
- V_{PinTip} $7.57 \cdot 10^{-12}$ m^3
- V_{Waist} $5.76 \cdot 10^{-12}$ m^3

A.1 Robot 1

Robot number 1 is built from main part No. 2 and two simple tips.

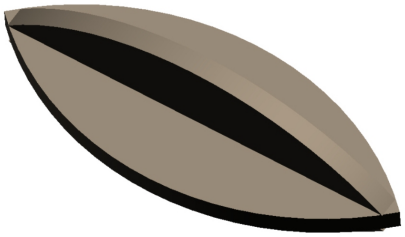

Figure 65: Robot 1

Volume: $2.523 \cdot 10^{-11} m^3$
Mass: $2.25 \cdot 10^{-7} kg$

Principal Moments of Inertia:
I_{xx}**:** $2.47 \cdot 10^{-15} kgm^2$
I_{yy}**:** $1.23 \cdot 10^{-14} kgm^2$
I_{zz}**:** $1.23 \cdot 10^{-14} kgm^2$

A.2 Robot 2

Robot number 2 is built from main part No. 1, a simple, a pin tip as well as a waist.

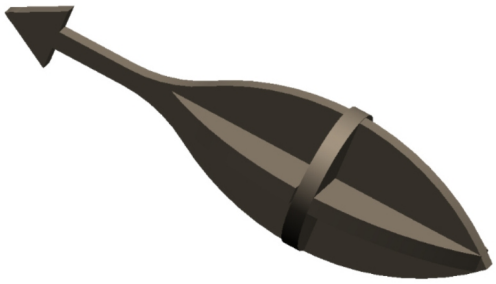

Figure 66: Robot 2

Volume: $3.22 \cdot 10^{-11} m^3$
Mass: $2.86 \cdot 10^{-7} kg$

Principal Moments of Inertia:
I_{xx}**:** $3.54 \cdot 10^{-15} kgm^2$
I_{yy}**:** $2.07 \cdot 10^{-14} kgm^2$
I_{zz}**:** $2.07 \cdot 10^{-14} kgm^2$

A.3 Robot 3

Robot number 3 is built from main part No. 2, a simple and a pin tip.

Volume: $3.22 \cdot 10^{-11} m^3$
Mass: $2.86 \cdot 10^{-7} kg$

Principal Moments of Inertia:
I_{xx}**:** $2.49 \cdot 10^{-15} kgm^2$
I_{yy}**:** $2.00 \cdot 10^{-14} kgm^2$
I_{zz}**:** $2.00 \cdot 10^{-14} kgm^2$

Figure 67: Robot 3

A.4 Robot 4

Robot number 4 is built from main part No. 1, two simple tips as well as a waist.

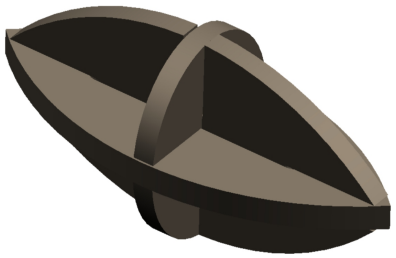

Volume: $3.22 \cdot 10^{-11} m^3$
Mass: $2.86 \cdot 10^{-7} kg$

Principal Moments of Inertia:
I_{xx}**:** $3.53 \cdot 10^{-15} kgm^2$
I_{yy}**:** $1.27 \cdot 10^{-14} kgm^2$
I_{zz}**:** $1.27 \cdot 10^{-14} kgm^2$

Figure 68: Robot 4

B Calculations

In this appendix only the most important formulas and theorems are listed. Verifications of the mentioned theorems and laws can i.e. be found in "The Feynman Lectures on Physics" [4].

B.1 Maxwell's Equations

1. Gauss' law:

$$\oint_A \vec{E} dA = \frac{1}{\epsilon_0} Q \tag{B.1}$$

where Q is the charge inside the volume defined by the area A:

$$Q_{inside} = \iiint \rho dV \tag{B.2}$$

2. Conservation of flux:

$$\oint_A \vec{B} dA = 0 \tag{B.3}$$

3. Faraday's law:

$$\oint_s \vec{E} d\vec{s} = -\int_s \frac{d\vec{B}}{dt} = -\frac{d\Phi}{dt} \tag{B.4}$$

4. Extension of Ampere's circuital law:

$$\oint_s \vec{B} ds = \mu_0 \epsilon_0 \frac{d}{dt} \iint \vec{E} d\vec{a} + \mu_0 I \tag{B.5}$$

B.2 Lorentz Force

The force exerted on a moving charge in a magnetic field is called Lorentz force and is given by:

$$\vec{F} = q(\vec{E} + \vec{u} \times \vec{B}) \tag{B.6}$$

The Lorentz force shows that there are actually two forces exerted on the charge. The first component of the force is the electrical force that is independent of the movement of the charge and can be defined by the electrical field strength $\vec{E}$:

$$\vec{F} = q\vec{E} \tag{B.7}$$

The second force component is the magnetic force and is dependent on the movement of the charge. The magnetic force is normal to the movement direction of the charge and the magnetic field vector $\vec{B}$:

$$\vec{F} = q\vec{u} \times \vec{B} \tag{B.8}$$

B.3 Ampere's Circuital Law

Ampere's circuital law states, that the circulation of the magnetic field intensity around any closed path is equal to the free current flowing through the surface bounded by the path:

$$\oint_s \vec{B} \cdot ds = \mu_0 I_S \tag{B.9}$$

B.4 Magnetic Field

The primary vectors defining the magnetostatic field in a magnetized manner are the magnetic field strength $\vec{H}$, the magnetization of the matter $\vec{M}$ and the magnetic flux density $\vec{B}$. The relationship between these vectors is:

$$\vec{B} = \mu_0(\vec{M} + \vec{H}) \tag{B.10}$$

For linear, homogeneous and isotropic materials, $\vec{B}$ and $\vec{M}$ are proportional to $\vec{H}$. Therefore the magnetization can be rewritten as:

$$\vec{M} = \chi\vec{H} \tag{B.11}$$

$\vec{B}$ can bet set in relation to $\vec{H}$ by defining an "absolute permeability" [5]:

$$\mu = \frac{\vec{B}}{\vec{H}} \tag{B.12}$$

$$\begin{aligned} \vec{B} &= \mu_0\vec{H} \qquad \text{(in vacuum)} \\ \vec{B} &= \mu_r\mu_0\vec{H} \quad \text{(in material)} \end{aligned} \tag{B.13}$$

Notice that χ and μ are related to one another:

$$\begin{aligned} \mu &= \mu_0(\chi + 1) \\ \chi &= \frac{\mu}{\mu_0} - 1 \end{aligned} \tag{B.14}$$

There is also a so called "relative permeability" [17]:

$$\mu_r = \frac{\mu}{\mu_0} = \frac{B}{B_0} \tag{B.15}$$

(B is the magnetic field inside the material and B_0 is the external magnetic field)

B.5 Biot-Savart Law

$$d\vec{B} = \frac{\mu_0}{4\pi} I \frac{d\vec{s} \times \vec{r}}{r^3} \tag{B.16}$$

B.5.1 B-field of a Linear Segment of a Wire Carrying a Current

Applying Biot-Savart's law (Eq. B.16), the B-field of a segment of a wire carrying the current I can be determined.

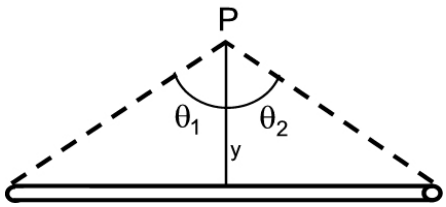

Figure 69: Linear wire segment

$$B = \frac{\mu_0}{4\pi} \frac{I}{y} \left(sin(\Theta_1) + sin(\Theta_2) \right) \tag{B.17}$$

B.5.2 B-field along the Axis of a Coil

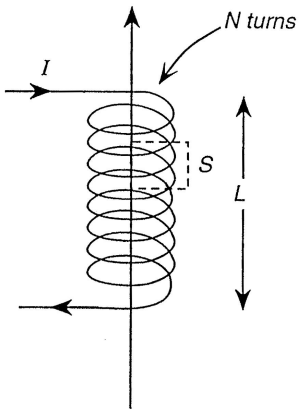

Figure 70: Solenoid [5]

Applying Ampere's circuital law B.9 we can determine the B-field along the z-axis of a air core coil. Apply Eq. B.9 to a rectangular path with one side of length S along the axis of the coil and the other parallel side just outside the coil. So we can determine the B-field to:

$$B_z = \mu_0 \frac{N}{L} I \tag{B.18}$$

To steer a microrobot by applying a magnetic field, the progression of the magnetic field outside the coil is important.
Biot-Savart law facilitates to determine the B-field outside a air core coil. Applying Eq. B.16 relates to:

$$B_z = \int_0^{2\pi} \frac{\mu_0}{4\pi} I \frac{a^2 d\phi}{(z^2 + a^2)^{\frac{3}{2}}} = \frac{\mu_0}{2} I \frac{a^2}{(z^2 + a^2)^{\frac{3}{2}}} \tag{B.19}$$

B.6 Magnetization

In general, the values derived for the suceptibility and the relative permeability are not constant but change with magnetization. The dependency of the magnetization of the material in an external magnetic field is described by a so called "hysteresis curve". The relationship between the external field and the magnetization is non-linear and the response of the material also changes with its previous state of magnetization. There exists also a saturation magnetization that can be be obtained by [17]:

$$M_s = n m_m \tag{B.20}$$

$$n = \frac{N_A}{M_m} \rho \tag{B.21}$$

where n is the density number of the molecules, m_m magnetic moment of each molecule, N_A the Avogadro-number, M_m the molar mass and ρ the density of the material .

The magnetization of a matter by in an external magnetic field can be be determined from

$$M = \frac{B - B_0}{\mu_0} \tag{B.22}$$

that can be rewritten by using (B.15):

$$M = \frac{\mu_r B_0 - B_0}{\mu_0} \tag{B.23}$$

The magnetization also depends on the shape of the specimen. When a specimen is magnetized, a self-field develops within it that opposes the magnetizing field. This is called the demagnetization field. For ellipsoidal shapes, analytical expressions have been derived to determine the demagnetization field and its influence on the magnetization [5].

B.6.1 Force on a Magnet in an External Field

$$\vec{F} = \int_V (\vec{M} \cdot \bigtriangledown) \vec{B}_{ext} dv \tag{B.24}$$

B.6.2 Torque on a Magnet in an External Field

$$\vec{T} = \int_V \vec{M} \times \vec{B}_{ext} dv \tag{B.25}$$

B.7 Bar Magnet

The field outside a bar magnet can be analytically calculated. The x-component is given by

$$B_x(x,y,z) = \frac{\mu_0 M_s}{4\pi} \sum_{k=1}^{2} \sum_{m=1}^{2} (-1)^{k+m} ln[F(x,y,z,x_m,y_1,y_2,z_k)] \tag{B.26}$$

where

$$F(x,y,z,x_m,y_1,y_2,z_k) = \frac{(y-y_1) + [(x-x_m)^2 + (y-y_1)^2 + (z-z_k)^2]^{\frac{1}{2}}}{(y-y_2) + [(x-x_m)^2 + (y-y_2)^2 + (z-z_k)^2]^{\frac{1}{2}}} \tag{B.27}$$

The y-component is given by

$$B_y(x,y,z) = \frac{\mu_0 M_s}{4\pi} \sum_{k=1}^{2} \sum_{m=1}^{2} (-1)^{k+m} ln[H(x,y,z,x_1,x_2,y_m,z_k)] \tag{B.28}$$

where

$$H(x,y,z,x_1,x_2,y_m,z_k) = \frac{(x-x_1) + [(x-x_1)^2 + (y-y_m)^2 + (z-z_k)^2]^{\frac{1}{2}}}{(x-x_2) + [(x-x_2)^2 + (y-y_m)^2 + (z-z_k)^2]^{\frac{1}{2}}} \tag{B.29}$$

The z-component is given by

$$\begin{aligned} B_z(x,y,z) =& \frac{\mu_0 M_s}{4\pi} \sum_{k=1}^{2} \sum_{n=1}^{2} \sum_{m=1}^{2} (-1)^{k+n+m} \\ & \times tan^{-1} \left(\frac{(x-x_n)(y-y_m)}{(z-z_k)} g(x,y,z,;x_n,y_m,z_k) \right) \end{aligned} \tag{B.30}$$

where

$$g(x,y,z;x_n,y_m,z_k) = \frac{1}{((x-x_n)^2 + (y-y_m)^2 + (z-z_k)^2)} \tag{B.31}$$

The gradient is given by

$$\begin{aligned}\frac{dB_z}{dz} =& \frac{\mu_0 M_s}{4\pi} \sum_{k=1}^{2}\sum_{n=1}^{2}\sum_{m=1}^{2}(-1)^{k+n+m}\Bigg((x-x_n)(y-y_m)* \\ & \Bigg(-\frac{1}{\left((x-x_n)^2+(y-y_m)^2+(z-z_k)^2\right)^{1.5}}- \\ & \frac{1}{\left((x-x_n)^2+(y-y_m)^2+(z-z_k)^2\right)^{0.5}(z-z_k)^2}\Bigg)\Bigg)/ \\ & \left(1+\frac{(x-x_n)^2(y-y_m)^2}{\left((x-x_n)^2+(y-y_m)^2+(z-z_k)^2\right)(z-z_k)^2}\right)\end{aligned} \tag{B.32}$$

C Calculation of Errors

C.1 Validation of Drag Force Experiments

C.1.1 Forces Equilibrium - Calculation of Errors

The drag force is calculated by the forces equilibrium and can therefore be written as:

$$F_D = F_G - F_B \tag{C.1}$$

The radius of the spheres, the mass of the spheres, the viscosity of the fluid (oil), and the density of the fluid are measured values. The density of the fluid is determined by measuring a specific volume of the fluid and then measuring the weight of this amount of fluid. All this measurements are afflicted with an uncertainty.
The drag force builded with this value can be written as

$$\begin{aligned} F_D &= F_G - F_B \\ &= m_s g - \rho_f V_s g \\ &= m_s g - \frac{m_f}{V_f}\frac{4}{3}\pi r_s^3 g \end{aligned} \tag{C.2}$$

The relative error of the gravity force is dependent of the weight measurement. Therefore, the error of the gravity force can be calculated.

Average weight of a bearing sphere:	0.7053 g
Inaccuracy of the balance:	5 mg

Therefore, the relative uncertainty of the gravity force is 0.7%.

The error of the buoyancy force is obtained by

$$\begin{aligned} \triangle F_B &= \sqrt{\left(\frac{\partial F_B}{\partial m_f}\triangle m_f\right)^2 + \left(\frac{\partial F_B}{\partial V_f}\triangle V_f\right)^2 + \left(\frac{\partial F_B}{\partial r_s}\triangle r_s\right)^2} \\ &= \sqrt{\left(\frac{4g\pi r_s^3}{3V_f}\triangle m_f\right)^2 + \left(\frac{4gm_f\pi r_s^3}{3V_f^2}\triangle V_f\right)^2 + \left(\frac{4gm_f\pi r_s^2}{V_f}\triangle r_s\right)^2} \end{aligned} \tag{C.3}$$

The relative uncertainty of the terms in (C.3) are with respect to the following measurements:

Measured weight of 2 ml oil AK1000:	1.972 g
Inaccuracy of the balance:	5 mg
Inaccuracy of fluid volume measurements of 2 ml:	0.05 ml
Measured radius of the bearing sphere:	2.75 mm
Inaccuracy of radius measurement:	0.025 mm

Using these values in (C.3), the total uncertainty of the buoyancy force is $4.618 \cdot 10^{-5} N$, where the relative uncertainty is 5.34% due to measurement inaccuracies.

C.1.2 Stokes Drag Force - Calculation of Errors

The value for the drag force is also determined by applying Stokes law:

$$F_D = 6\pi\mu_f r_s v_s \tag{C.4}$$

The uncertainty for Stokes drag force is obtained with

$$\begin{aligned} \triangle F_D &= \sqrt{\left(\frac{\partial F_D}{\partial \mu_f}\triangle\mu_f\right)^2 + \left(\frac{\partial F_D}{\partial r_s}\triangle r_s\right)^2 + \left(\frac{\partial F_D}{\partial v_s}\triangle v_s\right)^2} \\ &= \sqrt{\left(6\pi r_s v_s \triangle\mu_f\right)^2 + \left(6\pi\mu_f v_s \triangle r_s\right)^2 + \left(6\pi\mu_f r_s \triangle v_s\right)^2} \end{aligned} \tag{C.5}$$

Using the following measurement values (values for measurement number 3 in Section 4.3.4),

Measured radius of the bearing sphere:	2.75 mm
Inaccuracy of radius measurement:	0.025 mm
Measured viscosity at 23.5°:	1003.85 $mPa\ s$
Inaccuracy of viscosity measurement:	1 $mPa\ s$
Measured velocity of the sphere:	0.104 m/s
Inaccuracy of velocity measurement:	0.001 m/s

a total uncertainty of $7.18 \cdot 10^{-5} N$ and a relative uncertainty of 1.32% is obtained.

C.1.3 Oseens Drag Force - Calculation of Errors

Using Oseens approximation, the drag force is calculated from the measured values by

$$F_D = \frac{3\pi r_s(3m_f r_s v_s + 8\mu V_f)v_s}{4V_f} \tag{C.6}$$

The uncertainty is calculated by

$$\begin{aligned}\triangle F_D =& \sqrt{\left(\frac{\partial F_D}{\partial \mu_f}\triangle\mu_f\right)^2 + \left(\frac{\partial F_D}{\partial r_s}\triangle r_s\right)^2 + \left(\frac{\partial F_D}{\partial v_s}\triangle v_s\right)^2 + \left(\frac{\partial F_D}{\partial V_f}\triangle V_f\right)^2 + \left(\frac{\partial F_D}{\partial m_f}\triangle m_f\right)^2} \\ =& \Bigg((6\pi r_s v_s \triangle\mu_f)^2 + \left(\frac{3\pi(3m_f r_s v_s + 4\mu_f V_f)v_s}{2V_f}\triangle r_s\right)^2 + ... \\ & \left(\frac{3\pi(3m_f v_s r_s + 4\mu_f V_f)r_s}{2V_f}\triangle v_s\right)^2 + \left(\frac{-9m_f\pi r_s^2 v_s^2}{4V_f^2}\triangle V_f\right)^2 + ... \\ & \left(\frac{9\pi r_s^2 v_s^2}{4V_f}\triangle m_f\right)^2\Bigg)^{1/2}\end{aligned} \tag{C.7}$$

Using the following measurement values (values for measurement number 3 in Section 4.3.4),

Measured radius of the bearing sphere:	2.75 mm
Inaccuracy of radius measurement:	0.025 mm
Measured viscosity at 23.5°:	1003.85 $mPa\ s$
Inaccuracy of viscosity measurement:	1 $mPa\ s$
Measured velocity of the sphere:	0.104 m/s
Inaccuracy of velocity measurement:	0.001 m/s
Measured weight of 2 ml oil AK1000:	1.972 g
Inaccuracy of the balance:	0.005 kg
Inaccuracy of fluid volume measurements of 2 ml:	0.05 ml

we obtain a total uncertainty of $1.4365 \cdot 10^{-4} N$ and a relative uncertainty of 2.38% for Oseens drag force.

C.2 Microrobot Drag Number

The drag number has been experimentally determined in Section 4.3.3 by Equation 4.11:

$$D_N = \frac{F_{DragForce}}{\mu_f v_f}$$

The drag force has been calculated from the difference between the gravity force and the buoyancy force. Therefore the drag number can be written as:

$$\begin{aligned} D_N &= \frac{F_G - F_B}{\mu_f v_m} \\ &= \frac{V_m \rho_m g - V_m \frac{m_f}{V_f} g}{\mu_f v_m} \end{aligned}$$

The error of the drag number is the calculated by

$$\begin{aligned} \triangle D_N =& \left(\left(\frac{\partial D_N}{\partial V_m} \triangle V_m \right)^2 + \left(\frac{\partial D_N}{\partial m_f} \triangle m_f \right)^2 + \left(\frac{\partial D_N}{\partial V_f} \triangle V_f \right)^2 + ... \right. \\ & \left. \left(\frac{\partial D_N}{\partial \mu_f} \triangle \mu_f \right)^2 + \left(\frac{\partial D_N}{\partial v_m} \triangle v_m \right)^2 \right)^{1/2} \\ =& \left(\left(\frac{-g(m_f - \rho_m V_f)}{\mu_f V_f v_m} \triangle V_m \right)^2 + \left(\frac{-g V_m}{\mu_f V_f v_m} \triangle m_f \right)^2 + ... \right. \\ & \left(\frac{g m_f V_m}{V_f^2 \mu_f v_m} \triangle V_f \right)^2 + \left(\frac{g(\mu_f - \rho_m V_f) V_m}{\mu_f^2 V_f v_m} \triangle \mu_f \right)^2 + ... \\ & \left. \left(\frac{g(m_f - \rho_m V_f) V_m}{v_m^2 \mu_f V_f} \triangle v_m \right)^2 \right)^{1/2} \end{aligned} \tag{C.8}$$

For the calculation of the error, the following assumptions are done:
The density of the robot (Nickel) is assumed to be exact.

Volume of microrobot 1:	$2.524 \cdot 10^{-11}\ m^3$
Volume of microrobot 2:	$3.585 \cdot 10^{-11}\ m^3$
Volume of microrobot 3:	$2.654 \cdot 10^{-11}\ m^3$
Volume of microrobot 4:	$3.050 \cdot 10^{-11}\ m^3$
Inaccuracy of microrobot volumes:	$1 \cdot 10^{-13}\ m^3$

Inaccuracy of viscosity measurement:	1 $mPa\ s$
Inaccuracy of the measured velocity (AK100):	0.1 mm/s
Inaccuracy of the measured velocity (AK350):	0.03 mm/s
Inaccuracy of the measured velocity (AK1'000):	0.001 mm/s

The Inaccuracy of the measured velocity is dependent on the viscosity of the fluid. The precision of the measurement is dependent on the frame rate and the total number of the frames available for the velocity determination. The frame rate is the same for all measurements, but the total number of frames is dependent on the time needed to cross the field of view of the camera and this value is dependent on the viscosity of the oil.
Using these values the error of the measurements for the drag number can be calculated. Table 13 shows the average error of the determined drag number for the four different robots in the silicon oils AK1000, AK350 and AK1'000.

Oil	**Robot No.**	**Average error [mm]**	**Average relative error [%]**
AK100	1	0.256	4.89
AK100	2	0.202	3.92
AK100	3	0.239	4.67
AK100	4	0.199	4.03
AK350	1	0.21	4.69
AK350	2	0.183	3.80
AK350	3	0.200	4.45
AK350	4	0.201	4.00
AK1'000	1	0.196	3.98
AK1'000	2	0.157	3.17
AK1'000	3	0.190	3.79
AK1'000	4	0.165	3.30

Table 13: Errors for drag number D_N

D Guidelines for a Microrobot Steering System

There are no special guidelines for steering systems for biomicrorobots, but there are guidelines for MRI systems. As well as the MRI systems, the steering system for the microrobots will be used in medical applications. From the point of interaction between the system and the human body, both systems are quite similar. Both systems are working with static as well as changing magnetic fields that affect not only specific parts in the body but also affect the whole human body in the influence area of the system. Therefore, the guidelines established for the MRI systems can also be used as guidelines for a microrobots steering system.

D.1 Potential Dangers due to Electromagnetic Fields

The guidelines for systems creating and working with electromagnetic fields have been set to minimize the risk of getting injured while working with such systems. There are different exposures due to the magnetic fields. The exposures can be segmented to the different fields.

Static Magnetic Fields
A static magnetic field exerts forces and torques on ferro- and diamagnetic materials. Therefore, objects may be moved at high speeds due to a strong magnetic field and may hurt persons standing nearby. Especially for patients having implants or patients that need other medical equipment (intravenous drips, artificial respiratory equipment, ...) are potentially at risk. There have already been injuries with air tanks pulled into a MRI system due to the high fields. Also electric equipment can be damaged by electromagnetic fields.

Slow Time Varying Fields
These fields can function as an external nerve or muscle stimulation. As well as the static magnetic fields, slow time varying fields can interact with implants, especially cardiac pacemakers.

HF Magnetic Fields

HF[15] magnetic fields can lead to a warming of the human body. The warming of the human body correlates with the frequency of the field. Therefore fields with a higher frequency are potentially more dangerous than fields with a lower frequency [15]. Furthermore, also with HF magnetic fields the danger of interaction with implants and electrical equipment must not be neglected.

D.2 Organizations and Standards

There are several organizations providing guidelines for MRI systems. As with other laws, there are national and international regulations for MRI systems. The most important organizations and standards are:

International:

- International Electrotechnical Commission (IEC)- http://www.iec.ch/
  - IEC 60601-2-33 Requirements for the Safety of MR Equipment for Medical Diagnosis

USA:

- Food and Drug Administration (FDA) - http://www.fda.gov/
  - Guidelines for Premarket Notifications for MR Diagnostic Devices
  - Guidelines for Evaluating Electromagnetic Risk for Trials of Clinical NMR[16] Systems
- National Electrical Equipment Manufacturer's Association (NEMA) - http://www.nema.org/
  - MS 1 through 9 – Safety and Performance Standards
- American Society for Testing and Materials (ASTM) - http://www.astm.org/
  - Test Methods for MR Safety of Implanted Medical Devices

[15]High Frequency
[16]Nuclear Magnetic Resonance

Europe:

- Council of the European Union
  - http://europa.eu.int/institutions/council/index_en.htm
    - Directive 2004/40/EC[17]

D.3 Selection of Regulations

D.3.1 IEC 60601-2-33

The regulation is addressed to the protection of patients. The IEC regulation defines a control region for areas in which fields higher than 0.5 mT can occur. These areas have to be signed. Furthermore, there are three operational modes defined: *Normal Mode, First Level Controlled Mode and Second Level Controlled Mode.*

- In the Normal Mode, a physiological exposure of a person can be excluded. A normal monitoring of the patient in the MRI is adequate. This mode is defined by static magnetic fields up to 2 Tesla.

- In the first controlled mode, a physiological exposure of the patient is possible. Therefore, an adequate medical monitoring is indispensable. The system has to be designed in a way that when higher fields than the normal mode allows are applied, the personnel is alerted and that the new mode has to be confirmed by the personnel. The first level control is defined by static magnetic fields higher than 2 Teslas and lower than 4 Teslas.

- The second level controlled mode can lead to a significant risk for the patient and must only be applied after a clinical examination. The system must not change to this mode by chance. This mode is defined by static magnetic fields higher than 4 Teslas.

[17]European Council

D.3.2 FDA Guidelines

The FDA set limits directed to sponsors, manufactures and researchers of clinical MR devices, and specify levels of the field which when exceeded require evaluation in terms of "significant risk". Summarized the guidelines are:

- Limit for static magnetic fields: 2 T.
- Limit for time-varying fields exposured to the whole or partial body: 3 T/s.
- Limit for RF are fields that result in a specific absorption rate (SAR) of 0.4 W/kg as average over a whole body, or 2W/kg as averaged over any one gram of tissue.

D.3.3 EC Directives

The EC directive addresses the protection of people working with MR systems in the industry as well as at hospitals. The EC directives are not yet finished. Due to the new results from research in the field of electromagnetic fields, some directive proposals have been overridden. In the first proposal of the directive, a peak value of 2 T for static magnetic fields has been proposed. If the exposure to the field is over 8 hours, 200 mT should not be exceeded. For now, these values were discarded. Furthermore, the directive defines limits for time varying gradient fields dependent on the frequency and local SAR values.

The EMF[18] directive was published in spring 2004 and is a mandatory adoption into national law for each EC country within 4 years.

[18]Electro Magnetic Field

E Oil Viscosity

The viscosity of the silicon oils AK100 and AK1'000 has been measured at the ILW at ETH Zurich with a "Physica MCR300" rheometer. For the measurements, a "Couette CC17" measurement geometry has been used. The measurements are done for 20°C and 25°C oil temperature and shear rates from 1/s to 500/s.

For the calculation of the temperature dependency of the viscosity, an approximation with the Arrhenius-Equation is used [6].

$$\mu = A \cdot e^{\frac{E_0}{RT}} \tag{E.1}$$

(A = Frequency factor, E_0 = Activation energy, R = Gas constant, T = Absolute temperature)

In this approximation, the viscosity is decreasing with higher temperature until it reaches a limiting value. For the AK silicon oils, a linear relation between the logarithm of the viscosity and the reciprocal temperature is assumed (Figure 71).

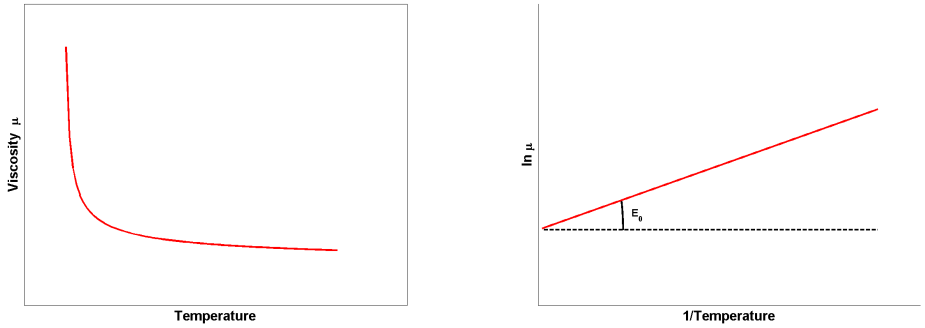

(a) Viscosity-temperature relation (b) Activation energy of the viscous flow

Figure 71: Arrhenius viscosity-temperature

E.1 Viscosity AK100

Measuring Point	**Shear Rate [1/s]**	**Shear Stress [Pa]**	**Viscosity [mPa s]**	**Revolution [1/min]**	**Moment [μNm]**	**Temperature [°C]**
1	500	54,7	109	390	709	19,9
2	483	52,8	109	376	684	19,9
3	466	50,9	109	363	660	19,9
4	448	49	109	349	636	19,9
5	431	47,2	109	336	611	19,9
6	414	45,3	109	323	587	20
7	397	43,4	109	309	562	20
8	379	41,5	109	296	538	20
9	362	39,6	109	282	514	20
10	345	37,7	109	269	489	20
11	328	35,8	109	255	465	20
12	310	34	109	242	440	20
13	293	32,1	109	228	416	20
14	276	30,2	109	215	391	20
15	259	28,3	109	202	367	20
16	241	26,4	109	188	342	20
17	224	24,5	109	175	318	20
18	207	22,6	109	161	294	20
19	190	20,8	109	148	269	20
20	172	18,9	109	134	245	20
21	155	17	109	121	220	20
22	138	15,1	109	108	196	20
23	121	13,2	109	94,1	171	20
24	104	11,3	109	80,7	147	20
25	86,3	9,45	110	67,3	123	20
26	69,1	7,57	110	53,8	98,1	20
27	51,8	5,68	110	40,4	73,6	20
28	34,6	3,79	110	26,9	49,1	20
29	17,3	1,91	110	13,5	24,7	20

Table 14: Viscosity AK100 - 20 °C

Measuring Point	**Shear Rate [1/s]**	**Shear Stress [Pa]**	**Viscosity [mPa s]**	**Revolution [1/min]**	**Moment [μNm]**	**Temperature** [°C]
1	500	49,5	99,1	390	642	25
2	483	47,8	99	376	620	25
3	466	46,1	99,1	363	598	25
4	448	44,4	99	349	576	25
5	431	42,7	99	336	553	25
6	414	41	99	323	531	25
7	397	39,3	99	309	509	25
8	379	37,6	99	296	487	25
9	362	35,9	99	282	465	25
10	345	34,1	99	269	443	25
11	328	32,4	99	255	420	25
12	310	30,7	99	242	398	25
13	293	29	99	228	376	25
14	276	27,3	99	215	354	25
15	259	25,6	99	202	332	25
16	241	23,9	99	188	310	25
17	224	22,2	99	175	288	25
18	207	20,5	99	161	266	25
19	190	18,8	99	148	243	25
20	172	17,1	99	134	221	25
21	155	15,4	99	121	199	25
22	138	13,7	99	108	177	25
23	121	12	99	94,1	155	25
24	104	10,3	99	80,7	133	25
25	86,3	8,55	99,1	67,3	111	25
26	69,1	6,85	99,1	53,8	88,7	25
27	51,8	5,14	99,1	40,4	66,6	25
28	34,6	3,43	99,2	26,9	44,5	25

Table 15: Viscosity AK100 - 25 °C

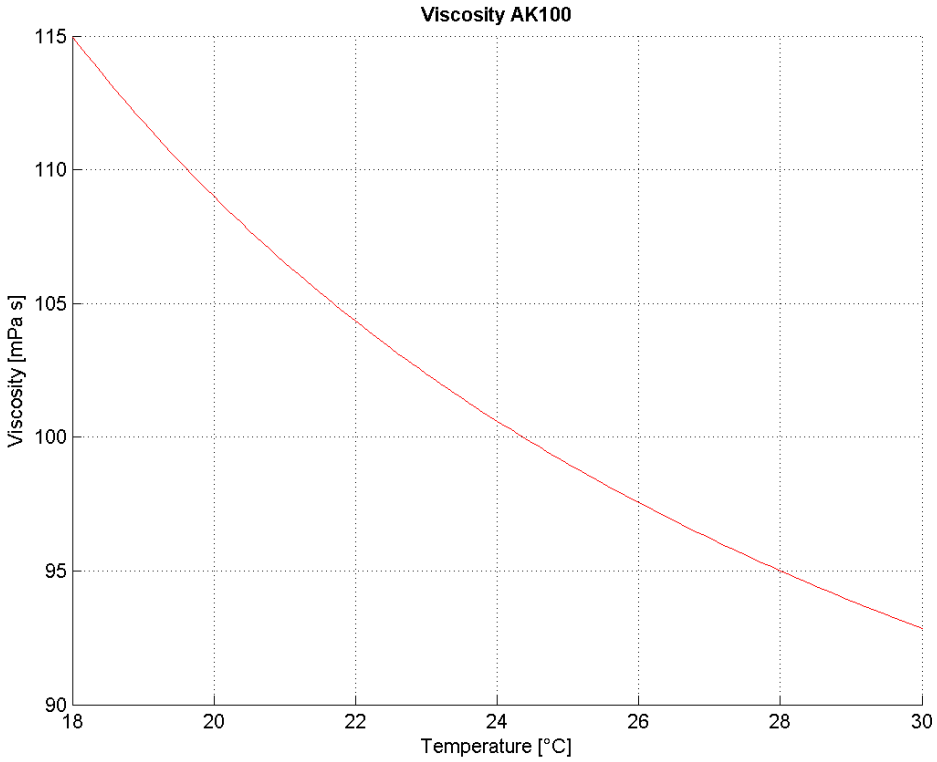

Figure 72: Viscosity silicon oil AK100

E.2 Viscosity AK350

Measuring Point	**Shear Rate [1/s]**	**Shear Stress [Pa]**	**Viscosity [mPa s]**	**Revolution [1/min]**	**Moment [μNm]**	**Temperature [°C]**
1	500	190	379	390	2.460	20
2	483	183	379	376	2.370	20
3	466	177	379	363	2.290	20
4	448	170	379	349	2.200	20
5	431	163	379	336	2.120	20
6	414	157	379	323	2.030	20
7	397	150	379	309	1.950	20
8	379	144	379	296	1.860	20
9	362	137	379	282	1.780	20
10	345	131	379	269	1.690	20
11	328	124	379	205	1.610	20
12	310	118	379	242	1.530	20
13	293	111	379	228	1.440	20
14	276	105	379	215	1.360	20
15	259	98,1	379	202	1.270	20
16	241	91,6	379	188	1.190	20
17	224	85	379	175	1.100	20
18	207	78,5	379	161	1.020	20
19	190	72	379	148	933	20
20	172	65,4	379	134	848	20
21	155	58,9	379	121	764	20
22	138	52,4	380	108	679	20
23	121	45,8	380	94,1	594	20
24	104	39,3	380	80,7	509	20
25	86,3	32,8	380	67,3	425	20
26	69,1	26,2	380	53,8	340	20
27	51,8	19,7	380	40,4	255	20
28	34,6	13,1	380	26,9	170	20
29	17,3	6,6	380	13,5	85.5	20

Table 16: Viscosity AK350 - 20 °C

Measuring Point	**Shear Rate [1/s]**	**Shear Stress [Pa]**	**Viscosity [mPa s]**	**Revolution [1/min]**	**Moment [μNm]**	**Temperature** [°C]
1	500	171	343	390	2.220	25
2	483	165	343	376	2.140	25
3	466	159	343	363	2.070	25
4	448	154	342	349	1.990	25
5	431	148	342	336	1.910	25
6	414	142	342	323	1.840	25
7	397	136	342	309	1.760	25
8	379	130	342	296	1.680	25
9	362	124	342	282	1.610	25
10	345	118	342	269	1.530	25
11	328	112	342	255	1.450	25
12	310	106	342	242	1.380	25
13	293	100	342	228	1.300	25
14	276	94,4	342	215	1.220	25
15	259	88,5	342	202	1.150	25
16	241	82,6	342	188	1.070	25
17	224	76,8	342	175	995	25
18	207	70,9	342	161	919	25
19	190	65	342	148	842	25
20	172	59,1	342	134	766	25
21	155	53,2	342	121	689	25

Table 17: Viscosity AK350 - 25 °C

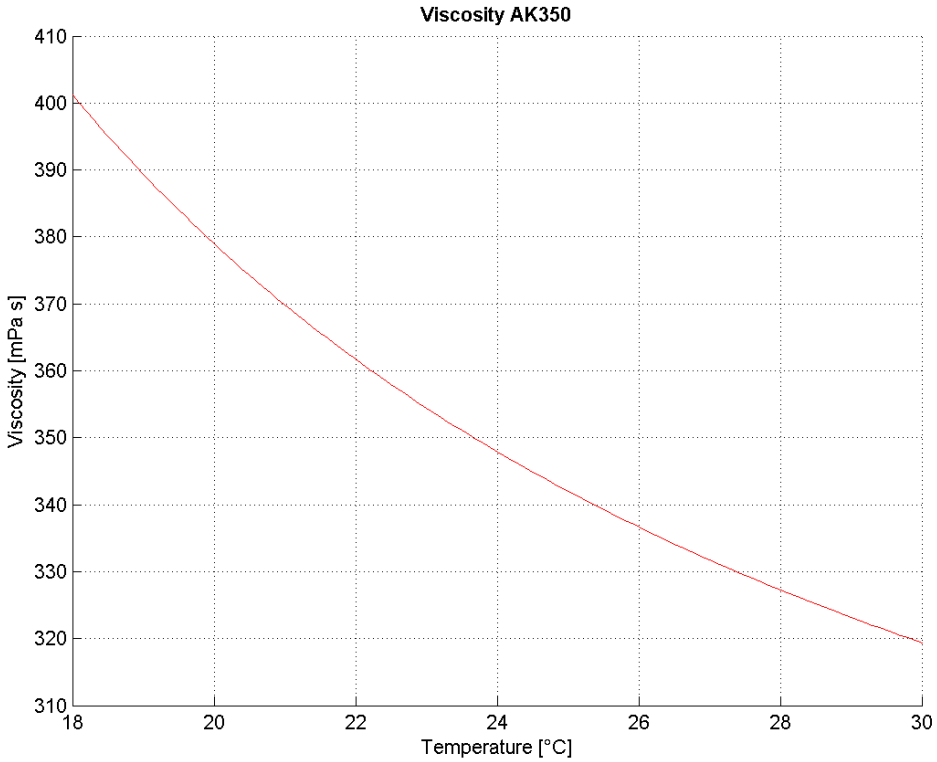

Figure 73: Viscosity silicon oil AK350

E.3 Viscosity AK1000

Measuring Point	**Shear Rate [1/s]**	**Shear Stress [Pa]**	**Viscosity [mPa s]**	**Revolution [1/min]**	**Moment [μNm]**	**Temperature [°C]**
1	500	542	1.080	390	7.030	19,9
2	483	523	1.080	376	6.780	20
3	466	504	1.080	363	6.540	20
4	448	485	1.080	349	6.290	20
5	431	467	1.080	336	6.050	20
6	414	448	1.080	323	5.810	20
7	397	429	1.080	309	5.570	20
8	379	411	1.080	296	5.320	20
9	362	392	1.080	282	5.080	20
10	345	373	1.080	269	4.840	20
11	328	355	1.080	205	4.600	20
12	310	336	1.080	242	4.360	20
13	293	318	1.080	228	4.120	20
14	276	299	1.080	215	3.870	20
15	259	280	1.080	202	3.630	20
16	241	262	1.080	188	3.390	20
17	224	243	1.080	175	2.150	20
18	207	224	1.080	161	2.910	20
19	190	206	1.080	148	2.670	20
20	172	187	1.080	134	2.420	20
21	155	168	1.080	121	2.180	20
22	138	150	1.080	108	1.940	20
23	121	131	1.090	94,1	1.700	20
24	104	112	1.090	80,7	1.460	20
25	86,3	93,7	1.090	67,3	1.210	20
26	69,1	75	1.090	53,8	972	20
27	51,8	56,3	1.090	40,4	629	20
28	34,6	37,6	1.090	26,9	487	20
29	17,3	18,8	1.090	13,5	244	20

Table 18: Viscosity AK1000 - 20 °C

Measuring Point	**Shear Rate [1/s]**	**Shear Stress [Pa]**	**Viscosity [mPa s]**	**Revolution [1/min]**	**Moment [μNm]**	**Temperature** [°C]
1	500	491	981	390	6.360	25
2	483	473	981	376	6.140	25
3	466	456	980	363	5.910	25
4	448	439	980	349	5.690	25
5	431	422	979	336	5.470	25
6	414	405	979	323	5.250	25
7	397	388	979	309	5.030	25
8	379	371	979	296	4.810	25
9	362	354	979	282	4.590	25
10	345	337	979	269	4.370	25
11	328	321	979	255	4.160	25
12	310	304	979	242	3.940	25
13	293	287	979	228	3.720	25
14	276	270	979	215	3.500	25
15	259	253	979	202	3.280	25
16	241	236	979	188	3.060	25
17	224	219	979	175	2.850	25
18	207	203	979	161	2.630	25
19	190	186	979	148	2.410	25
20	172	169	979	134	2.190	25
21	155	152	980	121	1.970	25
22	138	135	980	108	1.750	25
23	121	118	980	94,1	1.530	25
24	104	101	980	80,7	1.320	25
25	86,3	84,6	980	67,3	1.100	25
26	69,1	67,7	980	53,8	878	25
27	51,8	50,8	980	40,4	659	25
28	34,6	33,9	981	26,9	440	25
29	17,3	17	981	13,5	220	25

Table 19: Viscosity AK1000 - 25 °C

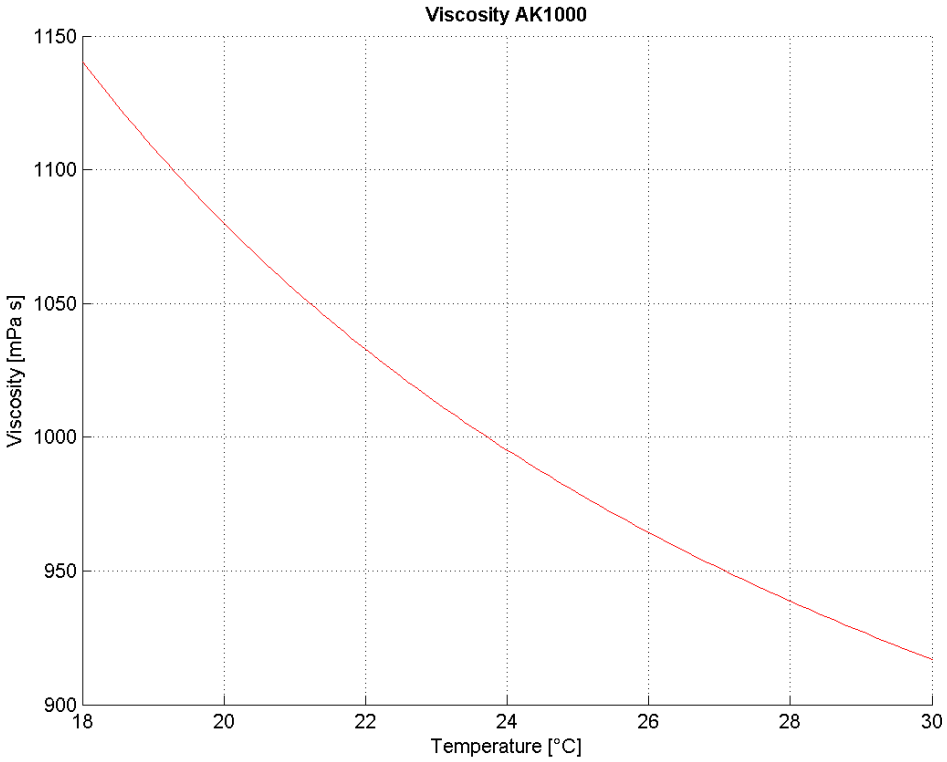

Figure 74: Viscosity silicon oil AK1000

F Results Thermal Coil Analysis

F.1 "Cooled Body Coil"

Scope	**Material**	**Thermal Conductivity [W/(m °C)]**	**Specific Heat [J/(kg °C)]**
Coil Body	Aluminium Alloy	165 @ 100 °C (Temperature dependent)	875.0
Wire	Copper Alloy	401	385
Water Adapter	Copper Alloy	401	385
Screws	Structural Steel	60.5	434.0

Table 20: Material settings - "Cooled Body Coil"

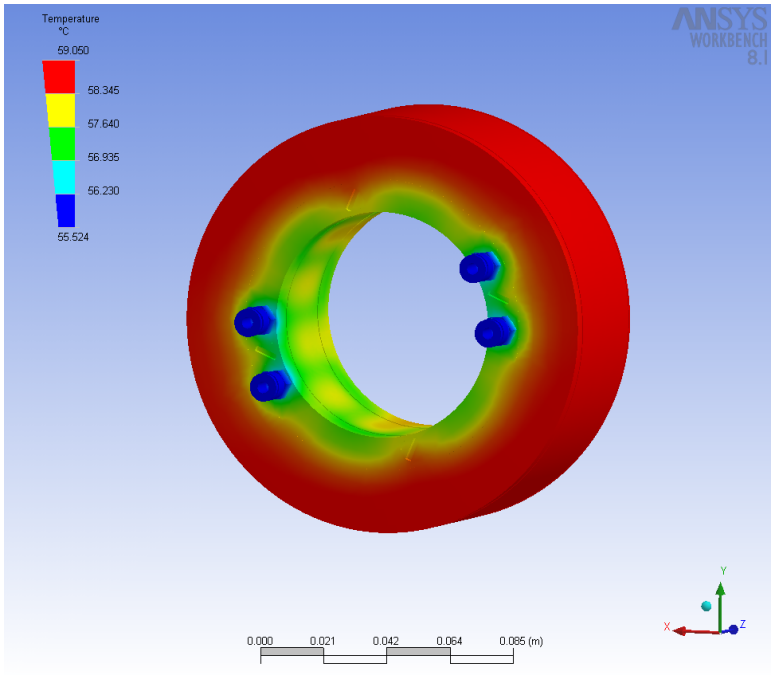

Figure 75: Temperature all bodies

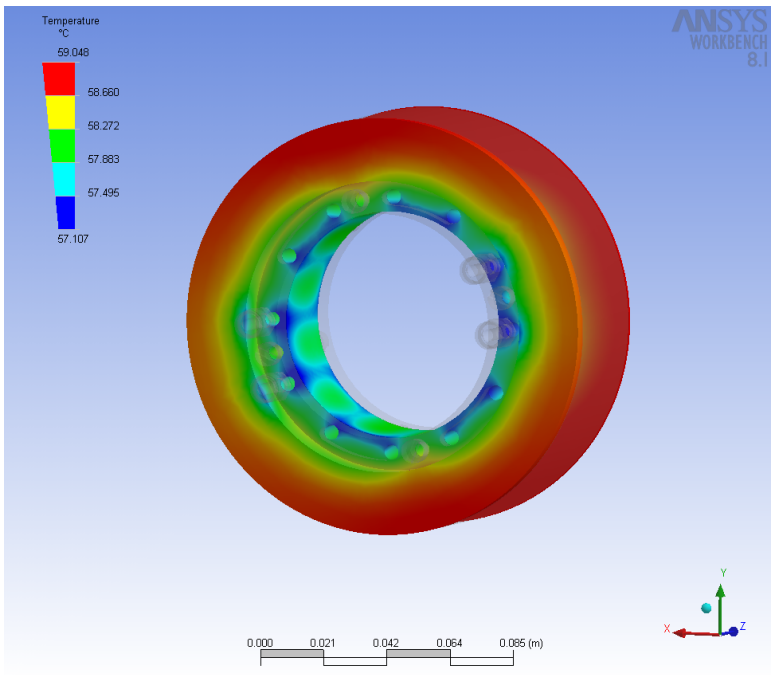

Figure 76: Temperature coil body

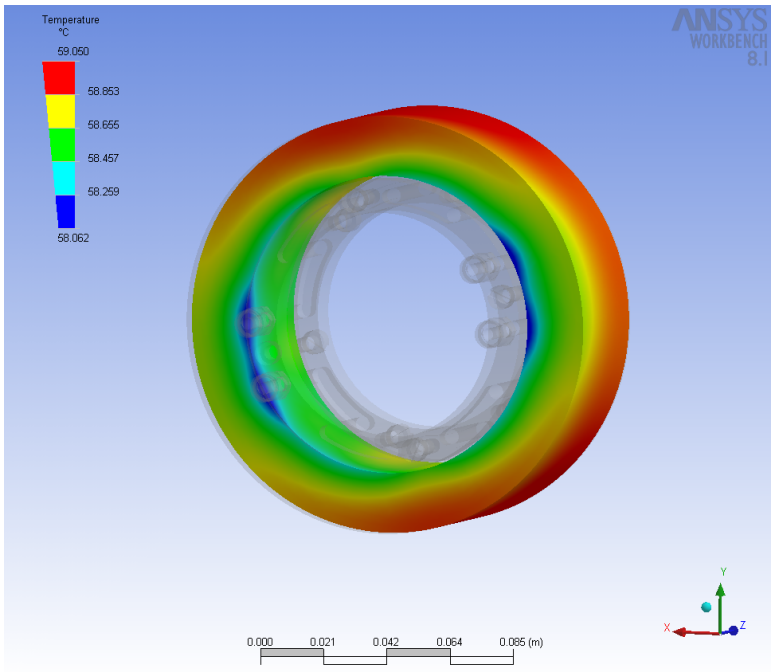

Figure 77: Temperature wire

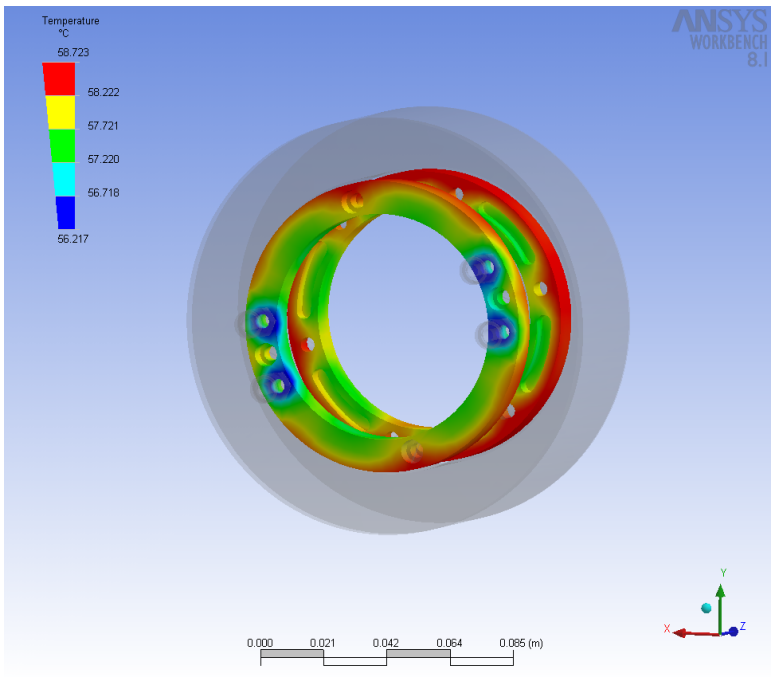

Figure 78: Temperature caps

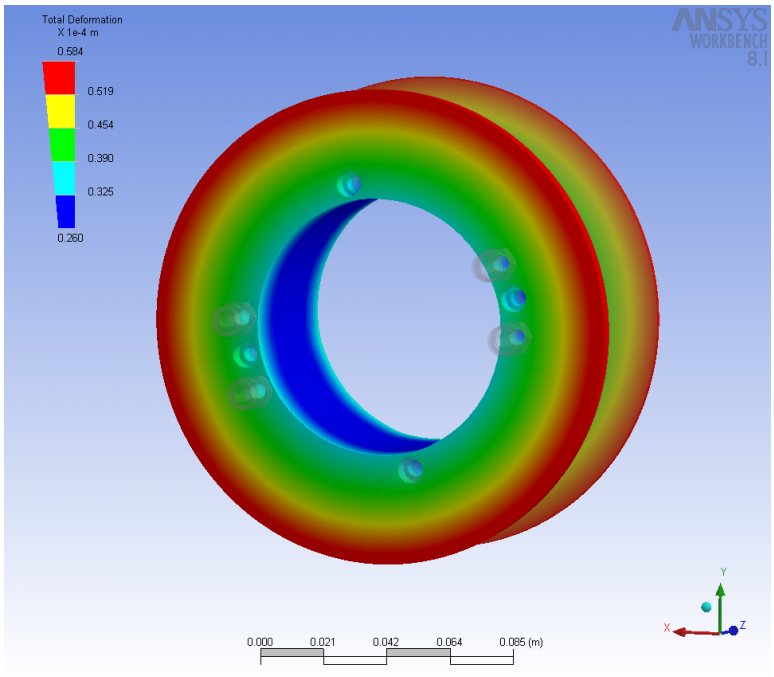

Figure 79: Total deformation body and caps

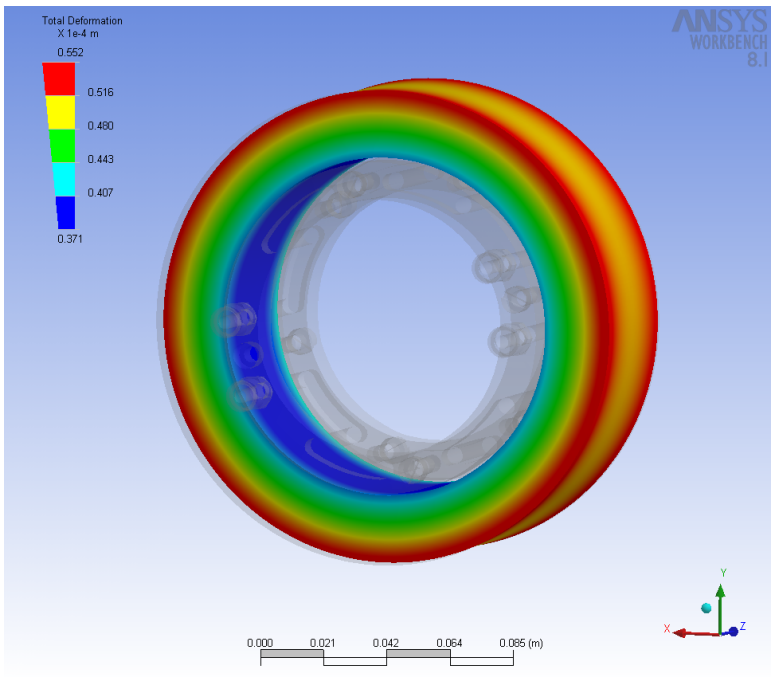

Figure 80: Total deformation wire

F.2 "Winded Cooling Tubes Coil"

Scope	**Material**	**Thermal Conductivity [W/(m °C)]**	**Specific Heat [J/(kg °C)]**
Coil Body	Aluminium Alloy	165 @ 100 °C (Temperature dependent)	875.0
Wire	Copper Alloy	401	385
Water Cooling Tubes	Copper Alloy	401	385

Table 21: Material settings - "Winded Cooling Tubes Coil"

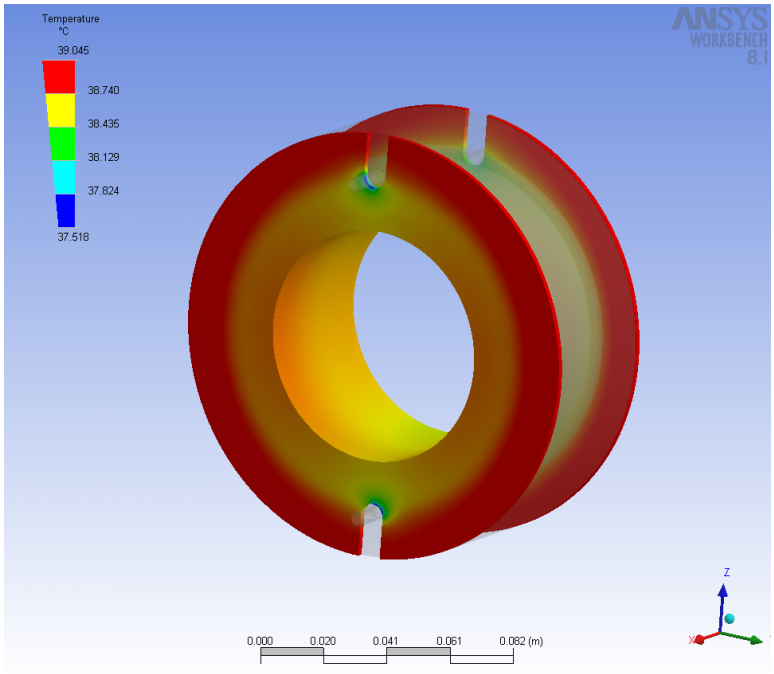

Figure 81: Temperature coil body

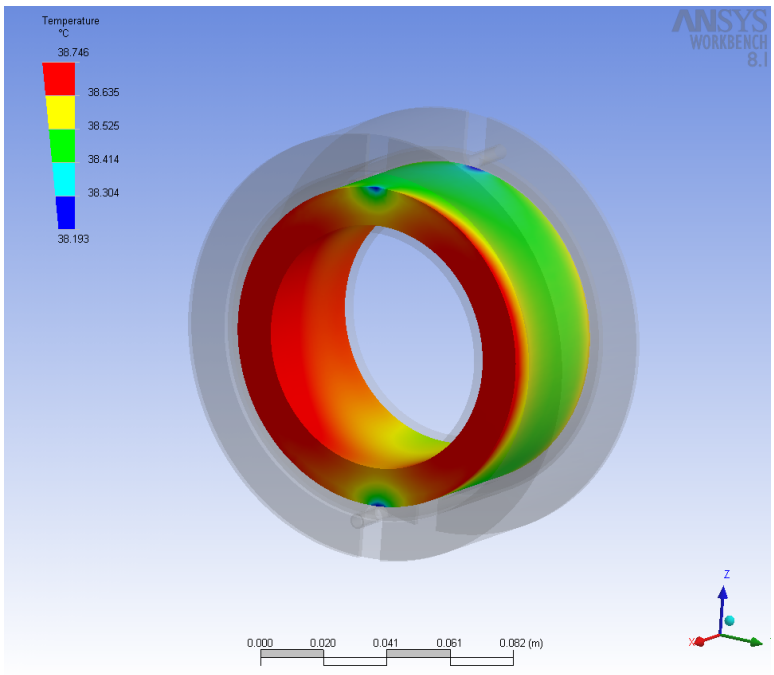

Figure 82: Temperature inner wire

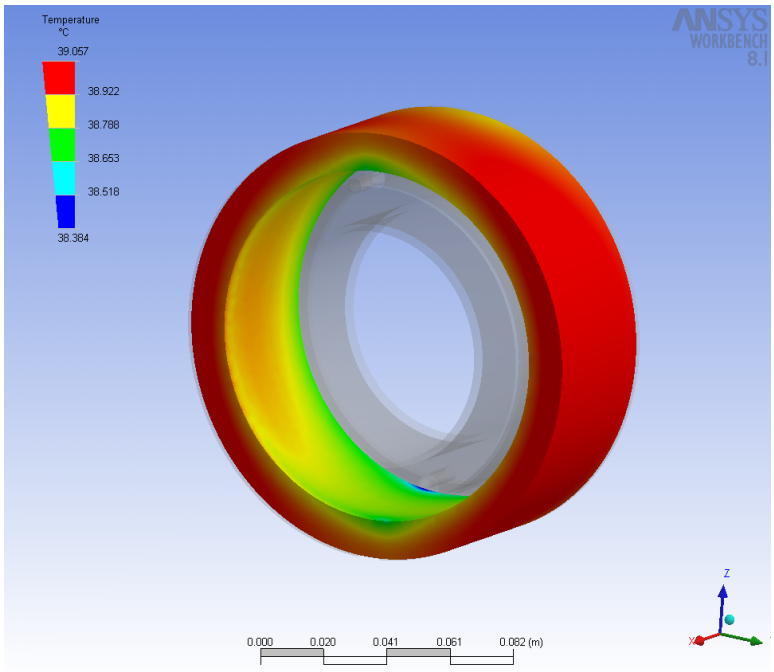

Figure 83: Temperature outer wire

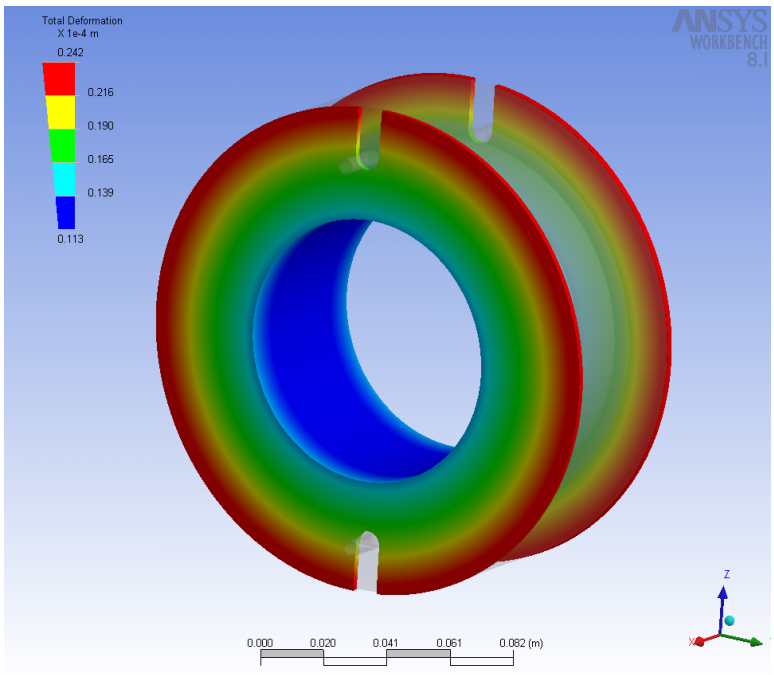

Figure 84: Total deformation body

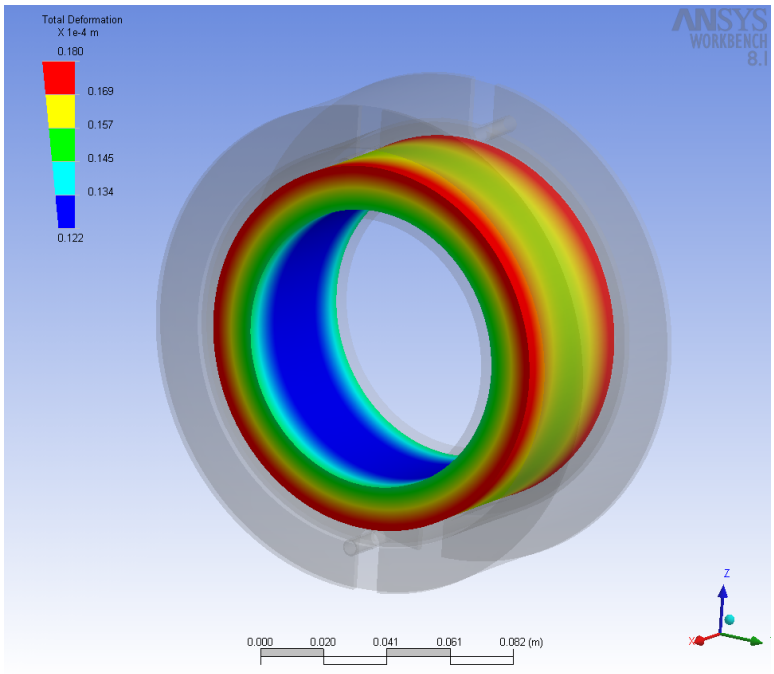

Figure 85: Total deformation inner wire

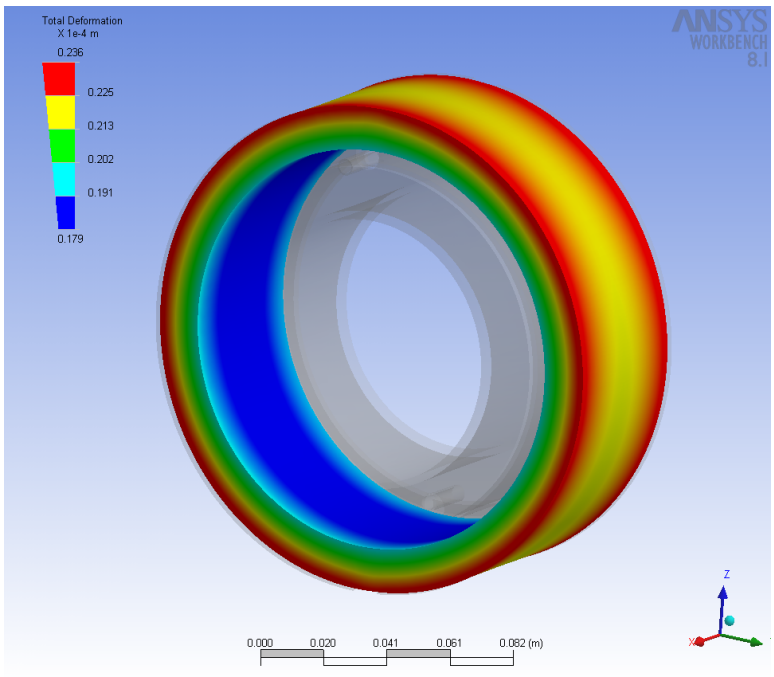

Figure 86: Total deformation outer wire

G Abbreviations

3D 3 Dimensional

ASTM American Society for Testing and Materials

CAD Computer Aided Design

CNC Computer Numeric Control

EC European Council

EMF Electro Magnetic Field

ETH Federal Institute of Technology

FDA Food and Drug Administration

FEM Finite Element Method

GUI Graphical User Interface

HF High Frequency

IEC International Electrotechnical Commission

ILW Institute of Food Science and Nutrition

IRIS Institute of Robotics and Intelligent Systems

ITET Institute of Information Technology and Electrical Engineering

MRI Magnetic Resonance Imaging

NEMA National Electrical Equipment Manufacturer's Association

NMR Nuclear Magnetic Resonance

PCB Populated Circuit Board

PID Proportional plus Integral plus Derivative

RF Radiofrequency

SAR Specific Absorption Rate